MONTE CARLO SIMULATION OF NEUTRAL-BEAM INJECTION FOR MIRROR FUSION REACTORS

BY

RONALD LEE MILLER

B. S., University of Illinois, 1971
M. S., University of Illinois, 1973

THESIS

Submitted in partial fulfillment of the requirements
for the degree of Doctor of Philosophy in Nuclear Engineering
in the Graduate College of the
University of Illinois at Urbana-Champaign, 1979

Urbana, Illinois

DISCLAIMER

MONTE CARLO SIMULATION OF NEUTRAL-BEAM INJECTION FOR MIRROR FUSION REACTORS

Ronald Lee Miller, Ph.D.
Nuclear Engineering Program
University of Illinois at Urbana-Champaign, 1979

Computer simulation techniques using the Monte Carlo method have been developed for application to the modeling of neutral-beam injection into mirror-confined plasmas of interest to controlled thermonuclear research. The energetic (10-300 keV) neutral-beam particles interact with the target plasma ($T_i \sim$ 10-100 keV) through electron-atom and ion-atom collisional ionization as well as ion-atom charge-transfer (charge-exchange) collisions to give a fractional trapping of the neutral beam and a loss of charge-transfer-produced neutrals which escape to bombard the reactor first wall. Appropriate interaction cross sections for these processes are calculated for the assumed anisotropic, non-Maxwellian plasma ion phase-space distributions. The target plasma is assumed to be confined by a Yin-Yang mirror-coil configuration and has distinct radial and axial density profiles as modeled in steady-state and three spatial dimensions. The energy and angular distributions of a population of neutral test particles are computed to give statistical estimates of neutral-beam trapping efficiency, non-uniform first-wall surface heating rates and first-wall sputtering-erosion for use in engineering-design calculations. The reference parameters of the Mirror Fusion Test Facility (MFTF) and the mirror Fusion Engineering Research Facility (FERF) are used as particular applications of the simulation. Benchmark calculations of idealized configurations are summarized. A guide to the NUBIN computer code developed for this study is included.

ACKNOWLEDGEMENT

It is my distinct pleasure to here gratefully acknowledge the several years of encouragement and support provided by a number of individuals and institutions in the course of this research. In particular, I wish to thank my thesis advisor, Professor George Miley, for his original inspiration and continuing patience. The unselfish consideration of the members of my thesis committee as well as other members of University faculty is certainly appreciated. In addition, I thank Doctors Robert Burke and Thomas Coultas for the opportunity to do preliminary work on this project at the Argonne National Laboratory. The cooperation and interest of Doctors David Bender, Gustav Carlson, Steven Devoto, Gordon Hamilton, Ralph Moir and Mr. Charles McDowell; all of the Lawrence Livermore Laboratory; are noted with special thanks. I also mention the helpful discussions and stimulating working environment provided by my friends and co-workers in the Fusion Studies Laboratory of the University, particularly Dr. Charles Bathke and Mr. Mark Campbell.

I acknowledge with thanks the financial support provided to this project by the United States Energy Research and Development Administration under Contract US ERDA EY-76-S-02-2218. In addition, I gratefully acknowledge the opportunities to use the excellent computational facilities and staff support of the University's Digital Computer Laboratory and the Magnetic Fusion Energy Computer Center. Finally, I especially thank Mrs. Chris Stalker for her careful typing of this manuscript.

TABLE OF CONTENTS

I. INTRODUCTION

A. Motivation.

The research and development program for the magnetic mirror confinement approach to controlled thermonuclear fusion reactors is in a transitional phase. As R. Post's historical review[1] of mirrors indicates, decades of patient work on a series of relatively small-scale physics experiments culminating in the 2XIIB device has recently indicated the validity of the classical confinement scaling relation for ion temperatures up to ~10 keV as well as the warm-plasma-stream suppression of loss-cone instabilities.[2] The progress made in these two areas of concern now suggests that mirror fusion systems can be extrapolated to the scientific feasibility stage and beyond to the commercial power reactor level. To that end, final design and construction of the next generation of mirror machines, the Mirror Fusion Test Facility (MFTF),[3] is now underway at the Lawrence Livermore Laboratory. Simultaneously, two variants of the standard mirror approach, the Tandem Mirror Reactor (TMR)[4] and the Field-Reversed Mirror (FRM)[5] have recently been advanced as promising techniques to improve mirror particle and energy confinement and thus enhance the energy multiplication capabilities of mirror reactor systems. On the technological side, the pending availability of high-energy, high-current, long-pulsed neutral beam injectors promises an exciting series of near-term mirror experiments under reactor-like temperature conditions in the MFTF and perhaps in the proposed Fusion Engineering Research Facility (FERF),[6] a materials test device with applications to the overall fusion technology program. A vigorous mirror fusion program incorporating the above elements is thus seen[7]

to be a strong alternative to the mainline tokamak fusion effort.

Because mirror systems are open-ended, steady-state operation will require the continuous injection of energetic particles to sustain the confined plasma against both particle and power losses. Particle injection perpendicular to the magnetic field lines maximizes confinement time insofar as the particles start out as far away in velocity space from the mirror loss cones as is possible. First suggested in 1953 independently by S. Colgate and W. Brobeck,[1] neutral-atom injection facilitates the penetration of injected particle beams across the confining magnetic field. Trapping of these energetic particles is then accomplished by impact ionization collisions with the target plasma. For all of the mirror devices cited above, the interaction of the neutral-beam injection subsystem and the mirror-confined plasma is of critical importance to the system design. Aside from technological aspects of neutral-beam injector development, important plasma-engineering questions regarding the interaction of high-energy beams and the target plasma are receiving increasing research attention. Of fundamental concern are the total system power balance and the thermal/mechanical design implications for the first wall. The characteristic operating energies and plasma radii for the mirror machines anticipated for operation in the next decade, by increasing both a) the charge-transfer interaction rate between injected neutral atoms and plasma ions and b) the escape probability of any neutrals produced in such collisions, make these concerns even more important for the near term than they might eventually be for mirror power reactors. For these intermediate devices, neutral-atom bombardment of the first wall can a) represent the major thermal load,

which, due to its nonuniform distribution, results in local "hot spots," b) produce localized sputtering and consequent surface erosion, and c) stimulate cold neutral reflux to the plasma. Further, the particle and power losses implied by this neutral-atom leakage must be offset by more demanding injector current and voltage requirements. This results in a higher recirculating power fraction which degrades system performance. First-wall materials choice, lifetime and heat-removal requirements may be severely impacted.

If mirror systems are to reach their full potential, these problem areas must be clearly identified theoretically and then overcome experimentally. This study attempts to assess these problems quantitatively in realistic mirror-plasma configurations as a contribution to the theoretical identification process. For the first time, the major critical features of the above problem have been brought together in a common model, providing new opportunities for meaningful results in a form which can be experimentally verified. The desire to model the steady-state neutral-beam/plasma/wall system in three spatial dimensions while incorporating the known phase-space anisotropies inherent in mirror-confined plasmas has motivated the implementation of computer simulation techniques using the so-called "Monte Carlo" (MC) method.[8,9] In this approach a large number of hypothetical neutral test particle histories are tracked on the computer to give an approximate, statistical picture of the physical processes under investigation. Tracking continues through successive generations of charge-transfer-produced neutrals until the test particle is ionized and integrated into the background plasma or until it escapes to bombard the first wall. Using

this new approach, key information regarding the spatial, angular and energy distributions of the charge-transfer-produced neutral particles can now be obtained routinely. The technique is flexible so that, as better understanding of the relevant physics develops, new calculational modules may be easily substituted or incorporated into the overall simulation framework. Finally, since the results of this simulation work can be applied directly to the design of near-term mirror machines, this study is both practical and timely.

It is convenient to, at this point, anticipate the organization of the presentation of the detailed discussion of this study. The remaining section of this introductory chapter will survey related research work done in the modeling of neutral-beam injection into mirror-confined plasmas. This will include preliminary scoping calculations performed by the author as well as the work of other researchers. While simple analytic and numerical models have proven most useful in identifying the salient problem areas, the deficiencies of these approaches make clear the need for improved modeling techniques and at the same time provide useful corroborative checks on certain aspects of the present results.

In Chapter II, the generalized treatment of the interaction cross sections used in this study will be considered. The collisions of primary interest include electron impact ionization, ion impact ionization, large-angle Rutherford scattering and charge transfer (also called charge exchange) involving deuterons. In addition to being a crucial aspect of this MC application, these cross sections are important for all neutral-particle transport studies involving fusion plasma environments. This chapter provides cross section results for a

range of neutral-particle and background-plasma energies far beyond the requirements of the specific reference cases considered in later chapters and thus can serve as a resource for a variety of other calculations. The cross sections here are averaged over the plasma phase-space distribution functions to obtain $\langle\sigma v\rangle$ rate coefficients. The computer code MCSAVG was developed by the author to compute these rate coefficients.

Chapter III will explain the MC neutral-particle-tracking techniques invented or adapted for this work. In contrast to the over thirty years of experience at many research centers in MC codes for neutron and gamma ray transport studies, little work had heretofore been done in applying MC techniques to neutral-particle transport problems of interest to the fusion community. This chapter will introduce the algorithms used in the Neutral Beam Injection (NUBIN) MC code developed by the author for this study.

Chapter IV will indicate the specific aspects and limitations of the mirror-plasma model used in this study. This plasma is characterized by the well-known double-fan radial boundary produced by "Yin-Yang" coils[10] and has separate radial and axial density profiles to exploit the three-dimensional capabilities of the MC approach. As noted previously, the MC approach places few fundamental restrictions on the sophistication or complexity of the plasma model. More elaborate characterizations than used here can be substituted with lesser penalties in terms of increased computation time than might be expected for alternative numerical procedures.

Chapter V will present the results of some general benchmark computations using the NUBIN code as well as detailed studies of two reference mirror devices, the MFTF and the FERF. Of particular interest

are the neutral-beam trapping efficiency results and the first-wall neutral-atom bombardment distributions in both energy and angle.

Chapter VI will consider the reactor engineering implications of these results for the FERF in terms of localized first-wall surface heating and sputtering erosion rates. New knowledge in these areas can be expected to affect materials choice and optimization of the thermal/mechanical point design of the first wall of that system.

Finally, since the NUBIN/MCSAVG computer code package developed for this project is useful as an engineering design tool only if other interested researchers with their own sets of device parameters have practical access to it, the attached Appendix serves as a "Computer Code User's Guide." Discussions of both the MCSAVG cross section averaging code of Chapter II and the MC simulation code NUBIN of Chapter III are included.

B. Related Studies.

1. Literature Review.

A number of researchers have investigated various aspects of neutral-atom injection into mirror machines and have developed analytic and numerical treatments of the problem. However, in order to obtain tractable models, various crucial approximations, idealizations and distribution averagings have had to have been made in the areas of a) the anisotropies of mirror-confined plasmas, b) the plasma radial and axial density profiles, c) the characterization of the neutral beam and d) the calculation of interaction cross sections. A large body of parallel work applied to neutral-beam injection into tokamak devices also exists[11-13] but will not in general be cited further here.

A. Futch and co-workers described[14] an early time-dependent mirror-plasma build-up calculation[15] for a cylindrical system. The low plasma temperatures considered (< 1 keV) are consistent with the available experiments of the time [e.g. DCX (ORNL) and ALICE (LRL)] or with the start-up of a more modern device. The plasma ions were taken to have an isotropic Maxwellian velocity distribution and only one generation of charge-transfer-produced neutrals was considered. These approximations allowed for detailed concentration on finite gyro-orbit effects as the injected neutral atoms become ionized. A similar calculation, this time in spherical geometry, was performed by R. Colchin.[16]

Contemporary interest in neutral-beam trapping calculations for the reactor regime traces largely to A. Riviere[17], whose compilation of ionization and charge-transfer cross-section formulae has become a standard resource for subsequent researchers. Chapter III of the present work generalizes and extends this calculation of $\langle\sigma v\rangle$ rate coefficients. In addition to his cross-section work, Riviere was perhaps the first to argue quantitatively that the plasma thickness parameter, $(\bar{n}D)$, where $\bar{n}$ is the average number density and D is the beam path length in the plasma, should neither be so low as to allow transmission of too large a fraction of the neutral beam nor be so high as to prevent sufficient penetration of the beam to the plasma core.

2. Preliminary Studies.

At this point in the review of previous work in the area of modeling neutral beam injection into mirror-confined plasmas, it is instructive to consider in greater detail a series of calculations which will serve to a) establish certain notational conventions and b) provide a convenient method to check and scale the specific results of Chapter V.

A straightforward analytic model attributed[18,19] to A. Hunt has been used to study neutral-beam injection into a spherical target plasma under the following restrictive assumptions :

a. The radial plasma density profile is uniform.

b. The neutral-beam injection energy E_o coincides with the characteristic plasma energy $\tilde{E}_p$.

c. The neutral beam diameter is much smaller than the size of the target plasma (the "pencil-beam" approximation).

d. The injection path is through the center of the plasma, giving the longest chord length D, the diameter.

e. One generation of charge-transfer neutral particles is considered.

f. All charge-transfer neutrals are born at the center of the plasma, are directed isotropically outward, and have energy E_o.

As illustrated in Fig. 1, a fraction (f_p) of the neutral-beam current will traverse the plasma without interaction and impinge on the opposite chamber wall or be recovered via a direct collection unit. Another fraction (f_t) of the beam will undergo competing electron-ionization, ion-ionization or ion-atom charge-transfer interactions with the target plasma. Ions formed in these collisions will generally be trapped in the plasma. Unless subsequent generations of charge-transfer-produced neutrals are reionized by later collisions, they (f_w) will escape the plasma and deposit their kinetic energy on the first wall surface. Conservation of particle inventory requires that

$$f_p + f_t + f_w = 1 \qquad (1)$$

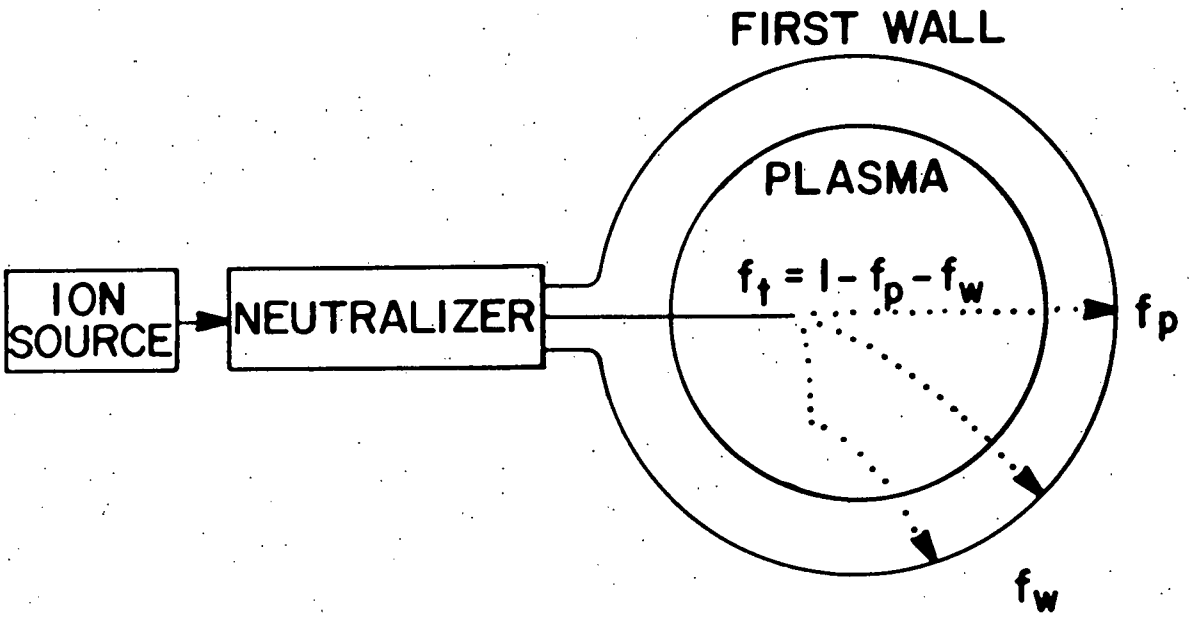

Figure 1. Schematic representation of neutral-beam injection into a target plasma defining the terminal fractions f_t (trapped ions), f_p (penetrating neutrals), and f_w (wall-bombardment neutrals).

The neutral beam is attenuated exponentially as it traverses the plasma diameter D such that

$$f_p = \exp\left\{-\frac{\bar{n}\langle\sigma v\rangle_T D}{v_o}\right\} \equiv \exp\{-\gamma\} \qquad (2)$$

where $\bar{n}$ is the plasma number density, v_o is the neutral-particle injection speed and $\langle\sigma v\rangle_T$ is the total interaction rate coefficient; which is the sum of contributions from electron ionization ($\langle\sigma v\rangle_{ei}$), ion ionization ($\langle\sigma v\rangle_{ii}$) and ion charge transfer ($\langle\sigma v\rangle_{cx}$). Numerical values for these rate coefficients are obtained using procedures described in Chapter II. The argument of the exponential term on the right-hand side of Eqn. (2) is denoted by "$-\gamma$" in the discussion to follow for notational simplification.

Following assumption f, the fraction of those neutral-beam atoms undergoing charge transfer multiplied by the probability that they will not be reionized (assumption e) yields the fraction of the neutral-beam current that bombards the first wall as

$$f_w = \frac{\langle\sigma v\rangle_{cx}}{\langle\sigma v\rangle_T}\left[1 - \exp\{-\gamma\}\right]\exp\left\{\frac{-\gamma}{2}\left[\frac{\langle\sigma v\rangle_{ei} + \langle\sigma v\rangle_{ii}}{\langle\sigma v\rangle_T}\right]\right\}. \qquad (3)$$

Using Eq. (1), the trapping efficiency becomes

$$f_t = \left[1 - \exp\{-\gamma\}\right]\left\{1 - \frac{\langle\sigma v\rangle_{cx}}{\langle\sigma v\rangle_T}\exp\left\{\frac{-\gamma}{2}\left[\frac{\langle\sigma v\rangle_{ei} + \langle\sigma v\rangle_{ii}}{\langle\sigma v\rangle_T}\right]\right\}\right\}. \qquad (4)$$

This analytical model was later extended by the author[20,21] to include the fractional reionization of all successive generations of charge-transfer neutrals, thus eliminating restriction e. A convergent infinite series solution results in the corresponding terminal neutral-beam fractions [distinguished from Eqns. (3-4) by the superscript "'"]. As before

$$f_p' = f_p \qquad (5)$$

$$f_w' = \frac{\frac{\langle\sigma v\rangle_{cx}}{\langle\sigma v\rangle_T}\left[1 - \exp\{-\gamma\}\right]\exp\{\frac{-\gamma}{2}\}}{\left\{1 - \frac{\langle\sigma v\rangle_{cx}}{\langle\sigma v\rangle_T}\left[1 - \exp\{\frac{-\gamma}{2}\}\right]\right\}} \tag{6}$$

and

$$f_t' = \left[1 - \exp\{-\gamma\}\right]\left\{1 - \frac{\frac{\langle\sigma v\rangle_{cx}}{\langle\sigma v\rangle_T}\exp\left\{-\frac{\gamma}{2}\right\}}{\left\{1 - \frac{\langle\sigma v\rangle_{cx}}{\langle\sigma v\rangle_T}\left[1-\exp\{\frac{\gamma}{2}\}\right]\right\}}\right\} \tag{7}$$

Figure 2 presents a comparison of the two analytic models by graphing the neutral-beam terminal fractions as a function of the plasma thickness parameter $\bar{n}D$. The fixed parameters are those of the FERF test case summarized in Table I.

The Carlson and Hamilton[22] numerical model, developed as an alternative approach, relaxes assumption f, allowing the charge-transfer neutrals to be born exponentially along the beam attenuation path. The 1-generation restriction e is retained. In comparing the 1-generation to the ∞-generation analytic model, there is close agreement for the particular case of Table I. For other combinations of $\bar{n}D$ and $\tilde{E}_p$ this agreement does not necessarily persist, however. The two models merge for low values of $\bar{n}D$ at all energies as expected. For increased values of $\bar{n}D$, however, as can be seen in Fig. 2, the contribution made by the fractional ionization of later generations of charge-transfer neutrals results in increasingly higher values of f_t and lower values of f_w. For energies less than 70 keV the disparity between the two approximations is greater. For higher energies, the relative influence of charge transfer declines and the disparity becomes negligible for $E_o > 300$ keV for all values of $\bar{n}D$.[20] The Carlson and Hamilton model has been used

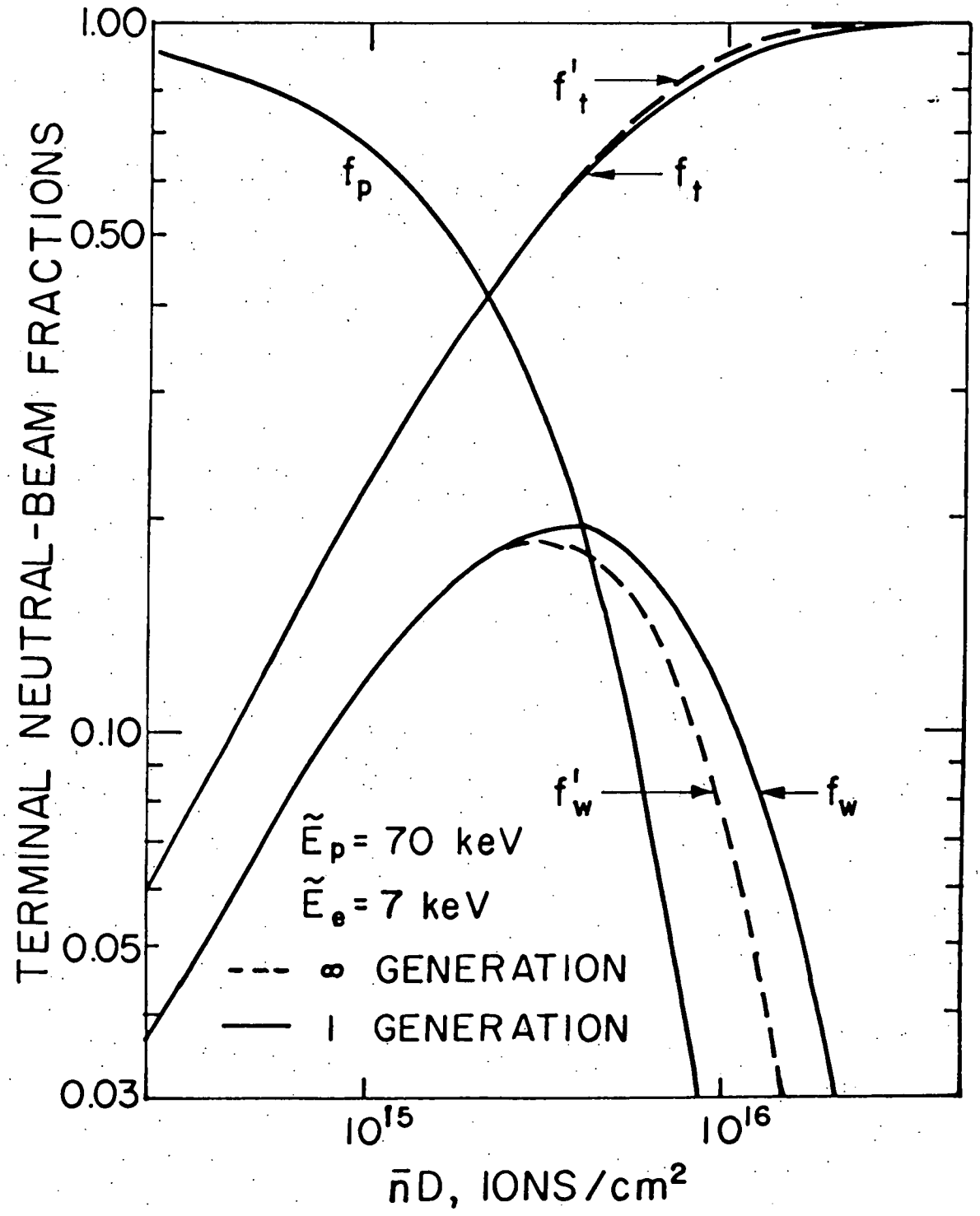

Figure 2. Comparison of analytic 1-generation and ∞-generation neutral-beam injection models as a function of the target plasma thickness parameter $\bar{n}D$.

TABLE I

Preliminary Injection Models Applied to FERF Test Case

Characteristic plasma ion (D^+) energy, $\tilde{E}_p$ (keV)	70
Characteristic plasma electron energy, $\tilde{E}_e$ (keV)	7
Average plasma number density, $\bar{n}$ (ions/cm^3)	$1.0(10)^{14}$
Spherical target plasma diameter, D (cm)	50
$\langle\sigma v\rangle_{ei}$ (cm^3/s)	$1.08(10)^{-8}$
$\langle\sigma v\rangle_{ii}$ (cm^3/s)	$\sim 4.8(10)^{-8}$
$\langle\sigma v\rangle_{cx}$ (cm^3/s)	$\sim 5.0(10)^{-8}$
Injection atom energy, E_I (keV)	65
Injection atom speed, v_o (cm/s)	$2.5(10)^8$
γ	~ 2.1
Mean free path, $\lambda = D/\gamma$ (cm)	~ 24

Results:	Carlson & Hamilton Fig. 3 of Ref. 22 (1-generation)	Hunt Refs. 18-19 (1-generation)	Miller Refs. 20-21 (∞-generation)
f_{ei}	-*	0.16	0.17
f_{ii}	-*	0.52	0.53
$f_t = f_{ei} + f_{ii}$	~0.69	0.68	0.70
f_p	~0.12	0.12	0.12
f_w	~0.19	0.20	0.18

*Not calculated separately

more recently by D. Bender and G. Carlson[23] to study the effects of the parasitic $E_0/2$ and $E_0/3$ neutral beam components expected in positive ion systems. These components were identified as major power loss channels because of charge-transfer effects of the type being considered for the primary beam and have therefore been subjected to Monte Carlo simulation as well.

Little more can be expected from further extension of approaches such as the Carlson and Hamilton model since the incremental knowledge to be gained would probably not justify the complicated algebraic refinements and manipulations that would have to be made. The "building block" aspects of the Monte Carlo approach thus become advantageous. Relatively simple modules can be fit easily into a general framework to upgrade the approach.

Finally, since the inception of this project, T. Kaiser[24,25] has initiated a preliminary Monte Carlo analysis of neutral-beam injection into mirror experiments (e.g. 2XIIB) using the approach of M. Hughes and D. Post.[26]. This reflects a growing interest in the use of Monte Carlo methods for this class of problems. The approach is somewhat more idealized and restrictive that that used here in order to provide a neutral-particle transport module with rapid computer execution capabilities for use by other code systems.

II. INTERACTION CROSS SECTIONS

A. Overview.

For purposes of this study, the interactions of interest between energetic neutral-beam atoms and the target plasma ions and electrons include electron impact ionization, ion impact ionization and atom-ion charge-transfer collisions. This study is then consistent with work reported in Refs. 18, 19, 22, and 23. Of lesser importance, but easily amenable to the MC simulation process, are large-angle Rutherford scattering collisions with the plasma ions. Excitation of the neutral atoms and all interactions involving alpha particle fusion products or impurities is neglected. While the relevant ionization and charge-transfer cross sections for interactions involving these other species are comparable to those for hydrogenic ions,[17] their low density in the open-ended devices considered here renders their influence negligible.

The question of what cross section representations to use for the hydrogenic interactions is one of an over-abundance of information rather than a scarcity. This has been a classic area for both theoretical and experimental investigation for many years; the relevant literature is consequently vast. References 27-70 represent an inexhaustive, chronological bibliography of that literature. Comprehensive periodic reviews are provided by References 32, 56, 66, 68 and 70. Available theoretical treatments of atomic collision phenomena can be distinguished by two categorizations: the Born approximation[27,42] and the classical binary encounter approximation.[28,30,34,43,50,55,57,58,61,62,65] In particular, the binary encounter formalism of E. Gerguoy

and co-workers[55,57,61,62] appears satisfactory for treating all three interactions of primary interest to this study on a self-consistent basis. This approach also avoids the awkward notation and certain questionable subsidiary approximations of the M. Gryzinski procedures[30,34,50,51,65], which represent an alternative binary-encounter approach. These theoretical methods perform about equally well (within a factor of three) in predicting experimental results in the energy range (10-100 keV) of interest.[29]

The present study uses the analytic representations of experimental results as compiled by A. Riviere[17] for hydrogenic collisions as they seem adequate and provide commonalty with other work.[18,19,22,23,71] The exclusive consideration of deuterium atoms and ions assumes that the cross sections depend only on the relative collision speed and not on the masses of the isotopes involved as has been experimentally verified to within two percent for hydrogenic collisions in the energy range 20-55 keV.[64]

The remainder of Chapter II considers the several representations of the microscopic interaction cross sections and the procedures for obtaining the corresponding phase-space-averaged $\langle\sigma v\rangle$ rate coefficients. The interface with the MC code is considered in Chapter III.

B. Electron-Impact Ionization.

For the ionization of atomic hydrogen by electron impact, A. Riviere[17] cites the classical theory of M. Gryzinski.[48] Correcting typographical errors* in both sources, the expression for the micro-

*The required numerical coefficient is $\sigma_0 = \pi e^4$, which for U in eV units becomes $6.52(10)^{-14}$ which is given as $6.52(10^{+14}$ in Ref. 17 and $6.56(10)^{-16}$ in Ref. 48.

scopic electron ionization cross section $\sigma_{ei}(cm^2)$ becomes

$$\sigma_{ei} = 6.52(10)^{-14}\, U^{-2}\, g(x) \qquad (8)$$

where

$$g(x) = \frac{1}{x}\left[\frac{x-1}{x+1}\right]^{3/2}\left[1 + \frac{2}{3}\left(1 - \frac{1}{2x}\right) \ell n\ (2.7 + \sqrt{x-1})\right],$$

U is the hydrogen ionization potential (13.605 eV) and x is the ratio of the electron energy E_e(eV) to U. Eqn. (8) is plotted in Fig. 3 where σ_{ei} is a function of electron impact energy. There is a threshold for ionization at $E_e = U$. The peak cross section is $8(10)^{-17} cm^2$ for $E_e \sim 50$ eV. Above $E_e \sim 100$ eV the cross section falls off approximately as E_e^{-1}. This analytic representation is a good fit to the available experimental results[17, 53] for $E_e < 20$ keV.

C. Ion-Impact Ionization.

The microscopic cross section for the ionization of atomic hydrogen by protons has been measured by W. Fite and co-workers[36] in the energy range 7-40 keV and by H. Gilbody and J. Ireland[41] for 60-370 keV. At higher energies ionization by protons is assumed to be equivalent to ionization by electrons impacting at the same speed. The following analytic expressions[17] are used to give the hydrogenic ion-ionization cross section $\sigma_{ii}(cm^2)$ as a function of proton collision energy E(eV):

$$\log_{10} \sigma_{ii} = 0.8712\ (\log_{10} E)^2 + 8.156\ (\log_{10} E) - 34.883 \qquad (9a)$$

$$\text{for } E < 1.5(10)^5 \text{ eV},$$

$$\sigma_{ii} = 3.6(10)^{-12}\, E^{-1} \log_{10}(0.1663\ E) \qquad (9b)$$

$$\text{for } E > 1.5(10)^5 \text{ eV}.$$

The curve labeled "ii" in Fig. 4 plots this expression. The peak cross section occurs for $E \sim 7(10)^4$ eV and is $\sigma_{ii} \sim 1.7(10)^{-16}$ cm^2, about

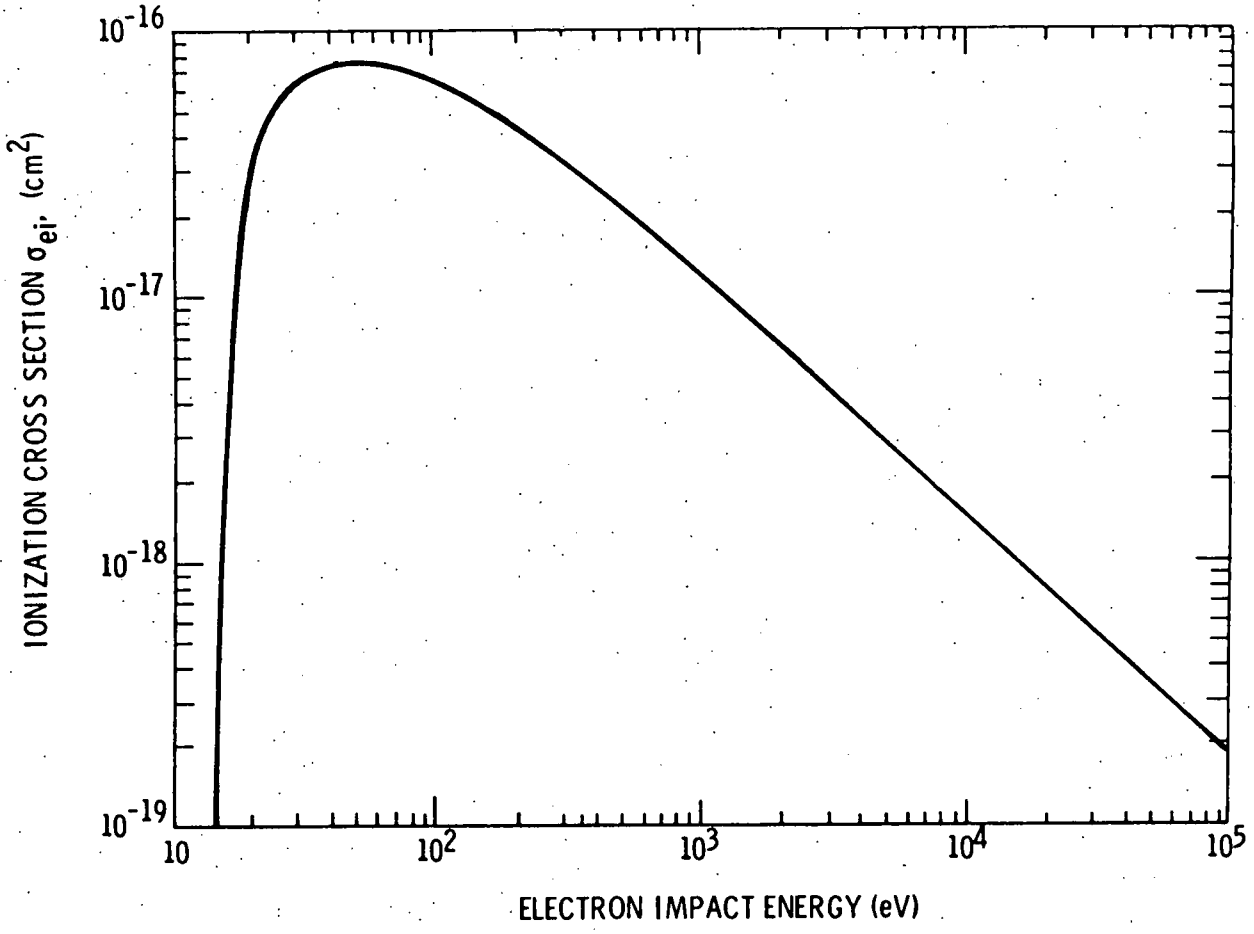

Figure 3. Microscopic cross section for the ionization of hydrogen by electron impact as a function of electron impact energy.

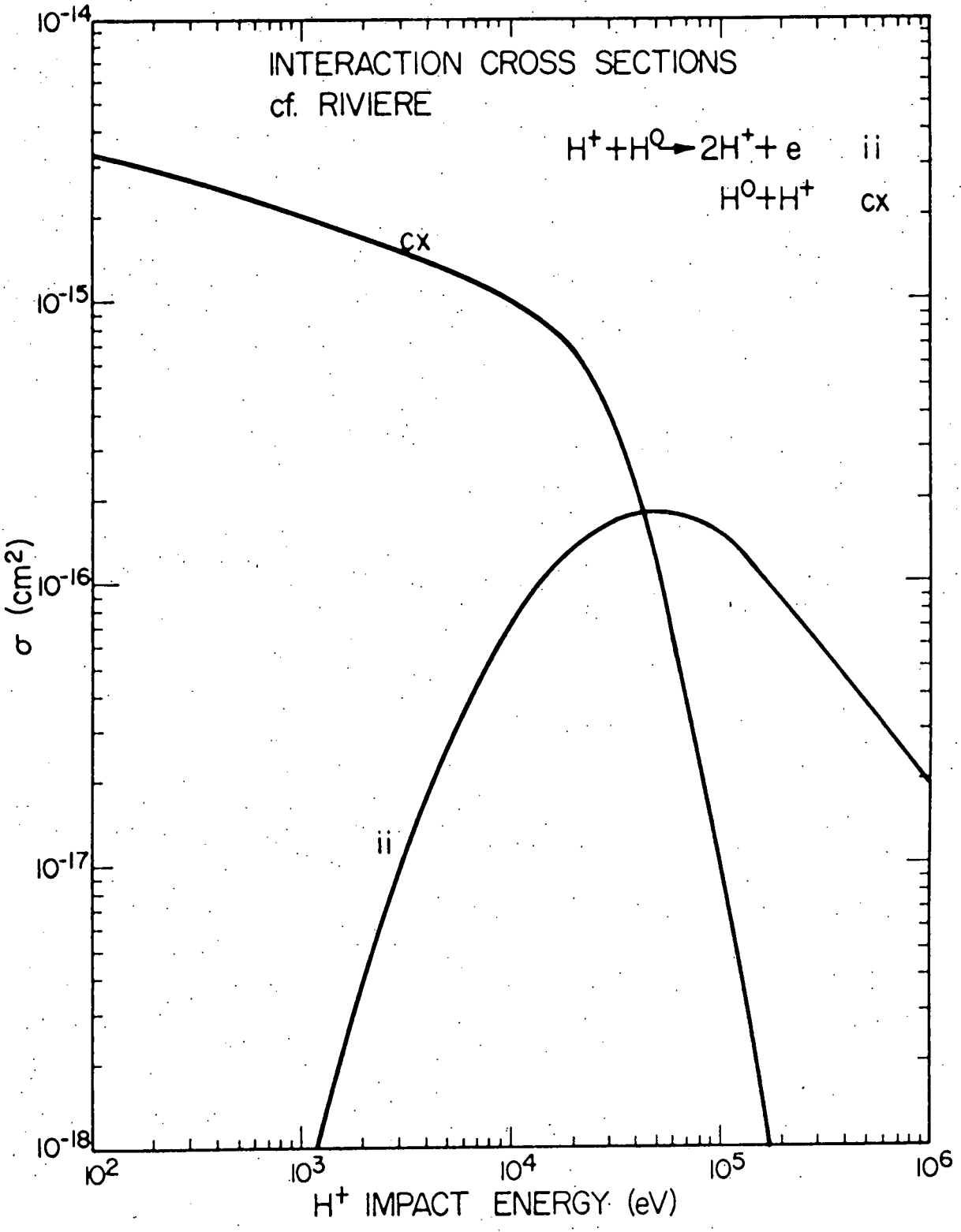

Figure 4. Comparison of analytic representations (cf. Riviere, Ref. 17) for the microscopic cross sections for proton ionization (ii) and charge transfer (cx) collisions with atomic hydrogen as a function of proton impact energy.

twice the maximum of σ_{ei}. The normal E^{-1} dependence is also seen here at high energies. The agreement of the analytic expressions with the experimental data is satisfactory as can be seen in Fig. 1 of Ref. 17.

D. Charge Transfer.

The microscopic cross section for charge transfer by protons in atomic hydrogen has been measured by W. Fite and co-workers[36] in the energy range 0.4-40 keV and by H. Gilbody and G. Ryding[52] for 38-130 keV. The following analytic expression[17] gives this cross section $\sigma_{cx}(cm^2)$ as a function of proton energy E (eV):

$$\sigma_{cx} = \frac{0.6937(10)^{-14}\ (1 - 0.155\ \log_{10} E)^2}{1 + 0.1112(10)^{-14}\ E^{3.3}} . \qquad (10)$$

The curve labeled "cx" in Fig. 4 plots this expression. In contrast to the ionization case of the previous section, the charge transfer cross section continues to increase as E decreases. This suggests that for neutral-atom injection into a plasma with a distribution of ion energies, charge transfer will preferentially occur between the neutral atom and those plasma ions having velocity vectors tending to minimize the atom-ion collision energy E. For energies above 80 keV the charge transfer cross section drops below the proton ionization cross section and continues to fall off sharply as E increases. The agreement of the analytic expression with the experimental data is reasonably good as can be seen in Fig. 2 of Ref. 17.

E. Large-Angle Rutherford Scattering.

This section develops the formalism for the MC simulation of the "large-angle" scattering of neutral atoms by ions. An arbitrary critical scattering-angle cutoff can be used to suppress this process relative

to the ionization and charge-transfer processes considered in prior sections of this chapter. It is useful to do this in order to maintain commonalty with the other neutral-beam injection models discussed in Chapter I which omit this effect. At the same time, however, there is an incentive to exploit the latent power of the MC method by anticipating new research opportunities.

For a neutral test particle with mass m_1 and charge number Z_1 moving through a background plasma composed of electrons and ions having mass m_2 and charge number Z_2, the classical differential scattering cross section per atom for interactions between the test particle and the ions is[73]

$$\frac{d\sigma_{RS}}{d\Omega} = \left[\frac{Z_1 Z_2 e^2}{\mu v_R^2}\right]^2 \frac{1}{(1-\mu_{cm})^2} \qquad (11)$$

where e is the electronic charge, v_R is the relative speed of the atom and ion, $\mu = m_1 m_2/(m_1+m_2)$ is the reduced mass, and $\mu_{cm} = \cos\theta_{cm}$ is the cosine of the center of mass (cm) scattering angle θ_{cm}. The subscript "RS" denotes Rutherford scattering. The point-charge, Coulomb-field idealization implicit in Eqn. (11) fails for both large and small impact parameters for the neutral-ion collisions considered. For large impact parameter b, the screening effect of the plasma electrons as well as the bound electron(s) of the test particle cause the scattering potential to fall off more rapidly than r^{-1}, resulting in an effective minimum value for θ_{cm}. For the case of small b, the finite size of the nuclear charge distribution introduces an upper limit to θ_{cm}. The appropriate extremal values for θ_{cm} can be obtained under various assumptions from J. Jackson.[74] Integration of Eqn. 11 over all solid angles yields the Rutherford-scattering cross section $\sigma_{RS}(cm^2)$ as a function of v_R:

$$\sigma_{RS} = 2\pi \left[\frac{Z_1 Z_2 e^2}{\mu v_R^2}\right]^2 \left[\frac{1}{(1-\mu_{max})} - \frac{1}{(1-\mu_{min})}\right] . \qquad (12)$$

For purposes of this study $\mu_{min} = m_2/m_1$ and μ_{max} corresponds to a critical scattering angle denoting the transition between relative dominance of large-angle scattering over cumulative small-angle collisions. Choosing $\mu_{max} = \cos 1°$ allows the claim[73] that there is a probability of 0.85 that cumulative small angle collisions will not exceed ~ 6° for neutral-atom path lengths less than the mean free path for a large-angle scattering event λ_{RS}. Thus, small-angle collisions which will tend to broaden the beam can be neglected relative to large-angle collisions. Also, in this application the 1° cm scattering angle corresponds to ~ 2° in the lab frame, representing only a slight perturbation by beam broadening of the overall simulation problem for the case studies of Chapter V.

F. Target-Plasma Phase-Space Distributions.

While mirror-confined plasma electrons are usually taken[17] to have n isotropic Maxwellian velocity distribution, this is not the case for the ions. The ion velocity distribution is distorted by neutral-beam source effects and by loss-cone phenomena. Following J. Holdren[75] it is assumed that the ion distribution function $f_2(\vec{v}_2)$ is azimuthally invariant [$M(\phi) = 1$] and approximately separable in the μ and v components of velocity; μ being the cosine of the angle θ between the ion velocity vector and the local magnetic field vector $\vec{B}$, and v_2 being the speed of the ion. The further approximation that $\vec{B}$ is nearly parallel to the system axis is a good one near the central region of confinement where the neutral-beam is likely to be injected and will be invoked to

simplify the MC simulation in Chapter III. Thus, to first order in angle,

$$f_2(\vec{v}_2) \sim \frac{1}{v_2^2} f(v_2)\, M_2(\mu) \qquad (13)$$

where $M(\mu)$ is the lowest eigenmode of Legendre's equation:

$$(1-\mu^2)\frac{d^2M}{d\mu^2} - 2\mu\frac{dM}{d\mu} + \lambda M = 0 \qquad (14)$$

$$\text{for } |\mu| \leq 1,\ M(\mu \geq \mu_o) = 0,\ M(-\mu) = M(\mu) \quad .$$

For application to mirror devices, $\mu_o = [(R' - 1)/R']^{1/2} = \cos\theta_o$, where θ_o is the critical loss-cone angle. Particles whose velocity vectors are within θ_o of $\vec{B}$ are not mirrored and escape from the system. R' is the effective mirror ratio in the presence of an ambipolar potential, Φ, defined in terms of the vacuum mirror ratio R such that

$$R' = R/(1 + 2Ze\Phi/mv_2^2) \quad . \qquad (15)$$

In mirror devices, the velocity distribution of electrons is assumed to be in approximate equilibrium, allowing use of a Maxwellian speed distribution and the default isotropic case, $M(\mu)=1$, corresponding to $R'=\infty$. The effects of the ambipolar potential $e\Phi$ cutoff on the electron energy distribution function are neglected for present purposes. This should introduce only minor errors because the electron contribution to the beam trapping is relatively small. Maxwellian, isotropic distributions are typically assumed for both ions and electrons in toroidal devices.

For ions in mirror devices, the following expression[75] (normalized to be unity at $\mu = 0$) is used for the first normal-mode angular distribution:

$$M(\mu) = \frac{\mu_o^2 - \mu^2 + (3\mu_o^2 - 1)\log_e[(1 - \mu^2)/(1 - \mu_o^2)]}{\mu_o^2 - (3\mu_o^2 - 1)\log_e[1 - \mu_o^2]} \quad . \qquad (16)$$

For convenience in some applications, this expression may be approxi-

mated[76] to within 10% by

$$M(\mu) = 1 - \mu^2/\mu_o^2, \text{ for } R' < 1.5 . \quad (17a)$$

$$M(\mu) = 1 + \log_e(1 - \mu^2)/\log_e R', \text{ for } R' > 1.5 \quad (17b)$$

Equation (16) was used for the numerical computation of mirror rate coefficients. The behavior of Eqn. (16) is shown for two typical mirror ratios, R' = 3 and 10, in Fig. 5.

In mirror devices, loss-cone effects and particle injection at energy E_o distort the energy distribution function of confined ions. The expected steady-state ion energy distribution functions for mirror ratios R' = 3 and 10 have been computed using Fokker-Planck techniques by Kuo-Petravic and co-workers.[77] The following analytical expressions, having the same functional forms (but modified coefficients) as those suggested by Riviere[17], are used to represent these energy distributions:

for R' = 3, and $0.18 < E/E_o < 1.0$

$$f(E/E_o) = 1.316(E/E_o)^2 + 2.831(E/E_o) - 0.515 , \quad (18a)$$

for R' = 3, and $1.0 < E/E_o < 2.5$

$$f(E/E_o) = 1.52 - 0.95[-3.69 + 5(E/E_o) - (E/E_o)^2]^{1/2}, \quad (18b)$$

for R' = 10, and $0.05 < E/E_o < 1.0$

$$f(E/E_o) = 1.00 - 1.4251[0.85 - (E/E_o)]^2 , \quad (19a)$$

for R' = 10, and $1.0 < E/E_o < 2.5$

$$f(E/E_o) = 1.52 - 0.95[-3.69 + 5(E/E_o) - (E/E_o)^2]^{1/2} . \quad (19b)$$

These new expressions more closely reproduce the desired energy distribution shapes, in the author's opinion.

An equilibrium Maxwellian energy distribution function with $kT = E_o$ and normalized to the same under-curve area as Eqn. (18) such that

$$f(E/E_o) = 1.45(E/E_o)^{1/2} \exp(-E/E_o) \quad (20)$$

is graphed for comparison with Eqns. (18-19) in Fig. 6.

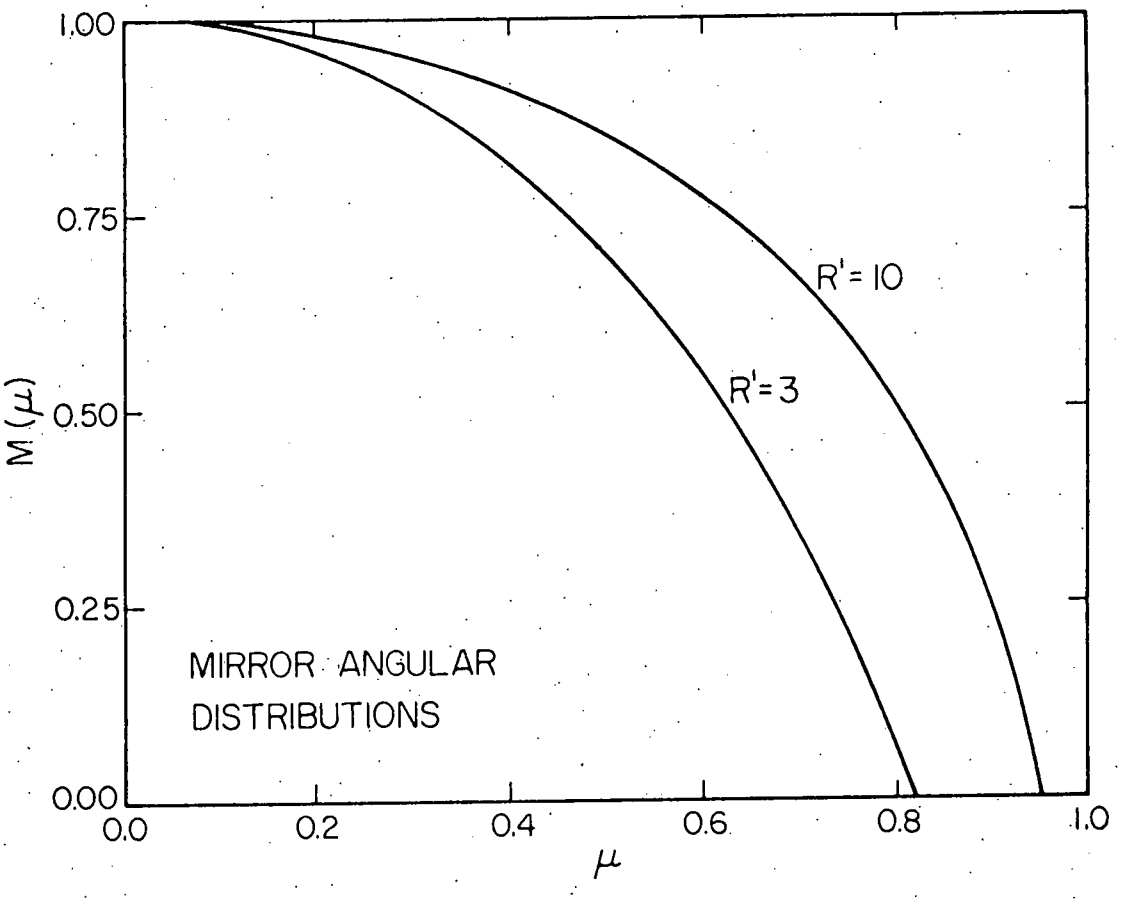

Figure 5. Angular component of the mirror loss-cone plasma phase-space distribution function vs. μ, the cosine of the angle θ from the magnetic axis, for two typical effective mirror ratios, i.e. R' = 3 and 10.

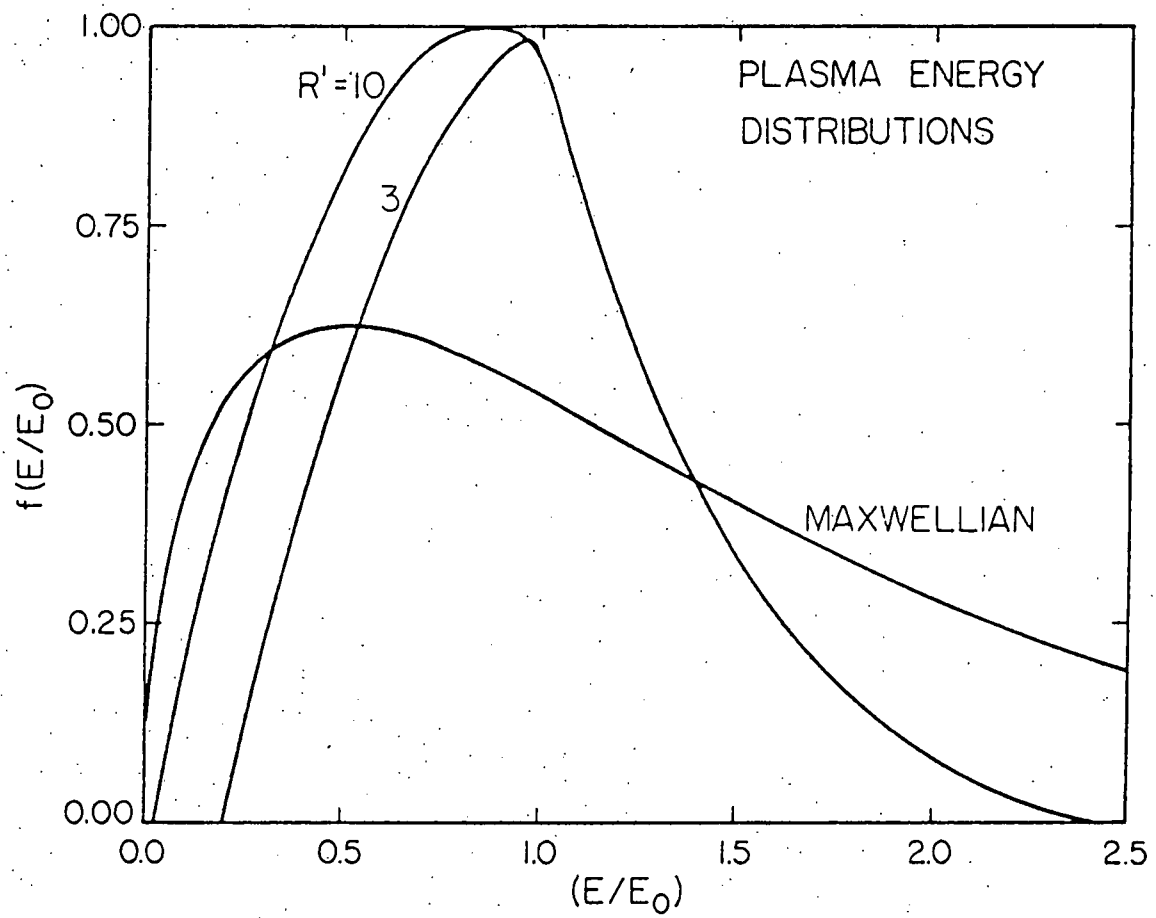

Figure 6. Energy component of the mirror loss-cone phase-space distribution for two typical effective mirror ratios, i.e. R' = 3 and 10. A Maxwellian distribution is shown for comparison.

G. Phase-Space-Averaged Cross Sections.

1. Method.

If, as is often the case, the speeds of the plasma particles are comparable to the test particle speed, it is necessary to average the cross sections over the plasma phase-space distribution to obtain the $\langle\sigma v\rangle$ rate coefficients for the interaction processes.

The formal definition of the rate coefficient begins by considering the distributions of two distinct particle species in 3-D phase space.[78] The first particle species has the number density n_1 and the velocity distribution $f_1(\vec{v}_1)$ such that the number of these particles in an incremental element $d\vec{v}_1$ is given by $n_1 f_1(\vec{v}_1)d\vec{v}_1$. These particles will interact with a number $n_2 f_2(\vec{v}_2)d\vec{v}_2$ of the second particle species in the element $d\vec{v}_2$ at the rate

$$dR = n_1 f_1(\vec{v}_1) n_2 f_2(\vec{v}_2)\ |\vec{v}_1 - \vec{v}_2|\ \sigma(|\vec{v}_1 - \vec{v}_2|)\ d\vec{v}_1 d\vec{v}_2 \qquad (21)$$

where $|\vec{v}_1 - \vec{v}_2|$ is the relative speed of the two interacting particles and $\sigma(|\vec{v}_1 - \vec{v}_2|)$ is the microscopic cross section (assumed to be functionally dependent upon the relative speed) for the reaction process under consideration.

The total reaction rate, R, is the sixfold integral over all space, viz.,

$$R = n_1 n_2 \int_{\vec{v}_1,\vec{v}_2} f_1(\vec{v}_1)\ f_2(\vec{v}_2)\ |\vec{v}_1 - \vec{v}_2|\ \sigma(|\vec{v}_1 - \vec{v}_2|)\ d\vec{v}_1 d\vec{v}_2. \qquad (22)$$

The multiple integral in the above expression may be interpreted as the interaction cross section averaged over the entire range of relative speeds, suitably weighted according to the distributions $f_1(\vec{v}_1)$ and $f_2(\vec{v}_2)$. This quantity is called the rate coefficient, $\langle\sigma v\rangle$, which is

defined as follows

$$\langle\sigma v\rangle \equiv \int_{\vec{v}_1,\ \vec{v}_2} f_1(\vec{v}_1)\ f_2(\vec{v}_2)\ |\vec{v}_1 - \vec{v}_2|\ \sigma(|\vec{v}_1 - \vec{v}_2|)\ d\vec{v}_1 d\vec{v}_2 \quad (23)$$

Now the reaction rate may be conveniently expressed as the product of the number densities of the dissimilar particles and the reaction coefficient, namely

$$R = n_1 n_2 \langle\sigma v\rangle \quad . \quad (24)$$

This should, of course, be consistent with the familiar form

$$R = \psi_1 \Sigma \quad (25)$$

where ψ_1 is a flux of test particles incident upon a target population with macroscopic cross section Σ. Equation (24) may be cast in the form

$$R = n_1 n_2 \langle\sigma v\rangle \frac{v_1}{v_1} \quad (26)$$

which, under the usual definition, $\psi_1 \equiv n_1 v_1$, becomes

$$R = \psi_1 n_2 \frac{\langle\sigma v\rangle}{v_1} \quad . \quad (27)$$

Thus, a generalized expression for the macroscopic interaction cross section is seen to be

$$\Sigma = n_2 \frac{\langle\sigma v\rangle}{v_1} \quad . \quad (28)$$

It may be remarked that in the cold plasma limit of $v_2 \ll v_1$, $\langle\sigma v\rangle$ reduces to σv_1 and the reaction rate again becomes

$$R = \psi_1 n_2 \sigma = \psi_1 \Sigma \quad (29)$$

as required by Eqn. (25).

In order to apply the formal definition of the general rate coefficient presented as Eqn. (23) above, it is necessary to perform some further manipulations. Consider a test particle characterized by

the velocity distribution $f_1(\vec{v}_1)$ as it travels through and interacts with a population of field particles with the distribution $f_2(\vec{v}_2)$. For a test particle with speed, v_t, and angular orientations, ϕ_t, and $\mu_t \equiv \cos\theta_t$, using the Dirac delta function and spherical coordinate system, the normalized test particle velocity distribution is

$$f_1(\vec{v}_1) = \frac{1}{v_1^2}\,\delta(v_1 - v_t)\,\delta(\phi_1 - \phi_t)\,\delta(\mu_1 - \mu_t) \quad . \tag{30}$$

The relative speed, $|\vec{v}_1 - \vec{v}_2|$, of the test particle and a field particle is given by

$$v_R \equiv |\vec{v}_1 - \vec{v}_2| = [v_1^2 + v_2^2 - 2v_1v_2\cos\gamma]^{1/2} \tag{31}$$

where γ is the angle between the two particles' velocity vectors and is given by

$$\gamma = \cos^{-1}\left[\mu_1\mu_2 + \sqrt{1-\mu_1^2}\,\sqrt{1-\mu_2^2}\,\cos(\phi_1-\phi_2)\right] \quad . \tag{32}$$

The incremental phase space elements are defined as follows

$$d\vec{v}_1 \equiv v_1^2 dv_1 d\phi_1 d\mu_1 \tag{33a}$$

$$d\vec{v}_2 \equiv v_2^2\, dv_2 d\phi_2 d\mu_2 \quad . \tag{33b}$$

Using Eqns. (30-33), Eqn. (23) may be rewritten in the form

$$\langle\sigma v\rangle = \int_{-1}^{+1}_{\mu_1}\int_{0}^{2\pi}_{\phi_1}\int_{0}^{\infty}_{v_1}\int_{-1}^{+1}_{\mu_2}\int_{0}^{2\pi}_{\phi_2}\int_{0}^{\infty}_{v_2} \frac{1}{v_1^2}\,\delta(v_1-v_t)\,\delta(\phi_1-\phi_t)\,\delta(\mu_1-\mu_t)$$

$$\times\, f_2(\vec{v}_2)\,[v_1^2 + v_2^2 - 2v_1v_2\cos\gamma]^{1/2}\,\sigma(v_R)\,v_1^2\,v_2^2$$

$$\times\, dv_2 d\phi_2 d\mu_2 dv_1 d\phi_1 d\mu_1 \quad . \tag{34}$$

This expression may be readily integrated over the subscript "1"

variables using the sifting property of the Dirac delta function to obtain

$$\langle\sigma v\rangle = \int_{-1}^{+1}_{\mu_2} \int_{0}^{2\pi}_{\phi_2} \int_{0}^{\infty}_{v_2} f_2(\vec{v}_2)\,[v_t^2 + v_2^2 - 2v_t v_2 \cos\Gamma]^{1/2}\sigma(v_R)\,v_2^2 \times dv_2 d\phi_2 d\mu_2 \tag{35}$$

where, from Eqn. (32), it is seen that

$$\Gamma = \cos^{-1}[\mu_t\mu_2 + \sqrt{1-\mu_t^2}\,\sqrt{1-\mu_2^2}\,\cos(\phi_t - \phi_2)] \tag{36}$$

and the cross section is evaluated such that

$$\sigma(v_R) = \sigma(|\vec{v}_t - \vec{v}_2|) \quad . \tag{37}$$

Also, Eqn. (35) must be normalized such that

$$\int_{-1}^{+1}_{\mu_2} \int_{0}^{2\pi}_{\phi_2} \int_{0}^{\infty}_{v_2} f_2(\vec{v}_2)\,v_2^2\,dv_2 d\phi_2 d\mu_2 = 1 \quad . \tag{38}$$

In order to make the integrations over the energy distributions of the previous section compatible with Eqn. (35), it is necessary to apply the transformation

$$\int_{(E/E_o)_{min}}^{(E/E_o)_{max}} f(E/E_o)\,d(E/E_o) = \int_{v_{min}}^{v_{max}} f(v^2/v_o^2)\,\frac{2v}{v_o^2}\,dv \tag{39}$$

where $E_o = \frac{1}{2} m_2 v_o^2$. Inspection of Fig. 6 suggests the limits of integration in Eqn. (39) to be

$$(E/E_o)_{min} = 0.18, \text{ for } R' = 3 \tag{40a}$$

$$= 0.04, \text{ for } R' = 10 \tag{40b}$$

$$(E/E_o)_{max} = 2.5, \text{ for both } R' = 3 \text{ and } 10. \tag{40c}$$

A FORTRAN program called MCSAVG has been developed which numerically integrates Eqn. (35). A three-dimensional version of the Gauss-Legendre quadrature technique is used to perform the required integrations. This method requires that a standard variable transformation of the form

$$F(x) = (b-a)\, F[a + (b-a)t]\, dt \qquad (41)$$

be applied to each of the phase-space dimensions in order that the integrations over the intervals [a,b] may be more conveniently performed over the unit interval [0,1]. Such data as mirror ratio, test and field particle identities, test particle velocity vector and magnetic field vector orientations, and plasma energy are set at the user's option. Specifications of either Maxwellian or mirror energy distributions and either isotropic or loss-cone angular distributions are also made. Program results are presented in tabular form as functions of test particle speed and kinetic energy. Once such rate coefficient tables are available for a series of representative parameters spanning the regimes of interest, an interpolation scheme may be employed to approximate intermediate values not themselves obtained by actual integration.

Use of the MCSAVG code is discussed in the Appendix. A FORTRAN listing of the code is available from the author on request.

2. Results.

Figures 7-8 depict ion-impact and charge-transfer rate coefficients calculated by MCSAVG according to Eqn. (35) above for the case of neutral deuterium test particles in a background of deuterium ions having the Maxwellian energy distribution of Eqn. (20) of the previous section and an isotropic [$M(\mu)=1$] angular distribution. E_o, the

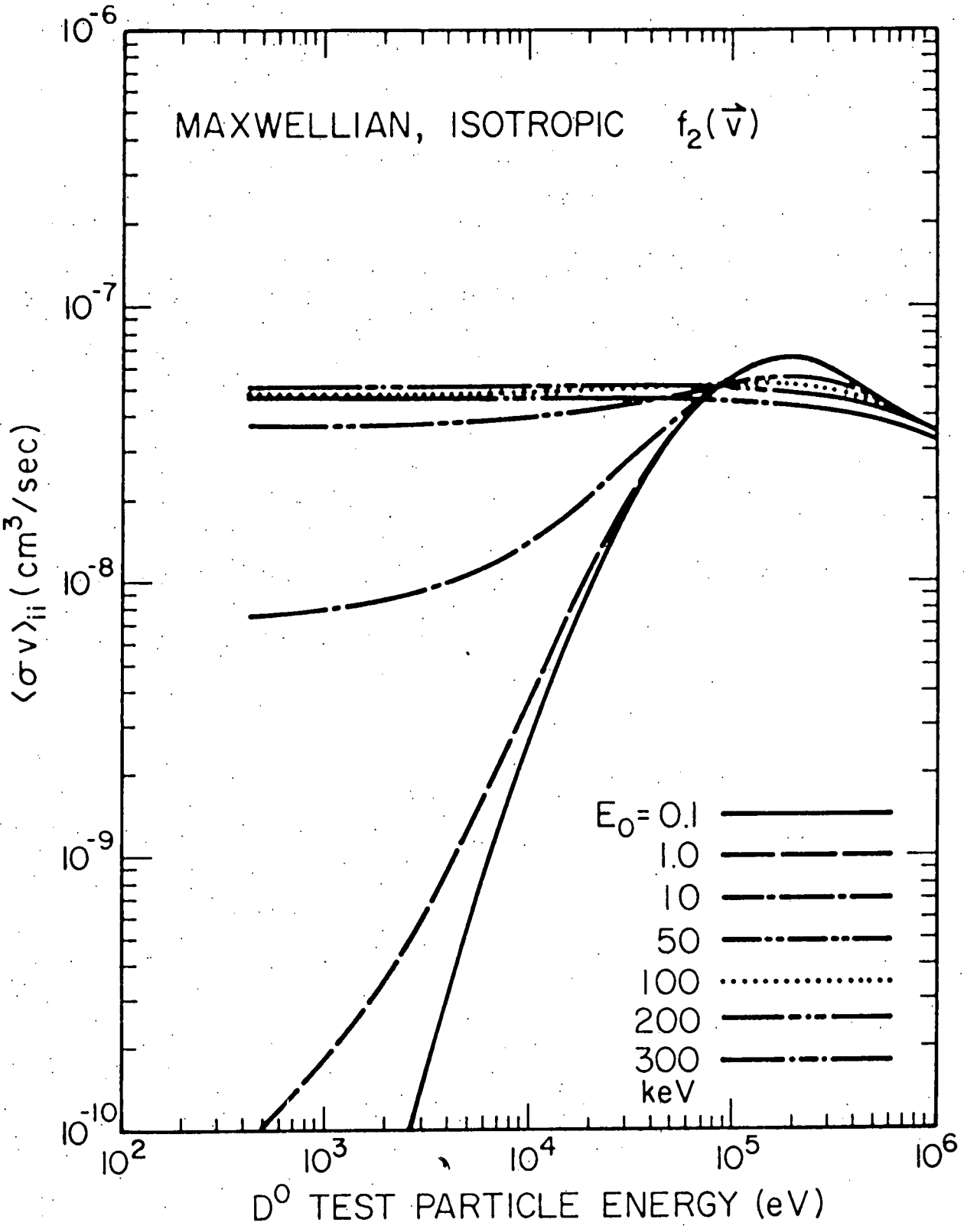

Figure 7. D-D ion-impact ionization rate coefficients as a function of neutral test-particle kinetic energy for a Maxwellian, isotropic plasma with various characteristic energies E_0.

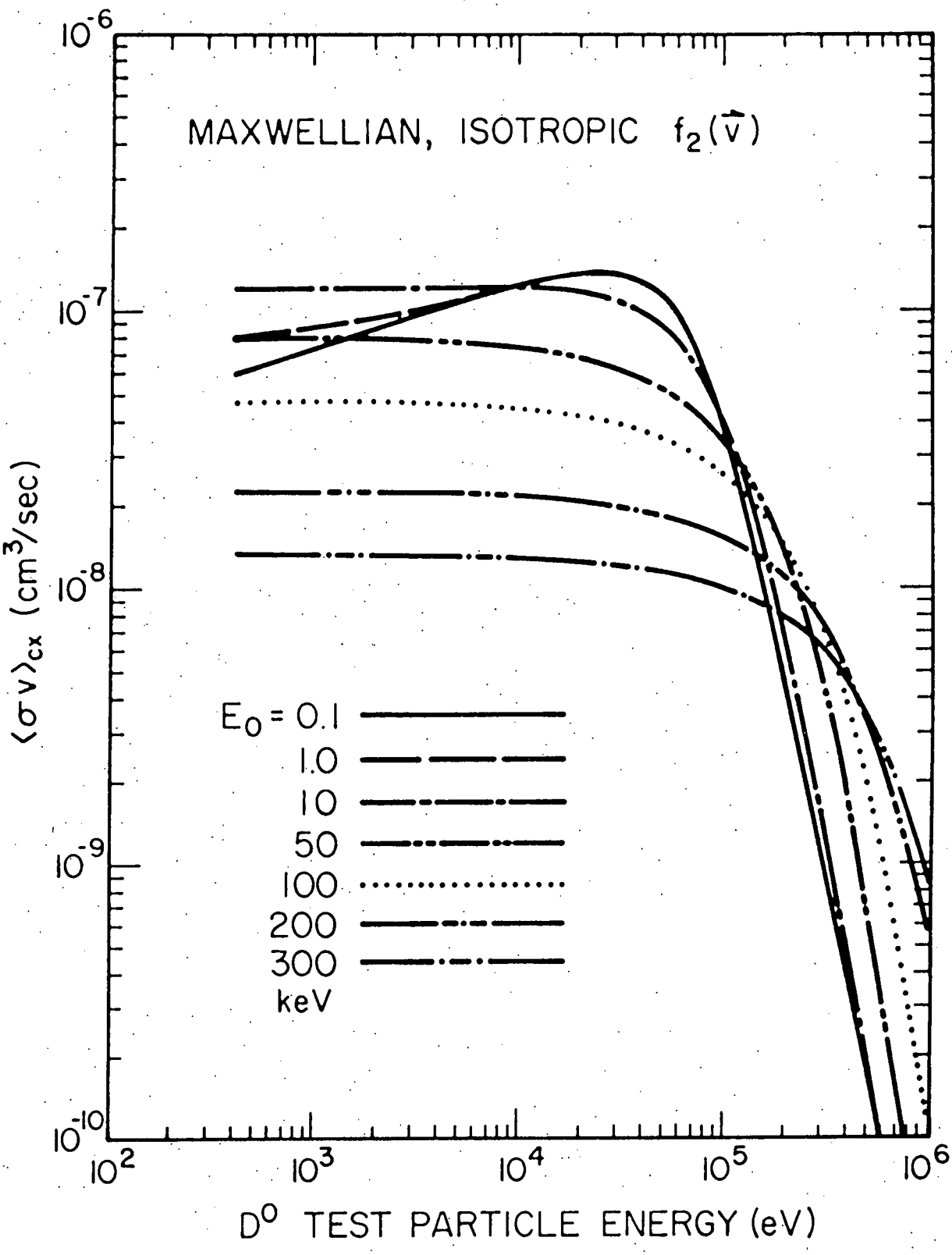

Figure 8. D-D charge-transfer rate coefficients as a function of neutral test particle kinetic energy for a Maxwellian, isotropic plasma with various characteristic energies E_0.

characteristic energy of the background distribution is varied as a parameter for representative values in the range [0.1 - 300 keV]. Results are plotted as a function of the D° test particle kinetic energy (eV). For values of E_o < 100 keV and test particle energies less than ~ 100 keV, charge transfer is the dominant processes. The ion-ionization rate coefficient is insensitive to the neutral test particle energy for E_o > 50 keV. For all values of E_o the charge transfer rate coefficient tends to fall off sharply for test particle energies in excess of 100 keV. Finally, for test particle energies < 10 keV both rate coefficients are rather strong functions of E_o.

In Figs. 9-10, the Maxwellian speed distribution has been replaced with the R' = 3 mirror loss-cone speed distribution of Eqn. (18). The isotropic angular distribution has been retained. The alternative speed distribution produces non-trivial changes in the resultant rate coefficients, suggesting the desirability of accurate representations of the plasmas used in neutral-particle transport calculations. As in Figs. 7-8 for very energetic test particles (i.e. those whose kinetic energy greatly exceeds E_o) the influence of the distributed plasma background becomes small and the rate coefficients tend toward asymptotic limits. For neutral test particles whose kinetic energy is much less than E_o the rate coefficients are depressed. For neutral test particle kinetic energies near E_o, the charge transfer rate coefficient can reflect the effect of increasing values of microscopic cross section for low relative energies seen in Fig. 4 and as well as the concentration of ions with energy near E_o seen in Fig. 6 such that the rate coefficient can increase significantly before ultimately falling off similar to the Fig. 7 result. In Figs. 7-10 as the test particle energy greatly

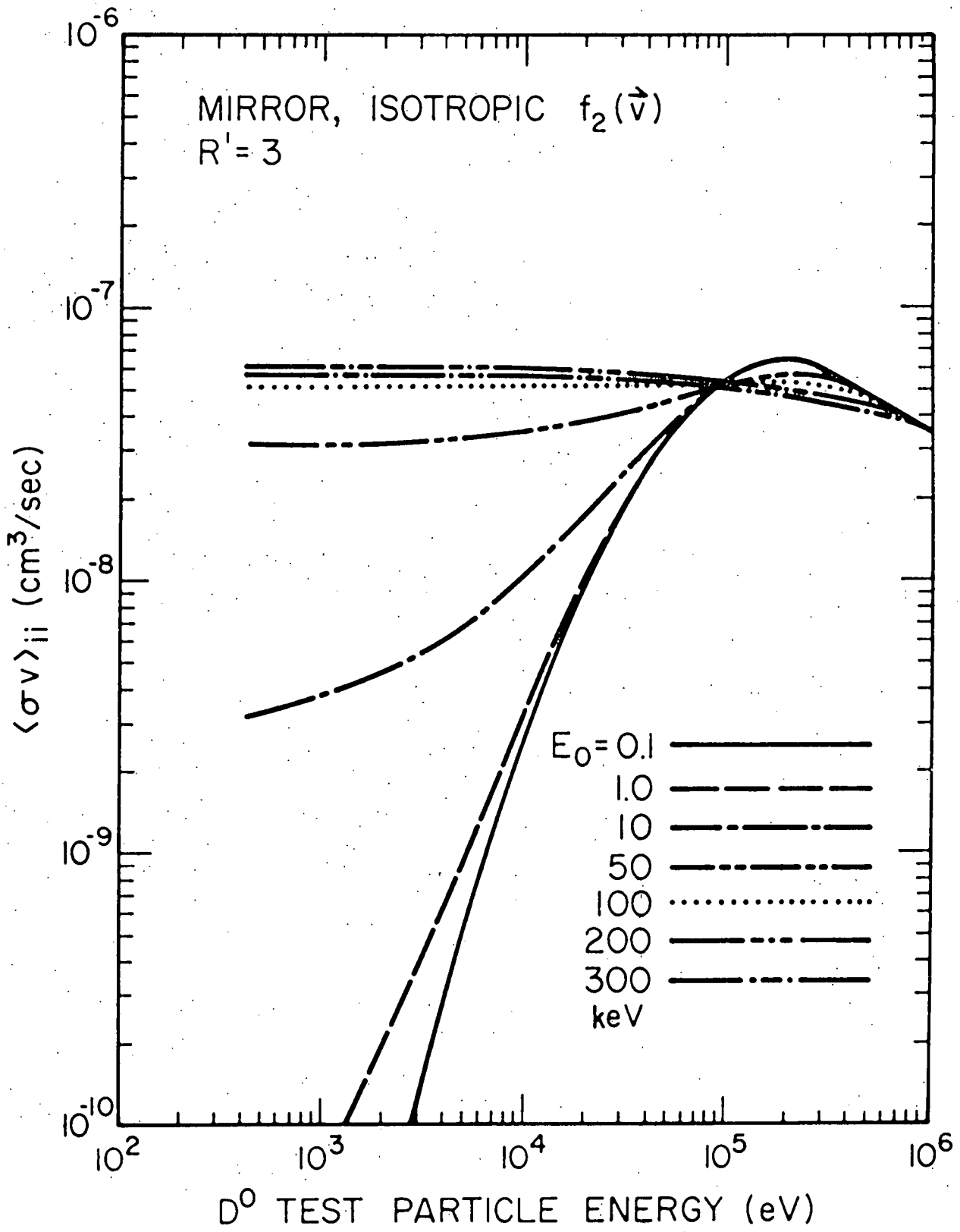

Figure 9. D-D ion-impact ionization rate coefficients as a function of neutral test-particle kinetic energy for a mirror loss-cone energy distribution for an effective mirror ratio R' = 3. The angular distribution was taken to be isotropic.

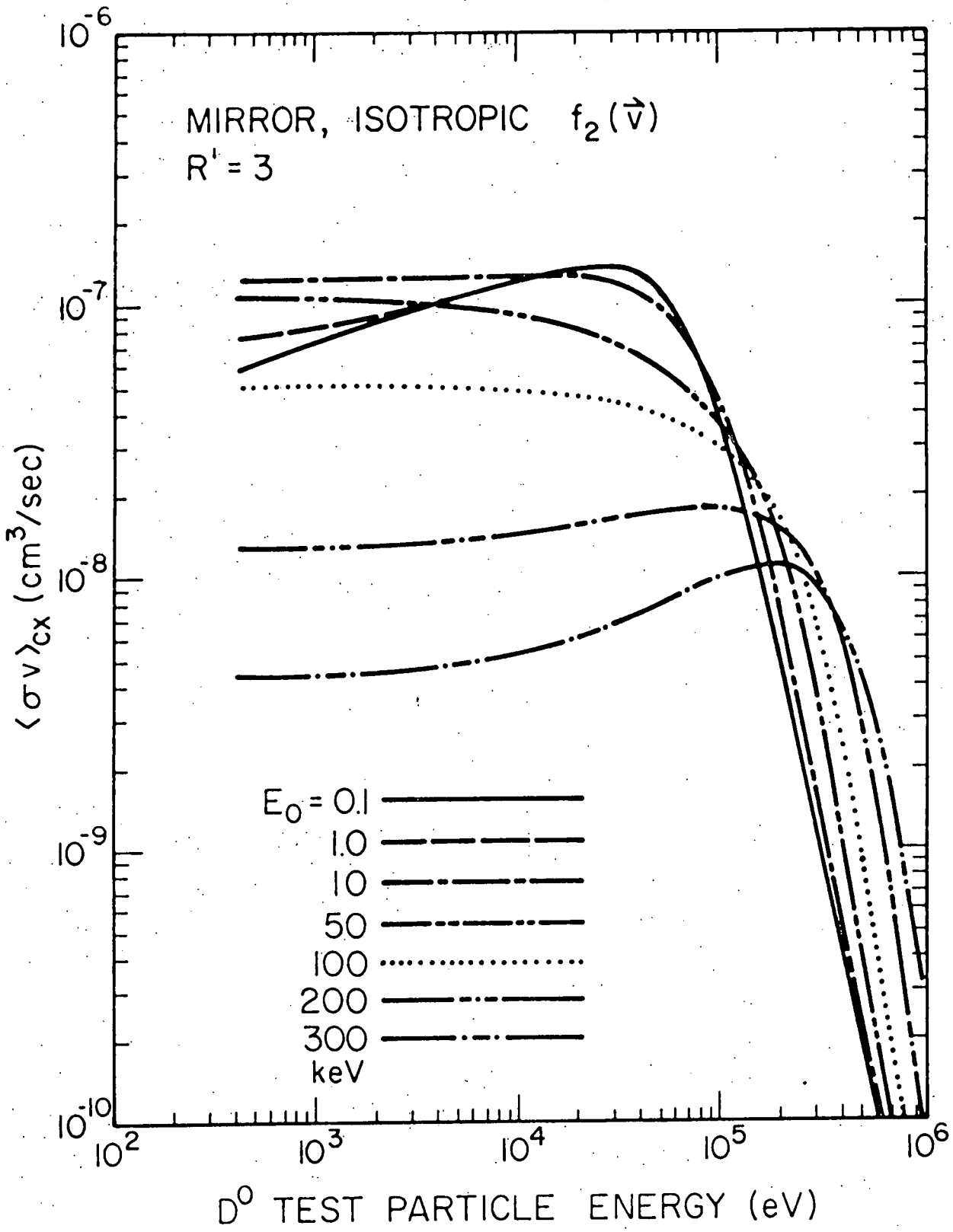

Figure 10. D-D charge-transfer rate coefficients as a function of neutral test particle kinetic energy for a mirror loss-cone energy distribution for an effective mirror ratio R' = 3. The angular distribution was taken to be isotropic.

exceeds E_o the average $\langle\sigma v\rangle$ tends toward the limit σv_t as expected. The isotropic results have been checked against LLL caluclations.[79] Qualitative confirmation of the 100 keV curve of Fig. 10 is also available.[80]

The ion-impact ionization results are not significantly affected by the next modification — the inclusion of the mirror loss-cone angular distribution. However, the charge-transfer rate coefficient, which incorporates a large contribution from those ions with velocity vectors close to that of the neutral test particle, is depressed when the neutral-particle orientation is within the loss cone (i.e. $\mu_o < \mu < 1$). For the particular case of $R' = 3$ ($\mu_o \sim 0.83$) and $E_o = 70$ keV, Fig. 11 plots the charge-transfer rate coefficient as a function of injection angle θ_i with respect to the magnetic axis of the system. Near-perpendicular injection tends to maximize the relative probability of charge transfer. The magnitude of the effect depends on the injection energy and is more pronounced for injection energies much greater than E_o, where the relative energy is more likely to lie in the sharply falling tail of the charge transfer cross-section curve of Fig. 4.

Taking the perpendicular injection case ($\theta_i = \pi/2$) the relative importance of the ion-impact ionization and charge-transfer processes as a function of injection energy is shown in Fig. 12 for the same particular case of $R' = 3$ and $E_o = 70$ keV. Reference 72 includes similar curves for other injection angles between 0 and $\pi/2$ radius. The charge-transfer rate coefficient exceeds that for ionization for injection energies < 70 keV. At higher injection energies than 70 keV the charge-transfer rate coefficient drops off sharply. The ion-impact ionization

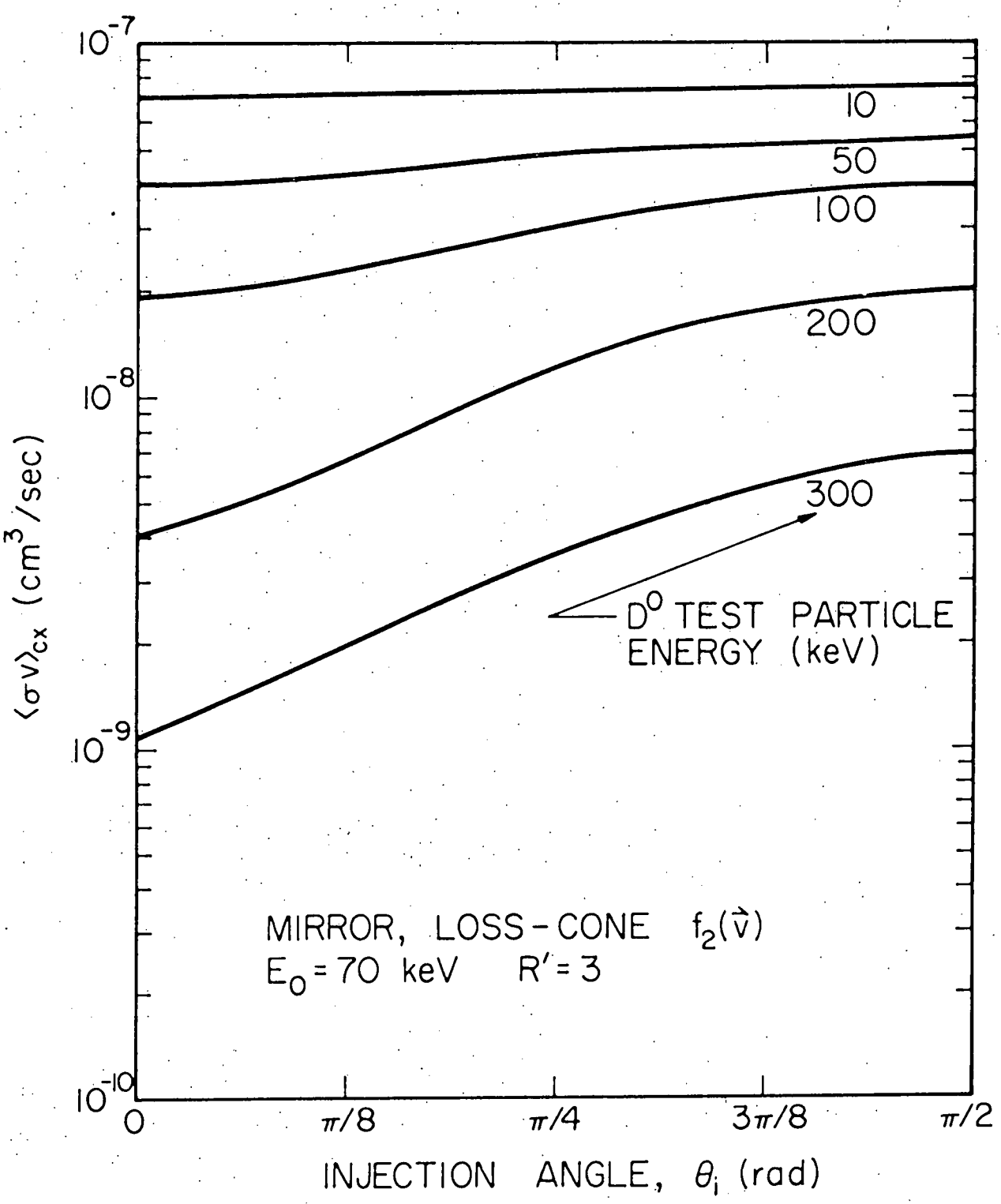

Figure 11. D-D charge-transfer rate coefficients as a function of injection angle θ_i with respect to the magnetic axis for a mirror loss-cone energy distribution for an effective mirror ratio R' = 3 and E_0 = 70 keV. Various injection energies in the range 10-300 keV are depicted. The ion-impact rate coefficients in contrast are insensitive to injection angle for all energies.

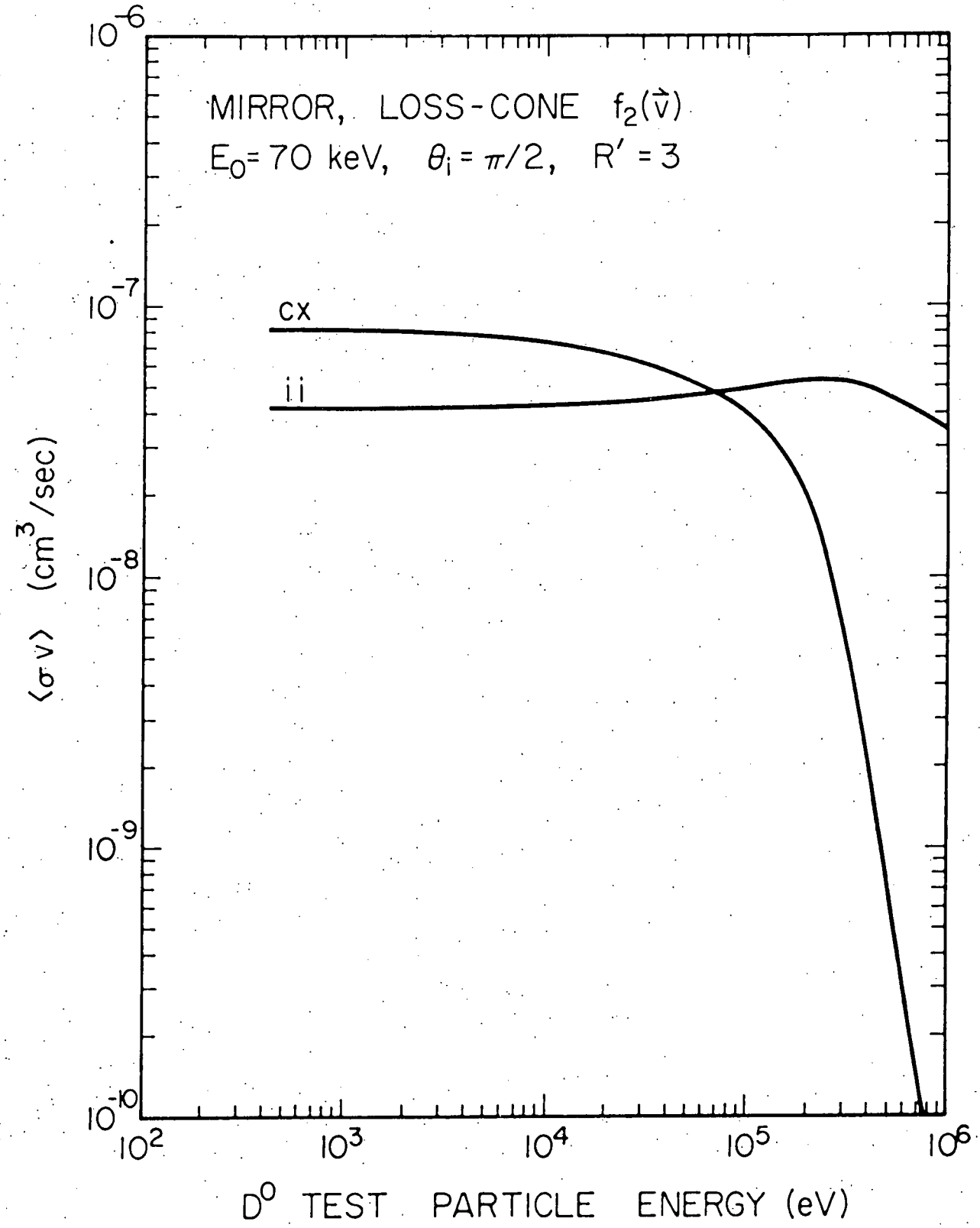

Figure 12. Comparison of D-D ion-impact ionization and charge-transfer rate coefficients for the case of perpendicular injection into a mirror loss-cone distributed plasma (in both energy and angle) with an effective mirror ratio R' = 3 and characteristic energy E_o = 70 keV as a function of injection energy.

curve is much less sensitive to the kinetic energy of the injected neutral test particle.

The final rate coefficient of interest is that for electron-impact ionization. The electrons are taken to have a Maxwellian energy distribution characterized by $\tilde{E}_e \ll E_o$ in a typical mirror machine. Since the mean electron speed is usually much greater than neutral test particle speeds the rate coefficients calculated according to Eqn. (35) are found to be essentially independent of the test particle speed. Figure 13 compares the result of A. Riviere[17] (solid curve above 10^3 eV) with the results of the present calculation (interpolated between three specific cases calculated). Above 10^3 eV, the region of interest to this study, both sets of results can be conveniently approximated by

$$\langle \sigma v \rangle_{ei} \approx 2.32(10)^{-6}\, \tilde{E}_e^{-0.347} \quad . \tag{42}$$

The solid curve has been extrapolated (the dashed portion) to energies below 10^3 eV, an energy region not considered by Riviere. Here, the Eqn. (42) approximation no longer well represents the results of the present calculation.

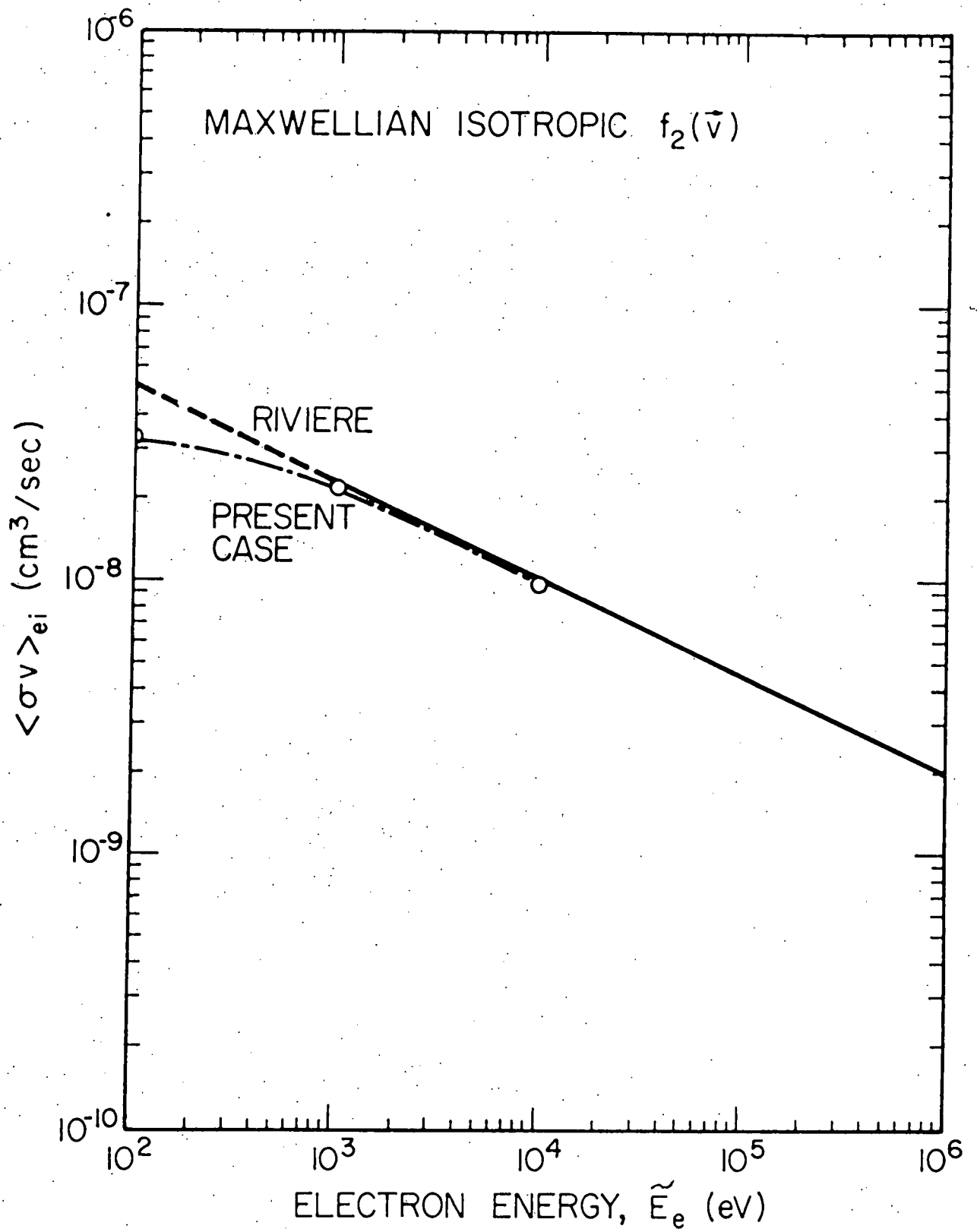

Figure 13. Rate coefficient for the electron-impact ionization of hydrogenic ions as a function of electron energy $\tilde{E}_e$. The Riviere result (Ref. 17) is compared with the MCSAVG calculation of the present study.

III. MONTE CARLO SIMULATION METHOD

A. Overview.

The Monte Carlo (MC) method can be described as a stochastic model of a mathematical or physical process "representing the solution of a problem as a parameter of a hypothetical population and using a random sequence of numbers to construct a sample of the population, from which statistical estimates of the parameter can be obtained."[81] Although antecedent work of a similar nature can be identified[9,81] the contemporary use of the method and its name can be traced to Manhatten Project activities at the Los Alamos Laboratory in the mid-1940's.[82] Development of the method has been rapid and extensive, particularly in the area of neutron and photon transport studies, and its growing popularity parallels the progress made in the availability of advanced high-speed computers.[81-88]

The transport of neutral particles in a plasma medium is analogous to the transport of neutrons in a fission reactor medium. First, the interaction of the test-particle population with the background plasma can be represented by the superposition of individual projectile-target collisions. This follows from the screened Coulomb potential of the neutral particles which makes the relevant interactions (see Chapter II) "short-range" with respect to the characteristic interparticle distances in the plasma. The density of neutral projectile particles is small enough that self-interactions and collective effects involving neutral particles are ignored. This allows for the sequential, one-at-a-time treatment of individual neutral-particle histories. Second, for neutrons in a fission reactor, a distinction is made between absorption and scattering interactions. For neutrals in a plasma background, the

analogous absorption interactions are the ionization collisions, which remove particles from the projectile population and integrate them into the background medium. Conventional scattering collisions have their analog in the charge-transfer collisions, which effectively make test particles "jump" from one point in phase-space to another. Finally, between successive collisions, if gravitation and higher-order electric and magnetic moments of the neutral particles are neglected as is the usual practice, there are no forces acting on the neutrals. Thus, as for neutrons, the consequent particle motion is characterized by constant velocity such that the overall trajectory is composed of a series of connected line segments where scattering collisions provide the transitions between successive legs. The neutral particle history terminates in either an ionization collision or escape from the finite plasma and bombardment of the first wall.

Recognition[89] of this essential correspondence between the neutron and neutral transport phenomena has recently led to attempts to apply computational techniques originally developed for neutron and gamma-ray studies to plasma applications.[90-94] The MC method has been the technique selected for this[95-98] and subsequent[24-26,99] studies. All of these applications may be interpreted as treatments of various forms of the Boltzmann transport equation.[89] This study treats the steady-state linear transport problem wherein the assumed plasma background is held fixed. A self-consistent adjustment of plasma conditions would require a more general, nonlinear treatment. The MC approach is of particular interest to the study of mirror systems in that incorporation of complicated geometries and known phase-space anisotropies is possible.

The definition of the MC method at the outset of this section mentions the requirement of a random sequence of numbers. In standard practice the procedure is to call upon the system software of the computer being used for the MC simulation to generate on demand a sequence of pseudo-random numbers distributed uniformly on the real unit interval [0,1]. Suitable mathematical transformations are then made to sample the appropriate probability density functions. The sequence of random variables thus obtained should satisfy the additional requirements that the cycle length of the sequence is long compared to the demands of the particular problem at hand and that there are no significant serial correlations between any particular "random" number ξ_n and ξ_{n+k} for k = 1,2,3,... The subject of pseudo-random number generation is in itself a large research field[100-105] and will not be treated in any more detail here. The ability to use one of these algorithms to recreate the sequence of random numbers is an advantage in debugging the MC code, it should be noted.

The remainder of this chapter will describe in detail the specific MC techniques invented or adapted for use in this study. These include the techniques for neutral-test-particle tracking, choosing the charge-transfer "scattering" angle using a rejection technique, reducing the statistical variance of the results, incorporation of the rate coefficient results of Chapter II, and monitoring the convergence of the results. The NUBIN code package thus developed becomes the first tool capable of treating the effects of three spatial dimensions and the plasma phase-space anisotropies expected in mirror fusion systems. The availability of results from this code makes meaningful engineering

calculation (such as those of Chapter VI) possible for use in the design of these systems.

B. Neutral Test-Particle Tracking.

The basic mechanism of the MC simulation is the tracking of neutral test-particle histories from some specified source through a series of interactions with the background plasma to eventual termination in either ionization or escape from the finite plasma. The neutral test particles are advanced through the plasma along a sequence of connected line segments from interaction point $P(X_i, Y_i, Z_i)$ to $P(X_{i+1}, Y_{i+1}, Z_{i+1})$ until a termination condition is satisfied. The initial point $P(X_o, Y_o, Z_o)$ represents the source. Figure 14 illustrates a typical test-particle history. The neutral particle is injected along the vector $\vec{I}(\theta, \phi)$ into the spherical target plasma with radius R_p centered at P(a, b, c). The angle α indicates the possible finite angular divergence of the beam. The plasma is arbitrarily partitioned into subregions (cells) of radius r_1 and $r_2 = R_p$ so that internal distributions of events (e.g., the radial profile of beam trapping) may be resolved. In actual practice more than two such cells would generally be used. In the nonanalog simulation scheme discussed in the next section, the particle is initially assigned a weight-value $W_o = 1$, which is adjusted at each interaction point (indicated by the closed circles labeled 1, 2 and 3 in Fig. 14) to reflect depletion of the beam by ionization. At each such interaction a new test-particle velocity vector is obtained by sampling from the ion population to represent the trajectory of a charge-transfer-produced neutral. A bookkeeping procedure monitors the crossing of boundaries (indicated by the open

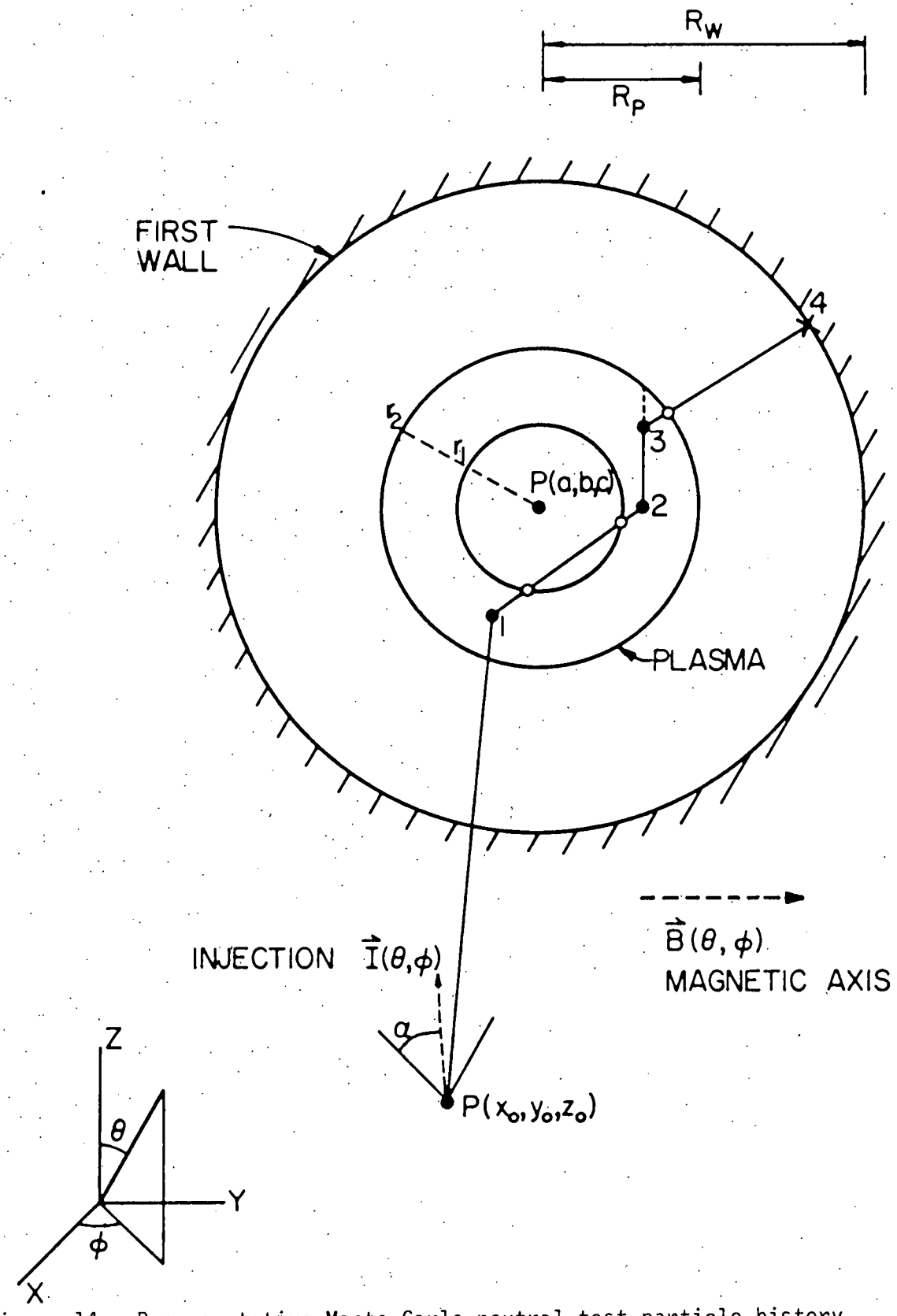

Figure 14. Representative Monte Carlo neutral test-particle history in an idealized fusion reactor configuration.

circles in Fig. 14) until the test particle escapes the plasma and is extrapolated to impact the first wall at radius $R_w > R_p$ (point 4 in Fig. 14). The remaining weight-value W_4 represents the estimate of the inefficiency of the beam trapping. Many such histories are followed to give the aggregate statistical picture desired. A convergence criterion is discussed in Sect. 6 below.

As the neutral test particle moves through the plasma a distance s, the probability that an interaction will occur in the incremental distance ds at s is equal to Σds. Here Σ is the total macroscopic interaction cross section previously defined as Eqn. (28). Σ could well be dependent upon local plasma properties as s varies but for the present illustration Σ is assumed to be spatially uniform. The probability f(s)ds that a test particle will have its first interaction in ds at s is equal to the product of the probability that the test particle reaches s without interaction and the probability that an interaction will occur in the incremental distance ds, which gives the exponential density function

$$f(s) = \begin{cases} \Sigma e^{-\Sigma s}, & 0 \leq s \leq \infty \text{ , } \Sigma \text{ constant} \\ 0 \quad , & s < 0 \end{cases} . \tag{43}$$

The cumulative distribution function F(s) is defined in the usual manner

$$F(s) = \int_{-\infty}^{s} f(s')ds' \quad . \tag{44}$$

For this case

$$F(s) = \begin{cases} 1-e^{-\Sigma s}, & s \geq 0 \\ 0 \quad , & s < 0 \end{cases} . \tag{45}$$

To select analog samples from f(s) the inversion technique[88] is employed. That is the equation

$$\xi = F(s) = 1 - e^{-\Sigma s}, \quad s \geq 0 \tag{46}$$

is solved for s as a function of ξ such that

$$s = -\Sigma^{-1} \ell n(1-\xi) \quad . \tag{47}$$

If pseudorandom numbers ξ_i distributed uniformly on the unit real interval [0, 1] are substituted into the righthand side of Eqn. (47), the corresponding values of s_i will be exponentially distributed over the semi-infinite interval $0 \leq s \leq \infty$. Further, since the sequence $(1-\xi_i)$ is random if and only if the corresponding sequence ξ_i is, Eqn. (47) may be rewritten

$$s_i = - \Sigma^{-1} \ell n(\xi_i) , \quad i = 1,2,3,... \quad . \tag{48}$$

In general the macroscopic cross section Σ may functionally depend upon s through Eqn. (28) if n=n(s) such that Eqn. (43) becomes

$$f(s) = \begin{cases} \Sigma(s) \exp\left(- \int_0^s \Sigma(s')ds'\right) , & 0 \leq s \leq \infty \\ 0 , & s < 0 \end{cases} \quad . \tag{49}$$

In contrast to the inversion procedure used to obtain Eqn. (47) from Eqn. (44), the distribution function F(s) obtained from Eqn. (49) may be awkward or impossible to treat similarly. An alternative sampling procedure has therefore been implemented in the NUBIN code in which a nonanalog (i.e. weight estimators, not individual particle histories, are propagated through the simulation) scheme samples the distance to collision for arbitrary $\Sigma(s)$ along the test particle trajectory and yields an unbiased estimate of the true number of collisions. The extensive discussion of this approach found in Reference 106 will not be recapitulated here. Figure 15 illustrates the procedure for

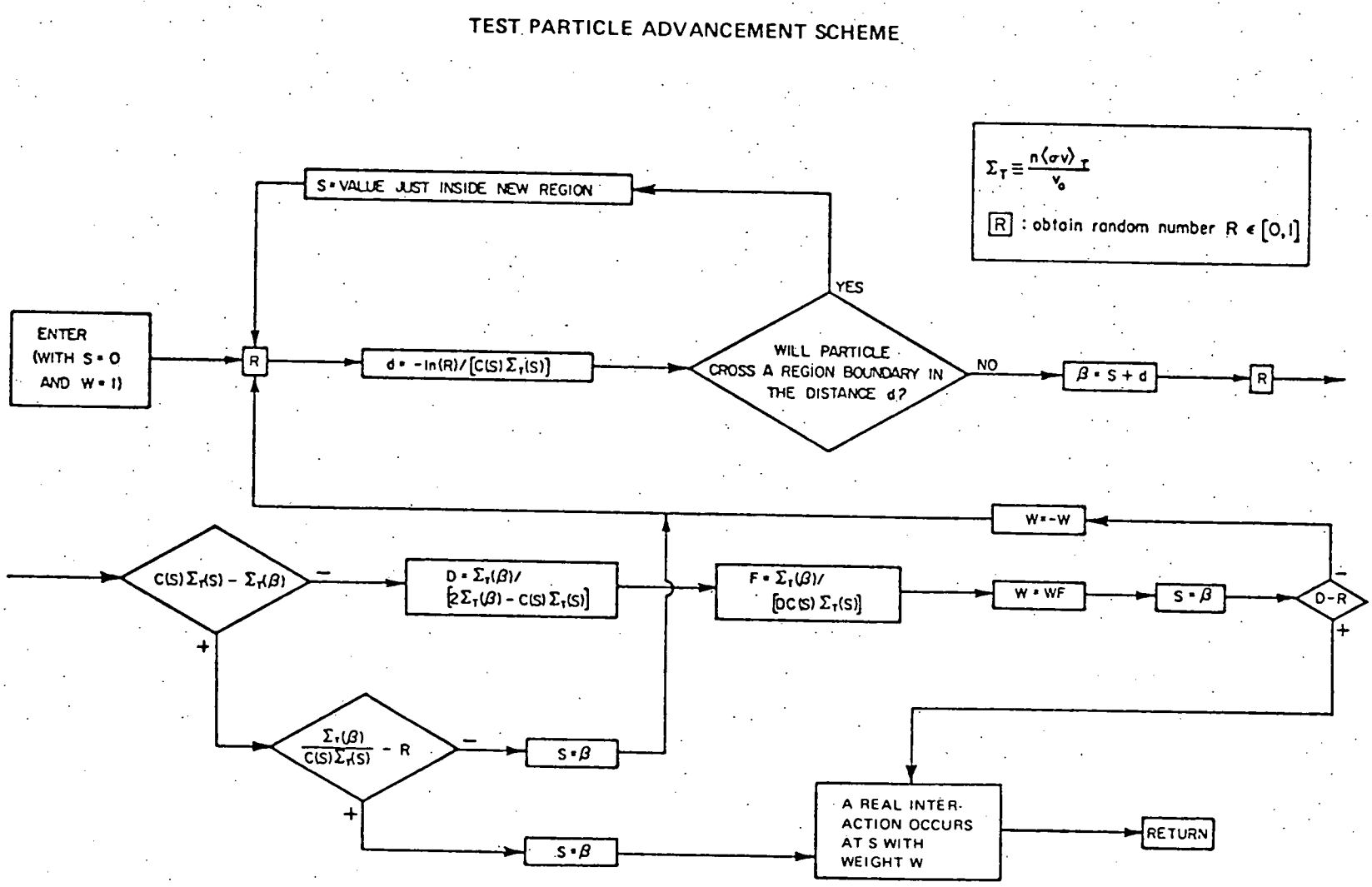

Figure 15. Nonanalog scheme for sampling the distance to collision s for an arbitrarily varying macroscopic cross section Σ. (Ref. 106)

sampling the distance to collision s. The scheme involves a) sampling the distance to a tentative collision point using a constant cross section $C(x)\Sigma(x)$, where x is the current test particle position and $C(x)$ is an appropriately chosen sampling multiplier, b) advancing the test particle to the tentative collision point, c) possibly altering the particle's weight-value W, and d) either accepting the tentative collision point as a "real" interaction point or rejecting the tentative collision point and returning to a) above to sample a new tentative collision point and repeat the process. For the case of $\Sigma(x)$ = constant and $C(x) = 1$ this scheme reduces to the usual analog method. The values of $C(x)$ are assigned to each plasma subregion (see Fig. 14) in a manner which attempts to optimally resolve the tradeoff between the possible introduction of increased variance at small $C(x)$ values and increased computation time at large $C(x)$ values.[106]

A current interaction point $P(X_{i+1}, Y_{i+1}, Z_{i+1})$ is determined to the previous interaction point by the standard geometric relations

$$X_{i+1} = X_i + s\ell \tag{50a}$$

$$Y_{i+1} = Y_i + sm \tag{50b}$$

$$Z_{i+1} = Z_i + sn \quad . \tag{50c}$$

The quantities ℓ, m, n are the direction cosines of the test particle velocity vector, which in terms of the spherical coordinates θ and ϕ are given by

$$\ell = \sin\theta\cos\phi \tag{51a}$$

$$m = \sin\theta\sin\phi \tag{51b}$$

$$n = \cos\theta \quad . \tag{51c}$$

The distance to the interception of the plasma boundary is found by

substitution of Eqns. (50a-c) into the equations describing the plasma surface (see Sect. A-2 of Chapter IV) and solving for s.

C. Rejection Techniques.

Once a neutral test particle has been advanced to a "real" interaction point using the procedure described in the previous section, it becomes necessary to select a suitable charge-transfer interaction partner from the background ion population. This is accomplished using a multidimensional rejection sampling[88] from the probability density function

$$f(v, \mu, \phi) = \frac{K\, f(v^2/v_p^2)\, M(\mu)\, \sigma_{cx}(v_R)\, v_R\, (v/v_p^2)}{\langle \sigma v \rangle_{cx}} \qquad (52)$$

where K = a normalization constant

$f(v^2/v_p^2)$ = the ion energy distribution function from Eqns. (18-20)

$M(\mu)$ = the plasma angular distribution function from Eqn. (16)

v_R = the relative collision speed

$\sigma_{cx}(v_R)$ = the microscopic charge-transfer cross section from Eqn. (10).

This particular density function incorporates the relevant charge-transfer collision physics in that those ions with velocity vectors tending to maximize $f(v, \mu, \phi)$ will be preferentially selected. Also, since it is assumed that no ions still in the system are in the loss-cones, no charge-transfer neutrals will be produced with velocity vectors in the loss cones. Thus, the anisotropy of the plasma will have considerable influence on the neutral-particle bombardment of the first wall.

Sampling is accomplished by choosing the four pseudo-random numbers ξ_1, ξ_2, ξ_3 and ξ_4 from [0, 1] and interpreting $P[X, Y, Z] \equiv P\ [a +$

$\xi_1(b-a)$, $c + \xi_2(d-c)$, $e + \xi_3(f-e)$, ξ_4] as a point lying in the hypercube containing $f(v, \mu, \phi)$ such that $a \leq v \leq b$, $c \leq \mu \leq d$, $e \leq \phi \leq f$ and $0 \leq \xi_4 \leq 1$. If $\xi_4 < f(X, Y, Z)$, then $P(X, Y, Z)$ is accepted as a sample from $f(v, \mu, \phi)$; if not, the process is repeated until a sample has been obtained successfully. The term "rejection technique" is applied because not all generated samples are used. The computational inefficiency of rejecting samples is tolerable if the average work required per sample is less than that which would be required to obtain samples from an alternative numerical inversion technique, if such exists. In the MC code NUBIN this rejection procedure is conducted by SUBROUTINE REJECT, the computational flow of which is illustrated in Fig. 16.

The successful triplet (X', Y', Z') is used to determine the corresponding values of (v', μ', ϕ') which define the velocity vector of the sampled ion participating in the charge-transfer collision. Under the assumption that no momentum is transferred in such collisions the ion (now neutralized) will continue to move with that same velocity. This new neutral is now taken to be the test particle of interest and followed along its trajectory to a subsequent interaction. At each interaction the weight-value is adjusted to reflect local ionizational trapping by the updating procedure

$$W_{i+1} = W_i \left[\frac{\langle \sigma v \rangle_{cx}}{\langle \sigma v \rangle_{ei} + \langle \sigma v \rangle_{ii} + \langle \sigma v \rangle_{cx} + \langle \sigma v \rangle_{RS}} \right] . \qquad (53)$$

For large-angle Rutherford scattering collisions a similar procedure is established using a version of Eqn. (52) wherein σ_{RS} and $\langle \sigma v \rangle_{RS}$ are substituted for σ_{cx} and $\langle \sigma v \rangle_{cx}$, respectively. Once the cosine of the

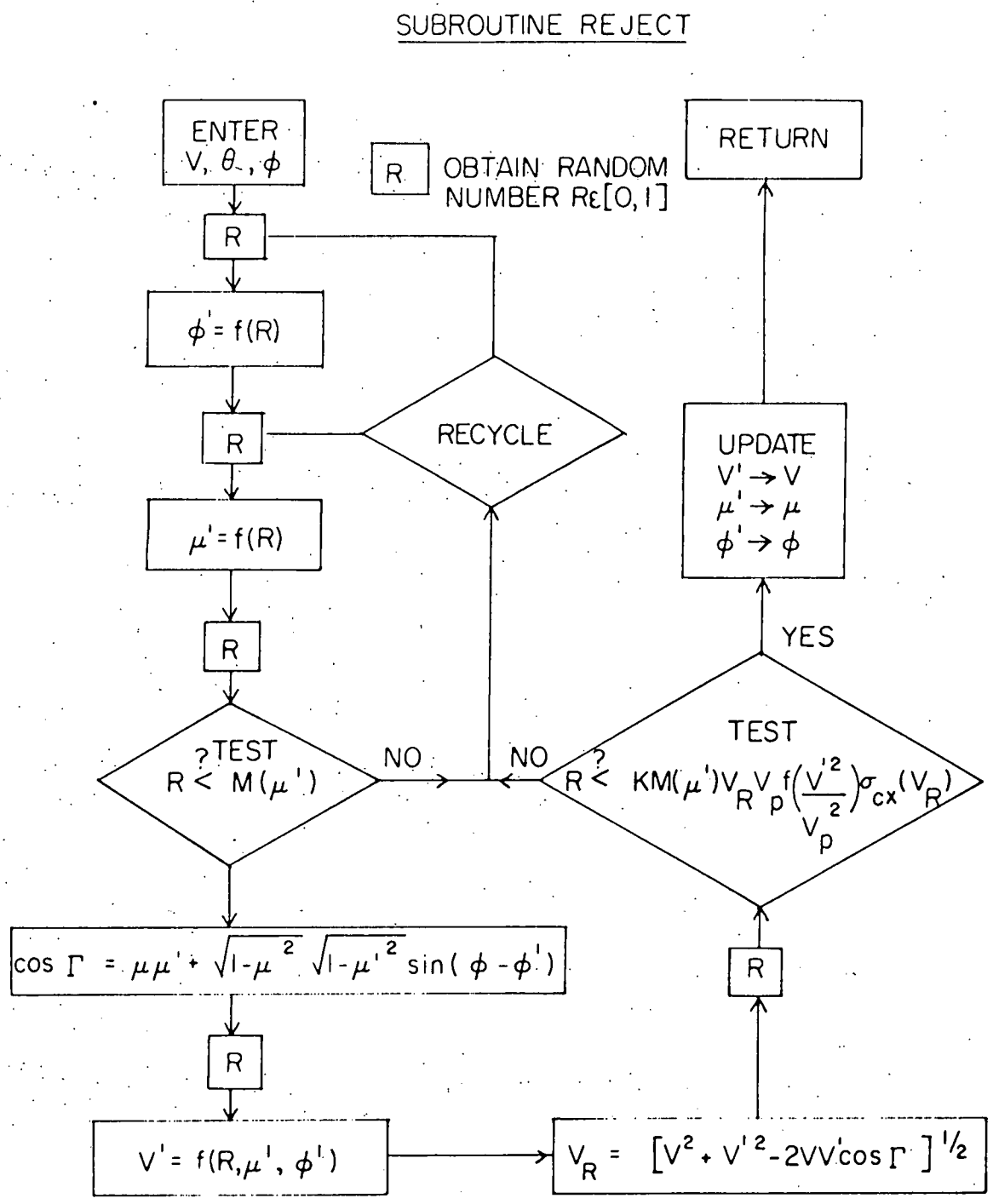

Figure 16. Computational flow diagram for SUBROUTINE REJECT of the NUBIN code. REJECT performs a rejection sampling of the plasma ion phase space distribution to obtain the trajectory of a charge-transfer-produced neutral atom.

polar angle of scattering μ is selected the direction cosines of the scattered neutral (α', β', γ') can be obtained from the initial direction cosines (α, β, γ) using the standard coordinate transformation illustrated in Fig. 17.

At various stages of the simulation, the cosine and sine of an angle δ uniformly distributed on the interval [0, 2π] are needed for Eqn. (51) above. Rather than processing a randomly selected δ into sophisticated and time-consuming trigonometric routines, the cosine and sine are obtained by a rejection technique suggested by J. von Neumann.[83] This technique, implemented in the SUBROUTINE RANGLE of the NUBIN code is schematically illustrated in Fig. 18. The efficiency of this technique is $\pi/4$; that is, $4/\pi$ pairs of pseudo-random numbers must be sampled for each acceptable cosine-sine pair produced.

D. Variance Reduction.

Since the results of any MC calculation are subject to statistical uncertainty as measured by the variance σ^2 about the estimator taken to represent the true value of the parameter under investigation, a key area of concern to researchers dating to the early days of MC work has been the invention of techniques designed to minimize the variance for a given amount of computational effort (time) invested in the simulation.[9] The brute-force alternative, since the variance is inversely proportional to the sample size, has been to increase the number of samples. This approach is both inefficient and inelegant.

The greatest gains in variance reduction are obtained by exploiting specific details of the problem at hand.[107] A dilemma is thus encountered in a new application of MC techniques such as this one. The

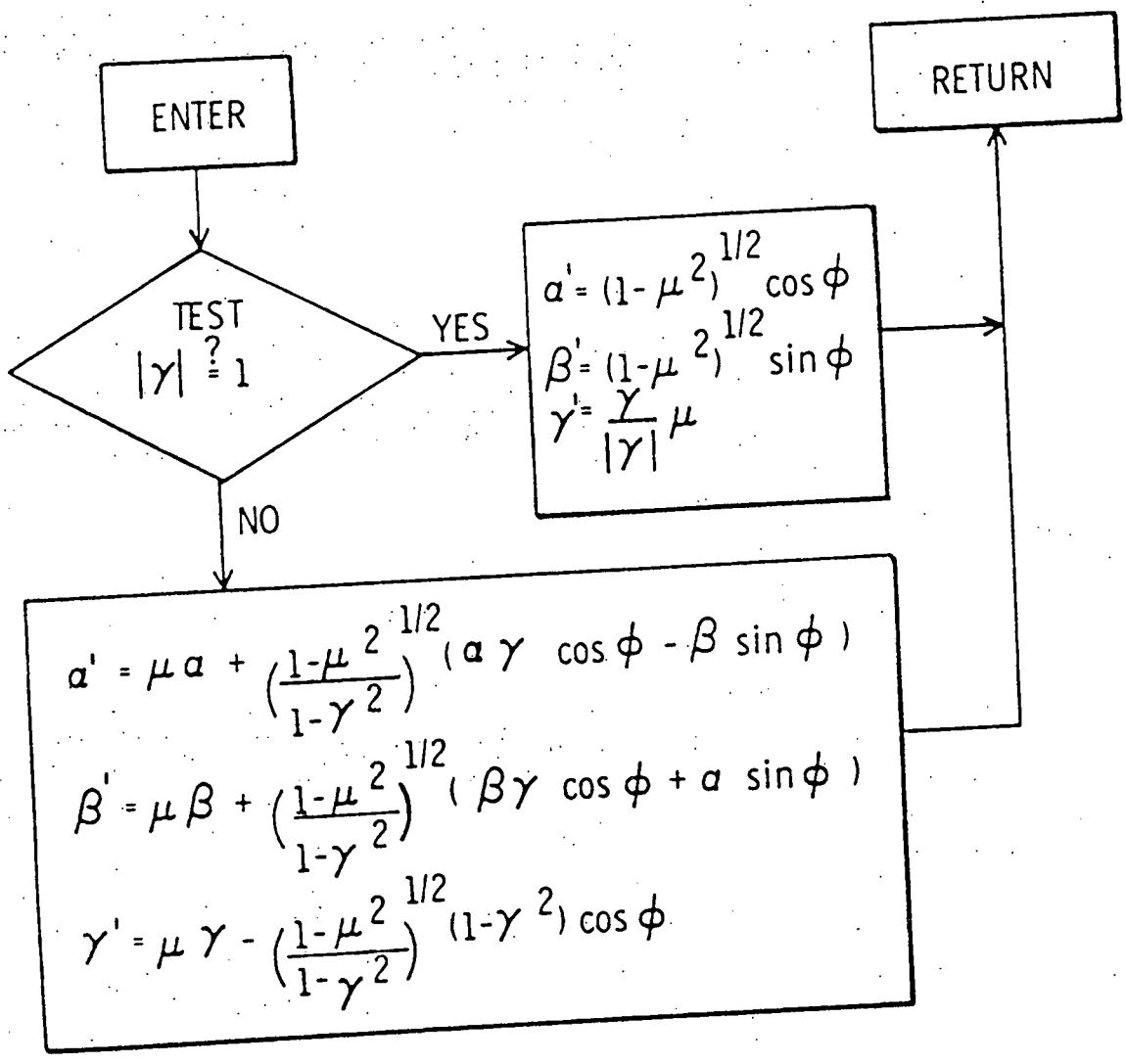

Figure 17. Coordinate transformation used to obtain the direction cosines (α',β',γ') for a neutral test particle scattered through an angle with cosine μ from an original trajectory denoted by (α,β,γ).

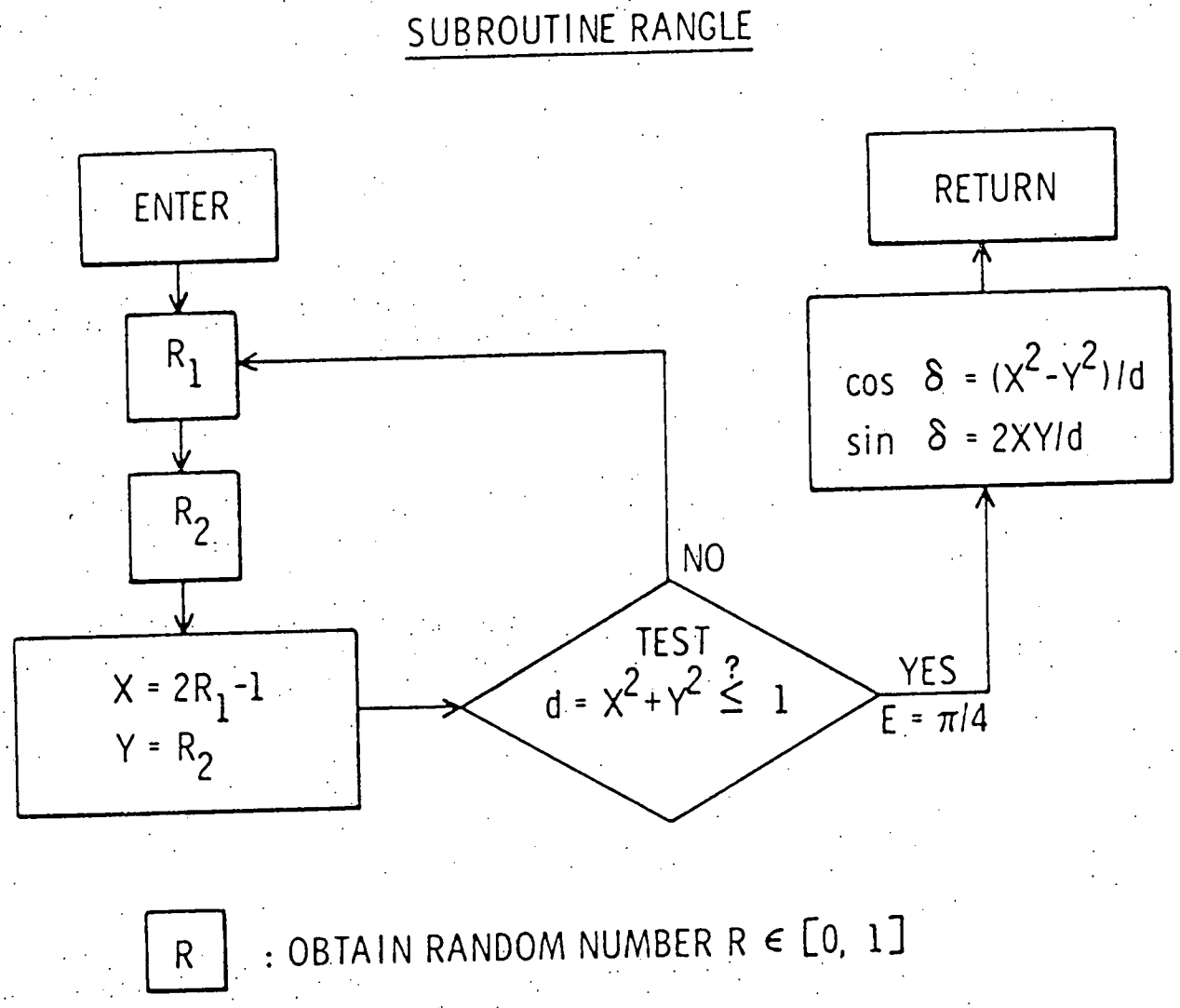

Figure 18. Rejection technique for obtaining the cosine and sine of an angle distributed randomly on the interval $[0,2\pi]$ (von Neumann, Ref. 83).

characterization of the problem is too new to start manipulating the model in order to apply sophisticated variance reduction techniques[9, 107-110] when the specific features of the physical problem which are transformed by these techniques may soon be superceded by newer physics. At the same time the advantages and savings to be gained justify the incorporation of at least some variance reduction effort even at this early stage. One approach found to be compatible with features already in the simulation code is the traditional "Russian Roulette" technique.[111] This procedure was therefore incorporated into the NUBIN code as SUBROUTINE RUSRLT and is described by Fig. 19. If a neutral test particle history is followed long enough the weight-value being carried along will eventually be so depleted that no matter what the particle does thereafter, the overall simulation result will scarcely be affected. The computation effort required to continue the particle tracking remains undiminished, however. Thus at each interaction point when the weight value has been reduced by the continuation (nonabsorption) probability

$$P_c = \left[\frac{\langle \sigma v \rangle_{cx} + \langle \sigma v \rangle_{RS}}{\langle \sigma v \rangle_{ei} + \langle \sigma v \rangle_{ii} + \langle \sigma v \rangle_{cx} + \langle \sigma v \rangle_{RS}} \right] , \qquad (54)$$

the new weight-value is tested against a critical weight-value $W_{cr} << 1$ specified by the code user. If the weight-value W exceeds the value W_{cr} the history is continued unmolested. If on the other hand $W < W_{cr}$ the Russian Roulette procedure is invoked by a supplementary game of chance under which the test particle weight-value is reset to unity with probability W and terminated in favor of the next source particle with probability (1-W). The average weight continued is still W.

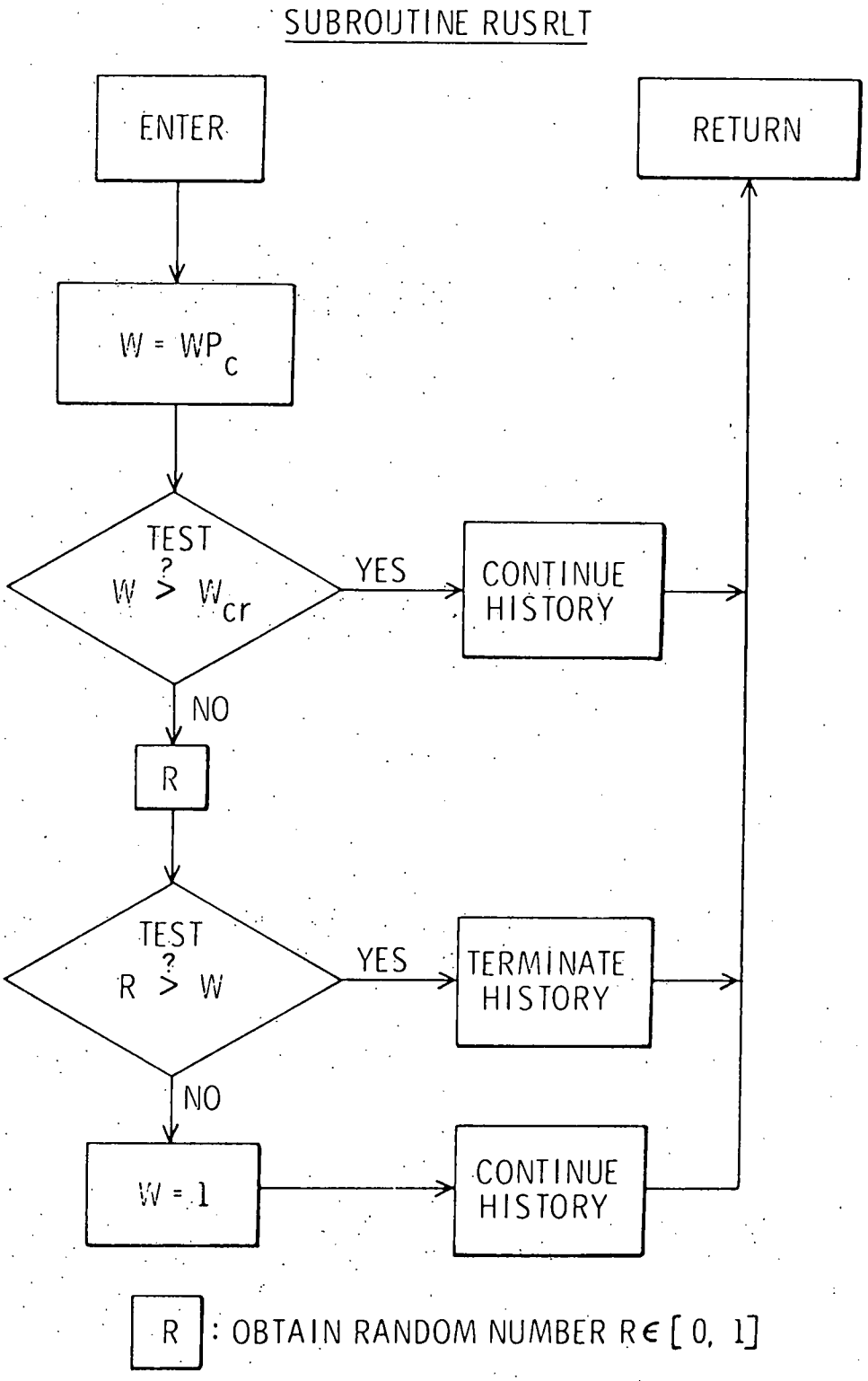

Figure 19. Computational flow diagram for SUBROUTINE RUSRLT of the NUBIN code. RUSRLT performs a Russian Roulette truncation of uninteresting MC test-particle histories. (Ulam, Ref. 111)

E. Rate Coefficient Interpolation.

The cross section averaging code MCSAVG produces tables of the $\langle\sigma v\rangle$ rate coefficients in the form $\langle\sigma v\rangle_i (v_i, \theta_i)$ where the ~ discreet values of test particle speed v_i range from $2.5(10)^7$cm/s to $1.2(10)^9$ cm/s and the ~ 5 discreet values of injection angle θ_i range from 0 to $\pi/2$ radians. These tables are interfaced with the NUBIN MC simulation code as a data base for the particular problem under consideration. For mirror systems the usual assumption of a spatially constant temperature profile allows the rate coefficients to be independent of spatial position as well. The prior calculation of the rate coefficients is an economy measure to circumvent the repeated calculation of the many rate coefficients needed by each of the many test particle histories.

It becomes necessary, however, to interpolate between the discreet values available from the tables to obtain a rate coefficient for specific test particle values of v and θ. The rate coefficient surfaces are smooth (i.e. no resonances) and the tables are sufficiently well resolved (subject to a desire to minimize the data-base computer storage requirement) such that a linear interpolation scheme is at least as accurate as the analytic cross section expressions of Chapt. II. This straightforward approach also is computationally fast.

For a specific (v,θ) pair the two-dimensional grid of table values is searched to bracket the (v,θ) coordinates such that $v_i < v < v_{i+1}$ and $\theta_i < \theta < \theta_{i+1}$. The four-point bivariate interpolation procedure[112] is then applied as illustrated in Fig. 20 for the general function $f(x,y)$. For this application $f(x,y)$ is taken as $\langle\sigma v\rangle(v,\theta)$. The approximate value for $\langle\sigma v\rangle(v,\theta)$ is easily obtained from the nearby tabulated

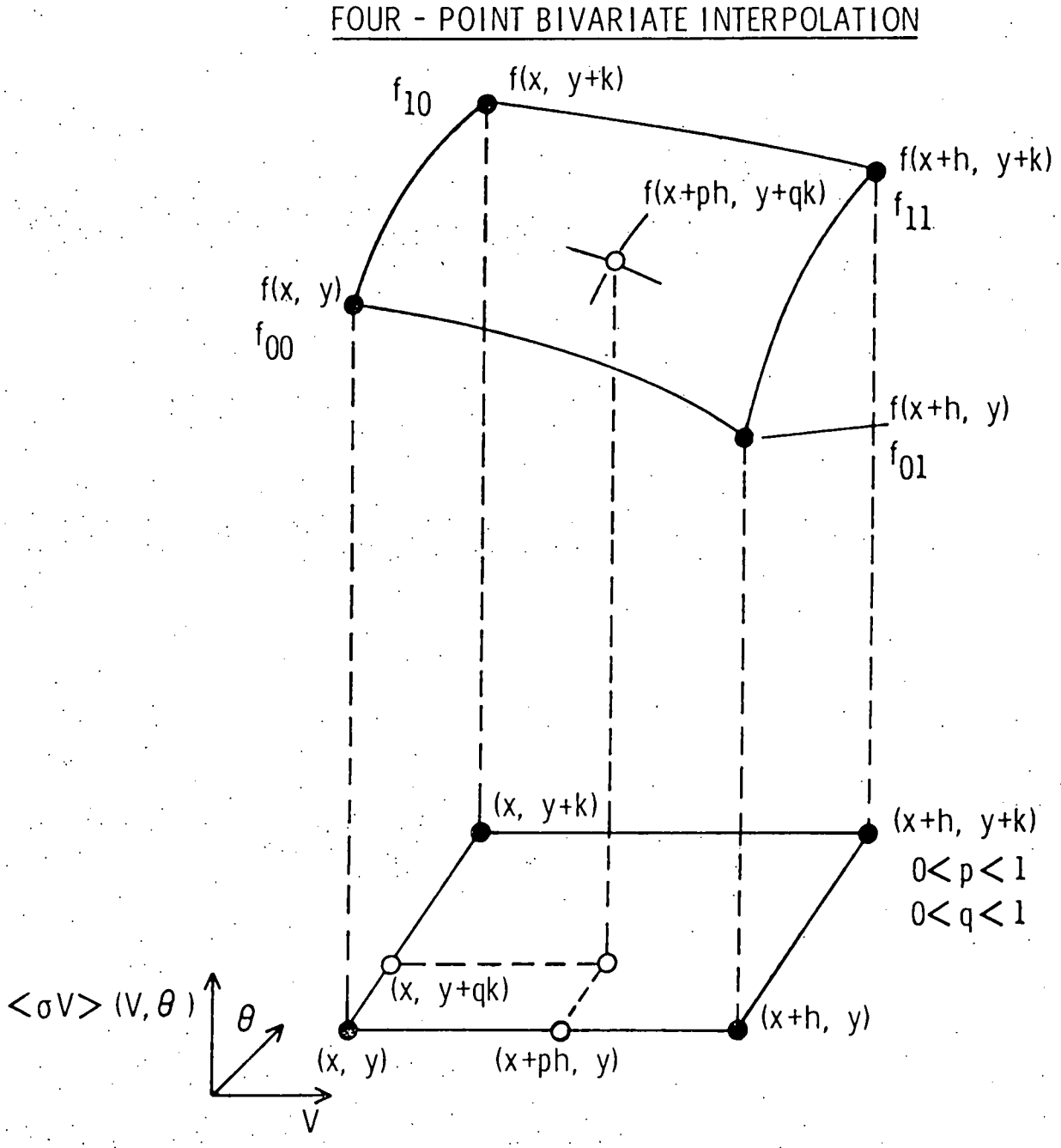

$$f(x+ph,\ y+qk) = (1-p)(1-q)\, f_{00} + p(1-q)\, f_{10} + q(1-p)\, f_{01} + pq\, f_{11} + \mathcal{O}(h^2)$$

Figure 20. Two-dimensional interpolation scheme used to interface the tabular rate coefficient data base of the MCSAVG code with the continuous requirements of the NUBIN simulation code.

values $\langle\sigma v\rangle(v_i,\theta_i)$, $\langle\sigma v\rangle(v_{i+1},\theta_i)$, $\langle\sigma v\rangle(v_i,\theta_{i+1})$, and $\langle\sigma v\rangle(v_{i+1},\theta_{i+1})$. This interpolation procedure is implemented as SUBROUTINE LOOKCS of the NUBIN code.

F. Monte Carlo Code NUBIN.

The Neutral Beam Injection (NUBIN) MC simulation code combines the elements described in the previous sections of this chapter into an overall framework illustrated schematically in Fig. 21. The code begins with the specification of the plasma model as described in the following chapter. The user supplied input parameters are then obtained to specify the particular problem being considered. The total number of neutral particle histories tracked ($\sim 5(10)^4$) is divided into subgroups (cycles) of convenient length ($\sim 5(10)^3$) so that intermediate results can be obtained and convergence tests can be applied. For any particular test particle the simulation loop in the lower part of Fig. 21 is followed until one of two termination conditions is satisfied: a) the test particle crosses the outer plasma boundary whereupon it is extrapolated to the first wall for tabulation of the bombardment or b) the test-particle weight-value falls below a critical threshold and the particle is "killed" in a supplementary Russian Roulette procedure.

At the end of the final particle cycle code results are processed for output and archival storage in the event the particular simulation should be restarted and continued in order to perhaps improve the convergence. An alternative procedure is to optionally readjust plasma conditions in view of the MC results and thus obtain a more self-consistent simulation. This latter option has not been implemented.

MONTE CARLO SIMULATION SCHEME

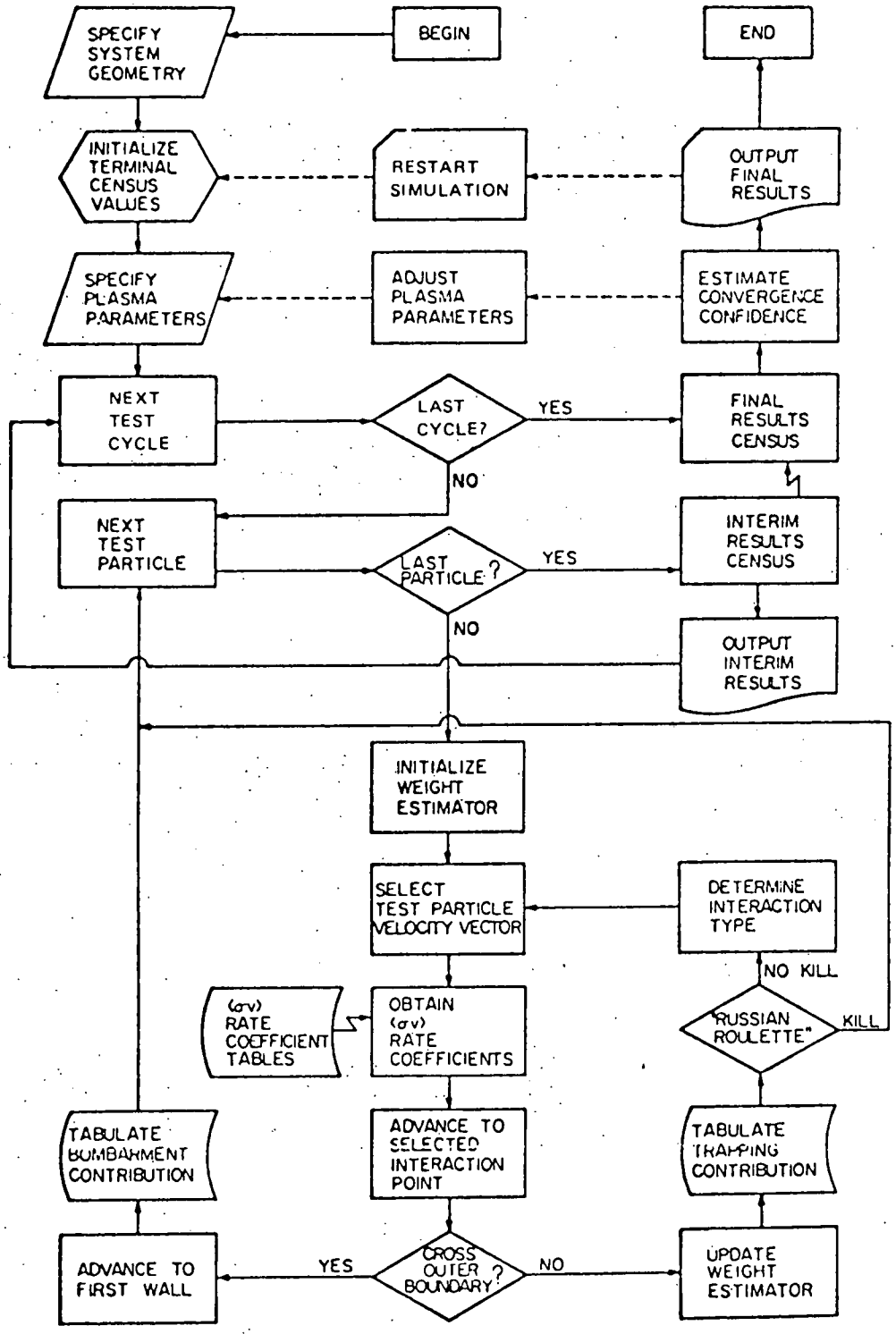

Figure 21. Computation flow diagram for the MC simulation code NUBIN.

Code output consists of tables and graphs describing various key aspects of the beam trapping and first-wall bombardment results. These results for the reference cases considered will be incorporated into the discussions of Chapter V.

Setup of the NUBIN input file and procedures for running the code are discussed in greater detail in the Appendix "Computer-Code User's Guide."

G. Simulation Convergence.

Monte Carlo work must acknowledge and estimate the magnitude of the inevitable statistical uncertainty in its simulation results. For those problems which are amenable to analytical solution, a direct comparison of the analytic and MC results, and hence a direct measure of the convergence of the MC simulation, is possible. However, it is for precisely those problems beyond the reach of analytic methods that MC techniques are attractive. Still, some aspects of a specific MC simulation [e.g., the penetrating fraction f_p of Eqn. (2)] may provide opportunities for straightforward comparisons of the two approaches.

The more standard approach is to inferentially estimate error bounds using traditional statistical methods. Alternately, but in the same spirit, a maximum tolerable error criterion is established and the MC simulation is continued until that criterion is met with a sufficiently high confidence level that the results seem meaningful and are reproducible. The latter approach is used in NUBIN.

Following the discussion of E. Cashwell and C. Everett[85] a general, but indirect measure of the convergence of the MC procedure is employed. The MC calculation <u>without weights</u> gives a number M out of N source

particles which terminate in each of a set of all-inclusive, mutually distinct terminal categories C. There is a probability p (unknown a priori) that any particular history will terminate in a particular category C. The object of the simulation is the determination of p. The ratio M/N is tentatively taken as an estimate for p at a late stage of the simulation when this ratio appears to have stabilized and a quantity $q \equiv (1-M/N)$ is defined. A measure of the probability P that the estimate is within a specified tolerance, ε, of the actual probability, p, is given by

$$P\,[|(M/N)-p|<\varepsilon] \approx \mathrm{erf}\,(t/\sqrt{2}) + R \qquad (55)$$

where $\mathrm{erf}(x) = \frac{2}{\sqrt{\pi}} \int_0^x e^{-x^2}\,dx$, the error function and

$t = \varepsilon \sqrt{N/(M/N)/(1-M/N)}$ and R is a small additional error term vanishing as $N \to \infty$. The desirable result is a value of P approaching unity for a choice of small ε without requiring an excessive number of test particle histories N. As the simulation converges, the measure P approaches unity asymptotically.

For the problem with weights the mathematical basis is less firm.[85] A useful error measure can nonetheless be calculated if Eqn. (55) is modified such that N represents the total weight estimator used in the simulation and M represents the accumulated weight tabulated for the particular outcome. One such particular outcome might be trapping by electron-impact ionization in the context of this study. Thus, a MC estimate of f_{ei} in Table I will have an associated value of P_{ei} representing the confidence that f_{ei} is known to within $|\varepsilon|$.

IV. APPLICATION TO MIRROR FUSION SYSTEMS

A. Target-Plasma Model.

1. Relevant Mirror-System Physics.

This section will summarize certain aspects of mirror-system physics which will be used together with the results of the NUBIN simulation to assess the influence of incomplete neutral-beam trapping on device performance.

The steady-state thermonuclear power P_F per unit volume V of D-T plasma is given by

$$P_F/V = \frac{1}{4} n^2 \langle\sigma v\rangle_F E_F \tag{56}$$

where n is the plasma density ($n_e = n_i = n$), $\langle\sigma v\rangle_F$ is the fusion reactivity obtained in a manner analogous to the approach of Chapter II for other interactions, and E_F is the energy released (17.58 MeV) per fusion reaction. The total power, assuming $\langle\sigma v\rangle_F$ is spatially constant as is the case under the assumption of a spatially constant temperature profile, is

$$P_F = \frac{1}{4} \langle\sigma v\rangle_F E_F \int n^2 \, dV \quad . \tag{57}$$

To maintain the plasma in a steady state the particle loss rate due to Coulomb scattering into the loss-cone regions of phase space must be balanced by particle injection. If the mean lifetime of particles is time τ, the required injection current is[6]

$$J_I = \int \frac{n}{\tau} \, dV \quad . \tag{58}$$

Eqn. (58) is usually recast as a function of the space-independent scaling product $n\tau$ in the form

$$J_I = \frac{1}{n\tau} \int n^2 \, dV \quad . \tag{59}$$

The $n\tau$ scaling product for the energy distributions given by Eqns. (18-19) is taken[77] to be

$$n\tau = 2.1(10)^{10}\,\tilde{E}_p^{\,3/2}\,\log_{10} R' \qquad (60)$$

where $\tilde{E}_p$ is the characteristic energy of the mirror-confined ions and R' is the effective mirror ratio defined in Eqn. (15).

The fusion power amplifies the injected neutral-beam power $P_I = J_I E_I$ by the ratio

$$Q = \frac{P_F}{P_I} = \frac{\langle\sigma v\rangle_F\, E_F\, n\tau}{4E_I} \qquad (61)$$

which is monitored as a power (energy) multiplication "figure-of-merit" for mirror performance. For incomplete neutral-beam trapping such that the actual injector output is $J_I' = J_I/f_t$ the Q-value is reduced such that $Q' = Qf_t$. Since standard mirror performance yields Q-values only marginally in excess of unity even under the best circumstances, it is important to maximize f_t.

For an injector power $P_I' = J_I' E_I$ the total power lost P_L due to charge-transfer-produced neutral-atom bombardment of the first wall and the penetrating fraction of the neutral beam is just

$$P_L = P_I' \left[\sum_{i=1}^{3} (f_{pi} + f_{wi} \langle E\rangle_i / E_{Ii}) \right] \qquad (62)$$

where the summation over the i subscript represents the contribution of the E_o primary (i=1), $E_o/2$ secondary (i=2), and $E_o/3$ tertiary (i=3) neutral beam energy components. Other parasitic beam fractions are small enough (<3%) to be negligible.[23] E_{Ii} is the energy of the i^{th} beam fraction, $\langle E\rangle_i$ is the average energy of neutrals escaping to the wall for the i^{th} beam fraction and the terminal fractions f_{pi} and f_{wi} are respectively the penetrating and wall bombardment terminal fractions for the i^{th} beam fraction (see Fig. 1). For the parasitic beam

fractions the ratio $\langle E \rangle_i / E_{Ii}$ may well exceed unity. Thus under operating conditions where these beam fractions dominated, the ratio P_L/P_I' could also exceed unity, thus representing a net power loss.[23]

The assumed energy distribution functions [Eqns. (18)-(19)] are separately obtained[6,77] by one- and two-dimensional Fokker-Planck computations for $E_o \sim \tilde{E}_p$ and give classical values of $n\tau$ consistent with Eqn. (60). Rate coefficients from Chapter II are calculated self-consistently.

2. Plasma Density Profiles.

The so-called "Yin-Yang" minimum |B| coil configuration is invoked for mirror systems in order to provide MHD stability with reasonable mirror ratios.[6] The plasma is centrally confined by the magnetic well produced by such a coil configuration as indicated in Fig. 22. Plasma leaks out along magnetic field lines through the two mirror-coil throats to give the apparent shape of the plasma "surface" as a double-fan. An approximate representation of this shape has been developed in concert with LLL researchers.[113,114]

The plasma is oriented along the z-axis such that the "fans" lie in the yz (for $z > 0$) and xz (for $z < 0$) planes. In any plane perpendicular to the z-axis (with $|z| < L/2$ where $L/2$ is the axial plasma half-length), the plasma envelope is taken to be an ellipse. The variable semimajor/ minor axes of the ellipse are represented approximately by parabolic functions of z so that $P(x_o, y_o)$ lies on the plasma surface and satisfies the standard equation

$$\left(\frac{x_o}{C_x(z)}\right)^2 + \left(\frac{y_o}{C_y(z)}\right)^2 = 1 \quad . \tag{63}$$

Note that at the plasma midplane ($z = 0$), $C_x(0) = C_y(0)$ and the ellipse

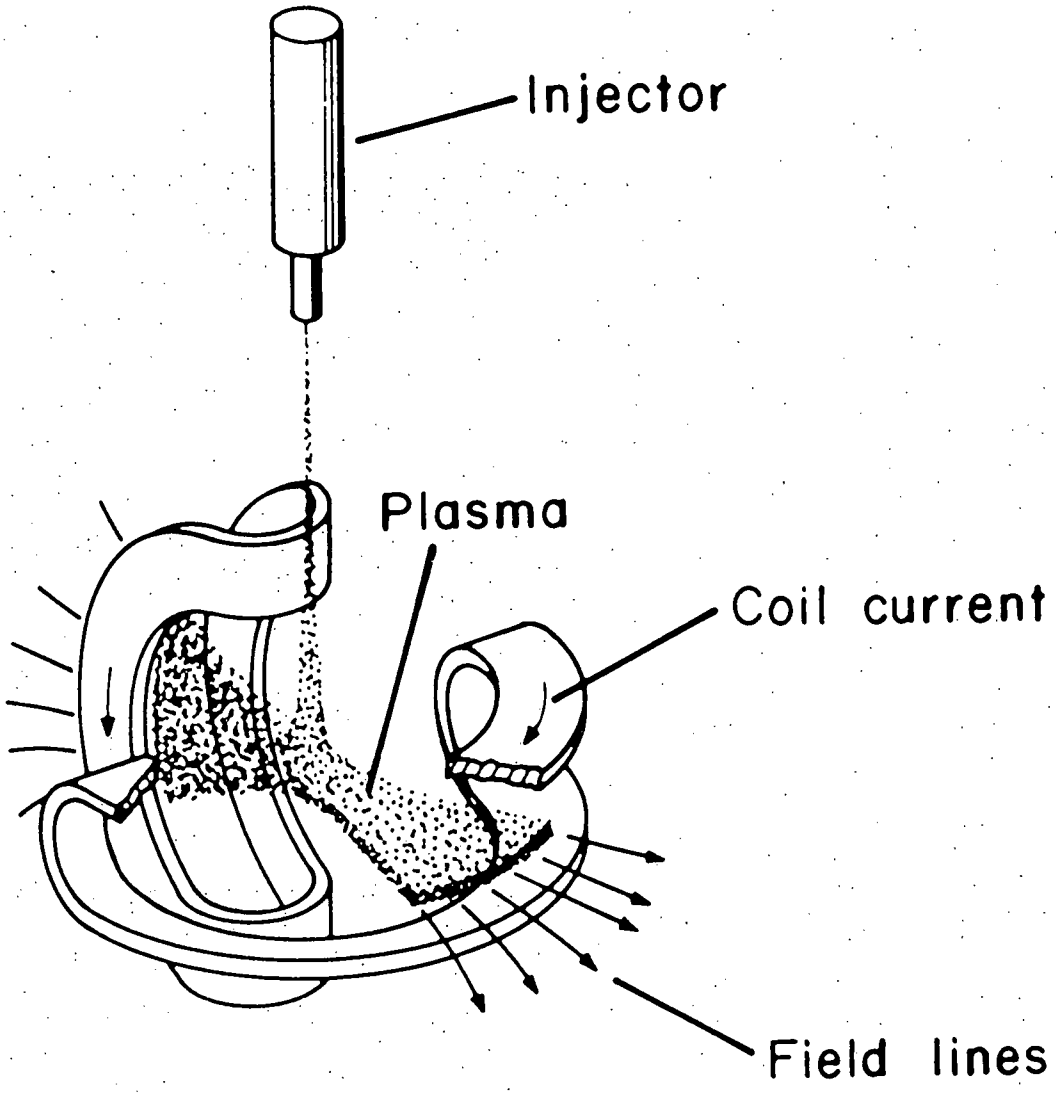

Figure 22. Plasma confinement in a minimum-|B| magnetic well produced by a Yin-Yang coil configuration. Plasma leakage along field lines is balanced by neutral-beam injection.

reduces to a circle of radius R_p. The curves $C_x(z)$ and $C_y(z)$ are uniquely defined using five parameters: The midplane radius R_p, the plasma half-length L/2, a point P(0,0,a) and an angle ϕ_m with respect to the z-axis giving the fan divergence, and the half-thickness of the plasma at the mirror throat ($z = \pm L/2$).

By invoking approximate magnetic flux conservation in any plane perpendicular to the z-axis, the normalized magnetic field strength is a function of z such that

$$\frac{B(z)}{B_0} = R' \frac{B(z)}{B_m} \left(\frac{R_p^2}{C_x(z)\, C_y(z)} \right) \tag{64}$$

where R' is again the effective mirror ratio.

Within this plasma boundary, the plasma density is assumed to be separable into radial and axial components such that

$$\frac{n(x,y,z)}{n_o} = \frac{n(r)\, n(z)}{n_o} \tag{65}$$

where n_o is the central plasma density, [i.e. $n_o = n(0,0,0)$]. In any plane perpendicular to the z-axis, the density varies as

$$\frac{n(r)}{n_o} = \left[1 - \chi \left(\frac{r}{\rho} \right)^j \right] \tag{66}$$

where $0 < \chi < 1$ and $j = 1, 2, 3, \ldots$ are fitting parameters and $r^2 = x^2 + y^2$. Figure 23 illustrates this behavior. Recalling Eqn. (63),

$$\rho^2 = x_o^2 + y_o^2 \ , \tag{67}$$

such that azimuthally about the z-axis

$$\frac{x}{y} = \frac{x_o}{y_o} = \tan \phi \ . \tag{68}$$

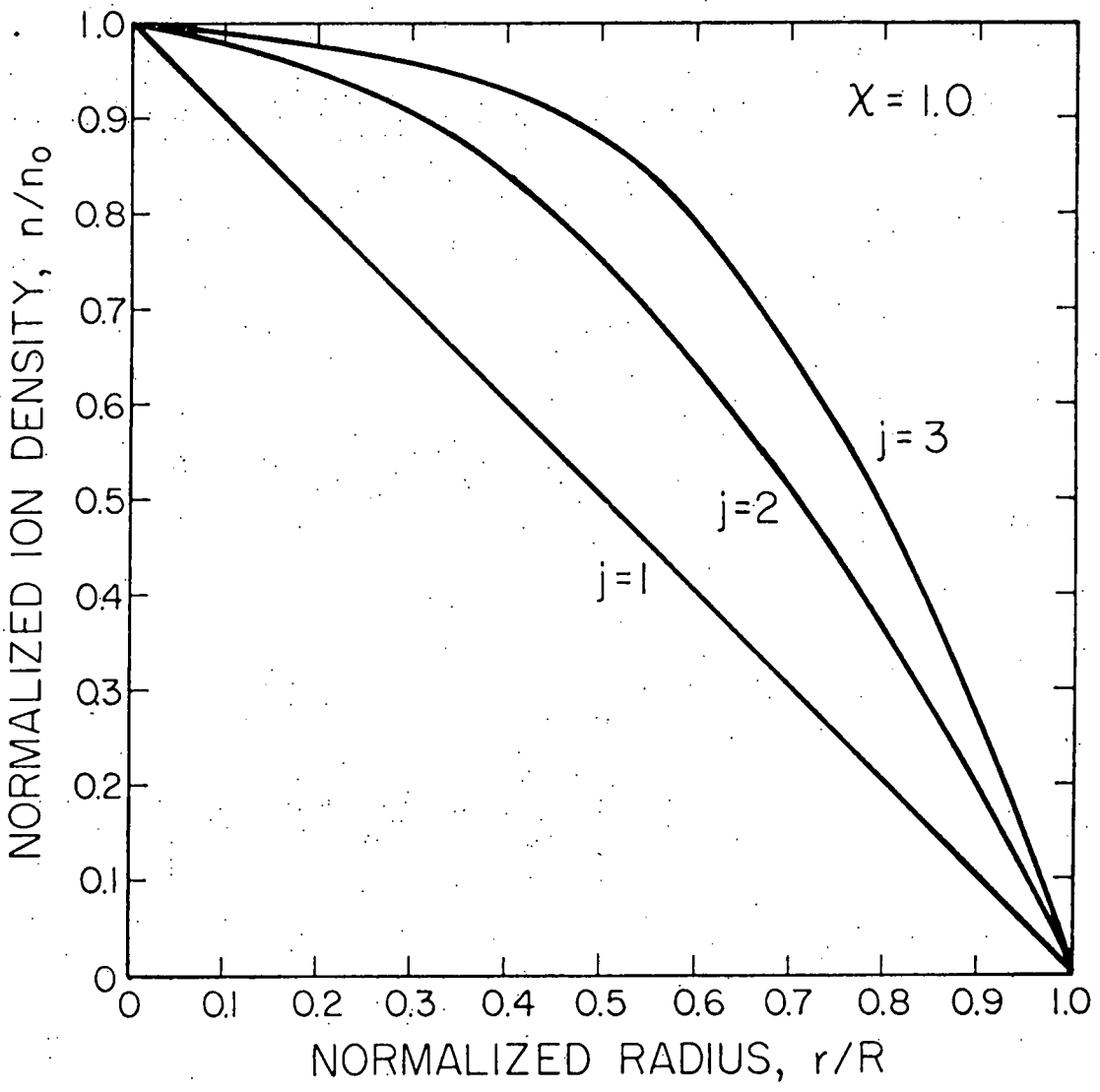

Figure 23. Representative radial plasma density profiles of the form $n(r) = n_o [1-\chi(r/R)^j]$.

Along the z-axis, the normalized plasma density profile is approximately using the expression of L. Hall:[115]

$$\frac{n(z)}{n_o} = f\left(\frac{B(z)}{B_m}\right) = \kappa \left\{(2R' - 3)\left[\tanh^{-1}\left(1 - \frac{B(z)}{B_m}\right)^{1/2} - \left(1 - \frac{B(z)}{B_m}\right)^{1/2}\right] + \frac{(1 - B(z)/B_m)^{3/2}}{3\, B(z)/B_m}\right\} \quad (69)$$

where κ is a normalization constant such that $f(1/R') = 1$. This profile is plotted in Fig. 24 for the FERF.[6]

The plasma volume integrals in Eqns. (57) and (59) are evaluated in the general form[6,10]

$$\int n^i \, dV = \int_o^{R_p} n^i(r)\, 2\pi r dr \int_{-L/2}^{+L/2} \frac{B_m}{B} \, f^i\left(\frac{B}{B_m}\right) ds' \quad (70)$$

such that

$$\int n^i \, dV = \pi R_p^2 \, L \, n_o^i \, G^i(R') \quad (71)$$

where the auxiliary function $G^i(R')$ includes the radial profile term

$$A^{i,j} = 2 \int_o^{R_p} \left[1 - \chi\left(\frac{r}{R_p}\right)^j\right]^i \frac{r}{R_p} \frac{dr}{R_p} \quad (72)$$

and the axial contribution

$$C^i(R') = \int_o^1 \frac{B}{B_m} f^i\left(\frac{B}{B_m}\right) ds \quad (73)$$

so that

$$G(R') = \pi R_p^2 \, L \, n_o^i \, A^{i,j} \, C^i(R') \quad . \quad (74)$$

The quantities $C^i(R')$ are graphed as a function of mirror ratio R' in Fig. 25 for reference purposes.

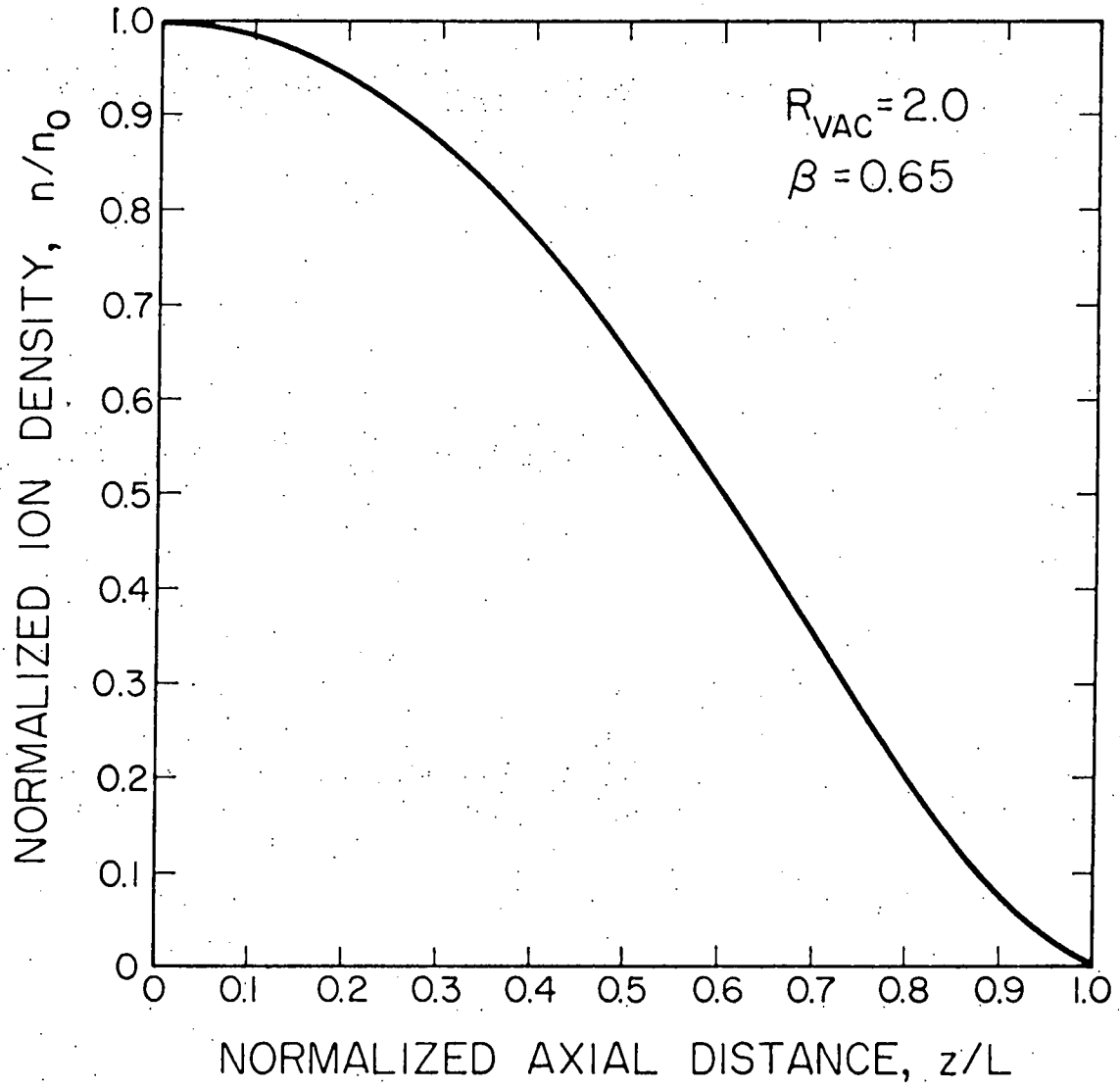

Figure 24. Typical axial plasma density profile for a mirror system.

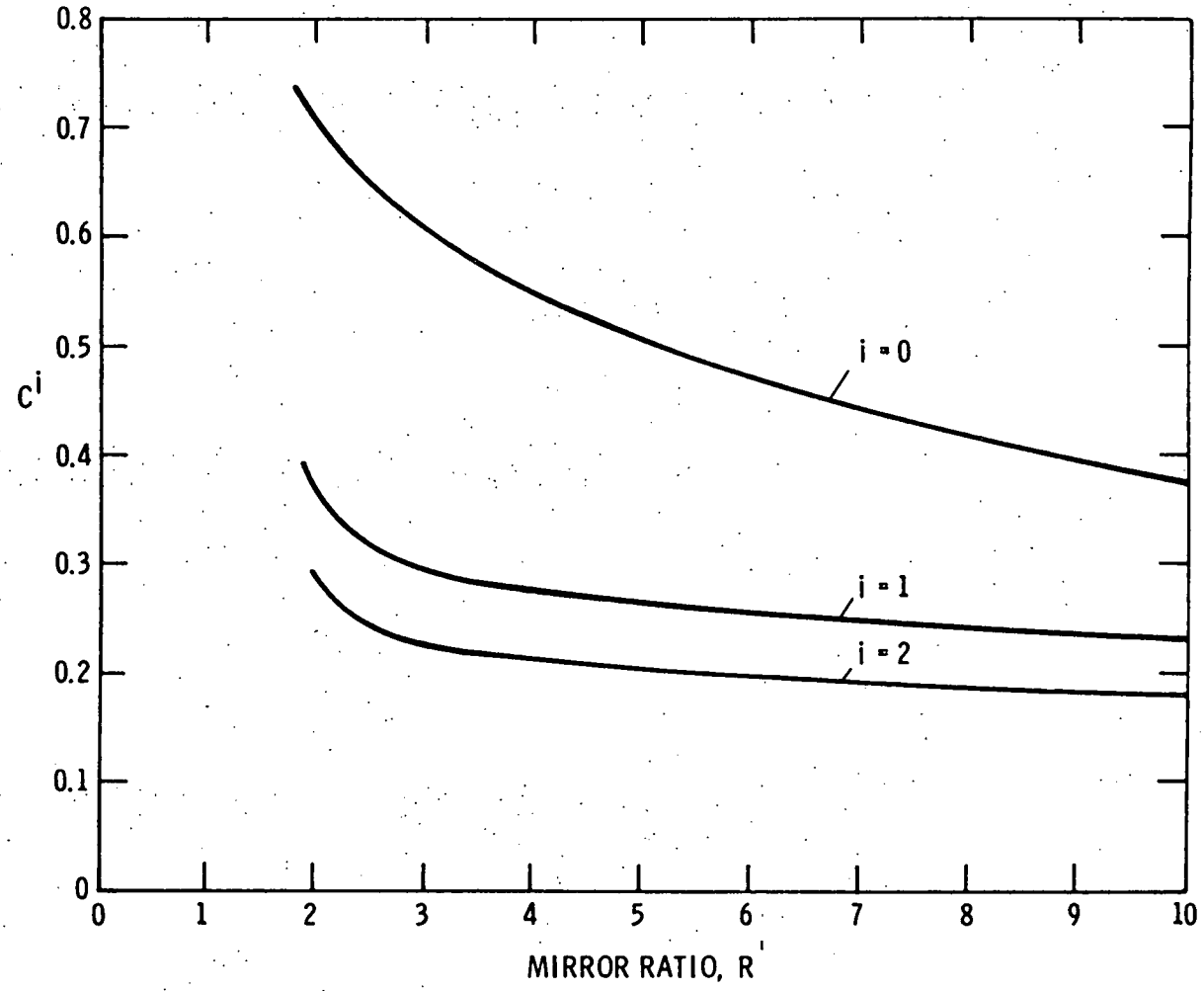

Figure 25. Auxiliary function $C^i(R')$ as a function of mirror ratio R'.

B. Auxiliary Models.

1. Neutral-Beam Source.

As currently implemented in the NUBIN code, the neutral beam originates as a point source of test particles located at some arbitrary point, $P(x_o,y_o,z_o)$, outside the plasma target (Fig. 14). This is, in effect, consistent with the mirror designs, which involve the focusing of the beam from several sources through a small aperture in the plasma chamber wall,[6] as can be seen in Fig. 26. The injection orientation $\vec{I}(\theta,\phi)$ is selected to intercept the plasma target and can be varied so as to parametrically study the effects of different attenuation chord lengths and different injection angles with respect to the magnetic axis, $\vec{B}(\theta,\phi)$. The beam is taken to be a right circular cone of half-angle width, α, such that three alternate beam profiles may be specified, namely:

1. Pencil beam (α = 0 radians)
2. Uniform transverse intensity (α > 0 radians)
3. Gaussian transverse intensity ($0 \leq \beta \leq \alpha$ radians)

In profile 3, β' represents the angle at which the neutral-beam intensity has fallen by a factor of $1/e$ of its centerline value.

The beam is currently taken to be mono-energetic, but the MC procedure, of course, can accommodate an energy-distributed source. The effects of the parasitic neutral beam components at half and third energies are calculated separately and can later be aggregated into an overall result using the MCS_D code (see Appendix).

2. First-Wall Detector Grid.

In order to tabulate the bombardment of the first-wall surface, a hypothetical shell (optionally a sphere or a right-circular cylinder)

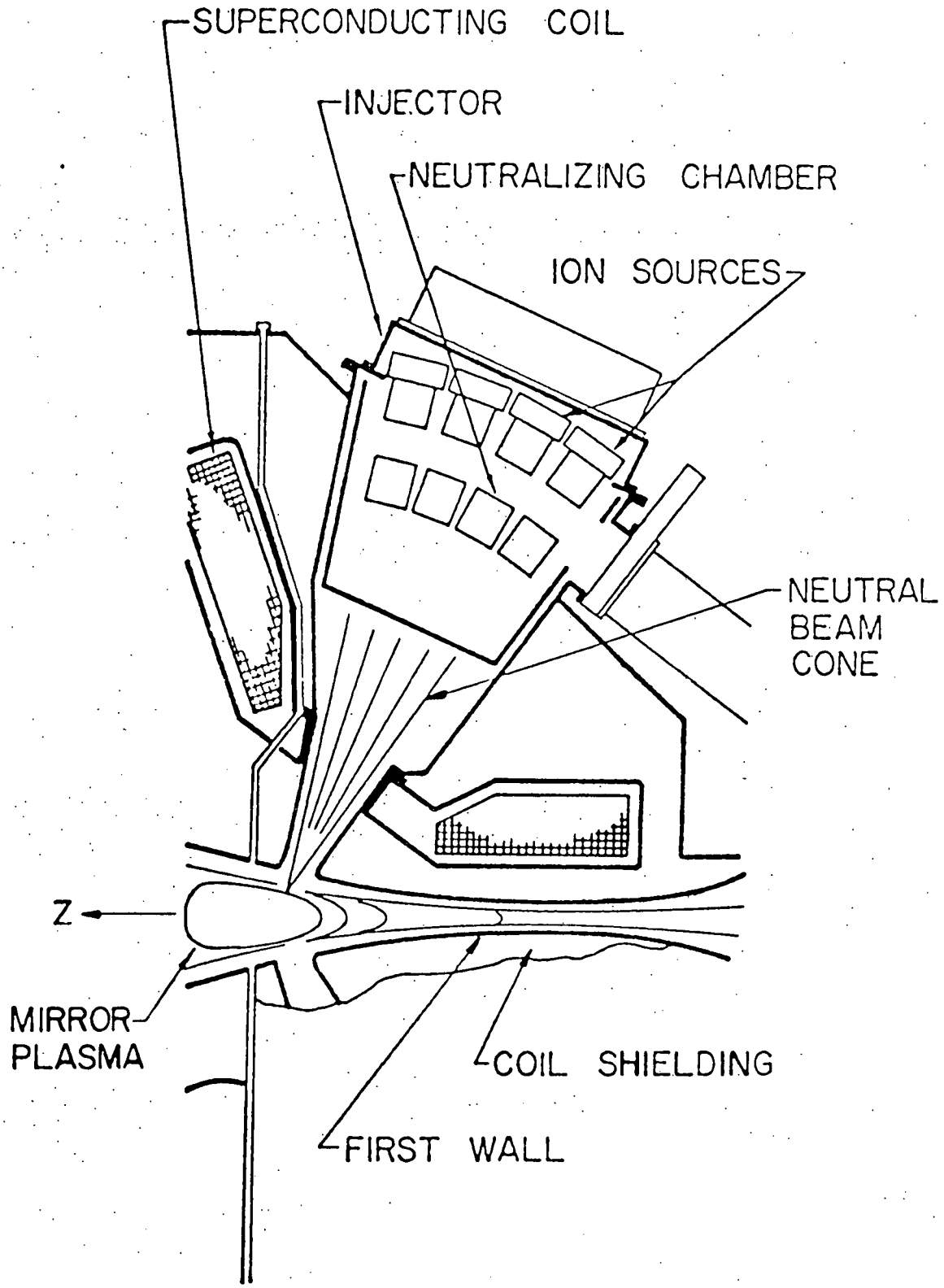

Figure 26. Neutral-beam injection configuration for the FERF design. The several individual injection modules are oriented to inject through a common port in the first wall.

is constructed to enclose the outer plasma boundary. This is illustrated in Fig. 27 for the cylindrical wall used in the FERF study. The actual first wall of a mirror machine may follow the plasma shape more closely (see Fig. 26), but is less convenient for tabulation and visualization of the first wall bombardment results. In any case, the results from the idealized wall can be mapped onto an alternative surface. The surface area of the first wall is partitioned into an array of equal-area "detector" subregions. As neutral test particles impact a given subregion, an accumulation of the residual test particle weight-values is made which is finally tabulated as a census of the nonuniformly distributed first-wall particle bombardment. The resolution of this bombardment improves as more (smaller) detector regions are used, but it becomes more difficult to obtain stable MC solutions for a fixed number of test particles if the probability of impacting in a given detector region (which decreases directly with its area) is too low. Statistical fluctuations between adjacent detectors become large. Typically, a 64 x 32 grid or 2048 individual detectors are used for the FERF case using R_w=80 cm, each detector area is approximately 10 cm^2.

In addition, an overall bombardment energy distribution function is constructed. Tabulation of a separate distribution for each subregion is prohibitive although it should be recognized that the angular and energy distributions are coupled, if only weakly. Assigning a global energy distribution also allows the angular particle-bombardment distribution to at the same time represent the power-deposition distribution for purposes of Chapter VI.

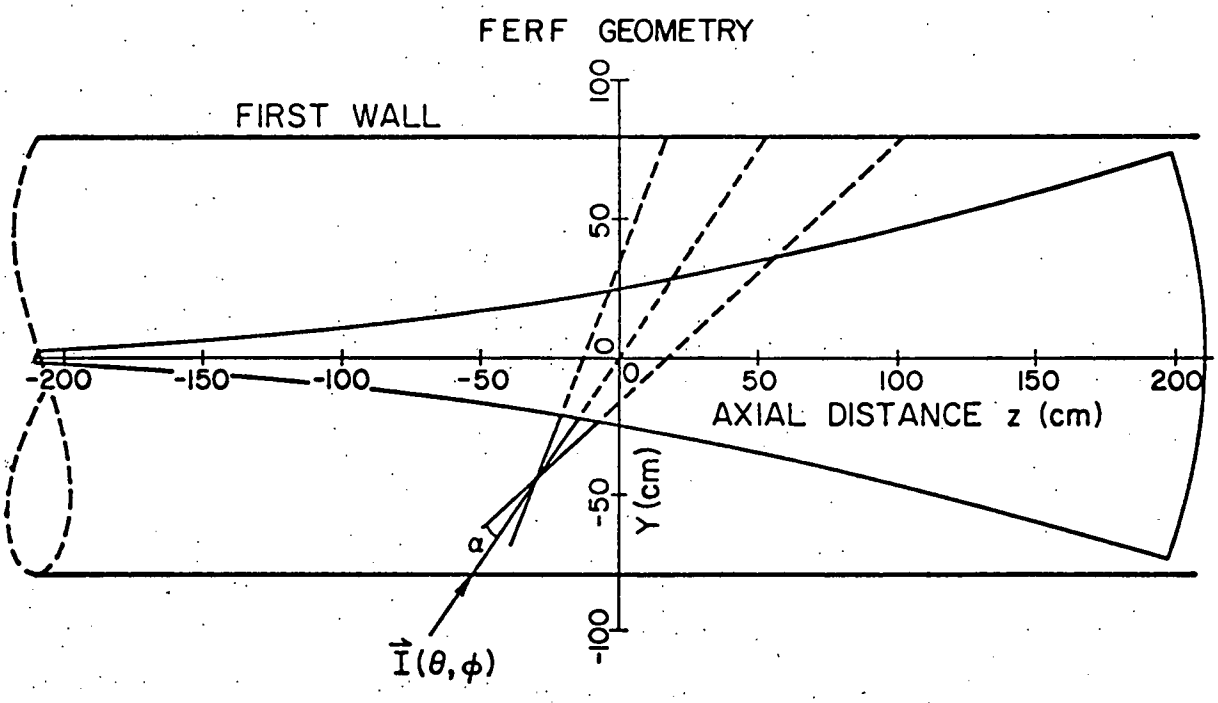

Figure 27. Idealization of the typical neutral-beam injector, plasma, and first-wall configuration used in the MC simulation code NUBIN.

V. MONTE CARLO SIMULATION RESULTS

A. Benchmark Calculations.

1. Spherical Geometry.

An early version of the MC simulation code (NUBIN3) was used to study spherical plasma targets in order to provide benchmark comparisons with the analytic and numerical models considered in Chapter I. This effort also served as an opportunity to develop and optimize the MC algorithms. The system parameters and results for this computation are summarized in Table II. In this case the density is taken to be spatially uniform [n(r) = constant].

The NUBIN3 calculation is in general agreement with the LLL one-generation model[22,113] for this particular case. The minor discrepancies can be ascribed to a) incomplete MC convergence, b) slight differences in the rate coefficients, and c) the influence of the $n \geq 2$ generations of charge-transfer neutrals. Item c) is most significant for the estimate of the power loss ratio P_L/P' for the $E_0/3$ beam component. Comparison of the power loss ratio results with those obtained from Ref. 116 is made for the most comparable case graphed.

The contribution of later-generation, charge-transfer-produced neutrals to the global results of Table II is indicated in Table III. For the particular test case the influence of $n \geq 2$ generation neutrals is quite small. A few neutrals are tracked through as many as seven generations before escape, however. The value of f_w for the 0^{th} generation corresponds to f_p.

The composite, normalized energy distribution functions of the neutrals bombarding the first wall are illustrated in Fig. 29 for the

TABLE II

MIRROR FERF PARAMETERS USED FOR SPHERICAL BENCHMARK CALCULATIONS*

Coordinates of plasma center, P(a,b,c)	(0,0,0)	cm
Plasma radius, R_p	25.0	cm
Cylindrical first-wall radius, R_w	35.0	cm
Average plasma number density, $\bar{n}$	$2.25(10)^{14}$	ions/cm^3
Central plasma number density, n_o	$2.25(10)^{14}$	ions/cm^3
Plasma density profile parameters, χ	0.0	
j	3.0	
Characteristic plasma ion (D^+) energy, $\tilde{E}_p$	70.0	keV
Characteristic plasma electron energy, E_e	7.2	keV
Magnetic axis orientations, $\vec{B}(\theta,\phi)$	(0,0)	radians
Effective mirror ratio, R'	3.38	
Coordinates of neutral beam point source, $P(x_o,y_o,z_o)$	(-50,0,0)	cm
Injection orientation, $\vec{I}(\theta,\phi)$	(π/2,0)	radians
Angular divergence of neutral beam, α	0.002	radians
Gaussian neutral beam parameter, β	0.001	radians
Neutral beam component energies, E_o	65.0	keV
$E_o/2$	32.5	keV
$E_o/3$	21.7	keV
$\gamma_o = \gamma(E_o)$ [from Eqn. (2)]	4.54	
$n\tau_{ion}$	$6.44(10)^{12}$	cm^{-3}sec

(continued on next page)

*Convergence: P > 0.90 for $\varepsilon = \pm$ 0.005

Table II (continued)

Results:

Beam component:	E_o	$E_o/2$	$E_o/3$
Fractional current:	~0.51	~0.22	~0.24
Number of test particles:	$1.75(10)^4$	$2(10)^4$	$3(10)^4$
f_p	0.008	0.001	<0.001
f_w	0.100	0.143	0.206
f_t	0.892	0.856	0.794
<E> of f_w	60.5	58.6	58.4
$P_L/P'[\gamma_o = 4.54]$	0.103	0.249	0.543
P_L/P' [γ = 5 from Ref. 116]	0.10	0.23	0.41

TABLE III

TERMINAL PARTICLE FRACTIONS BY GENERATION (SPHERE)

GENERATION #	E_o		$E_o/2$		$E_o/3$	
	f_t	f_w	f_t	f_w	f_t	f_w
0	0.537	0.008	0.478	0.001	0.452	<0.001
1	0.218	0.040	0.226	0.072	0.209	0.130
2	0.088	0.028	0.096	0.035	0.085	0.043
3	0.034	0.016	0.037	0.018	0.033	0.017
4	0.012	0.007	0.014	0.008	0.012	0.007
5	0.004	0.003	0.005	0.003	0.004	0.003
6	0.002	0.001	0.002	0.001	0.002	0.001
7	0.001	~0.0	0.001	~0.0	0.001	~0.0
8	~0.0	~0.0	~0.0	~0.0	~0.0	~0.0

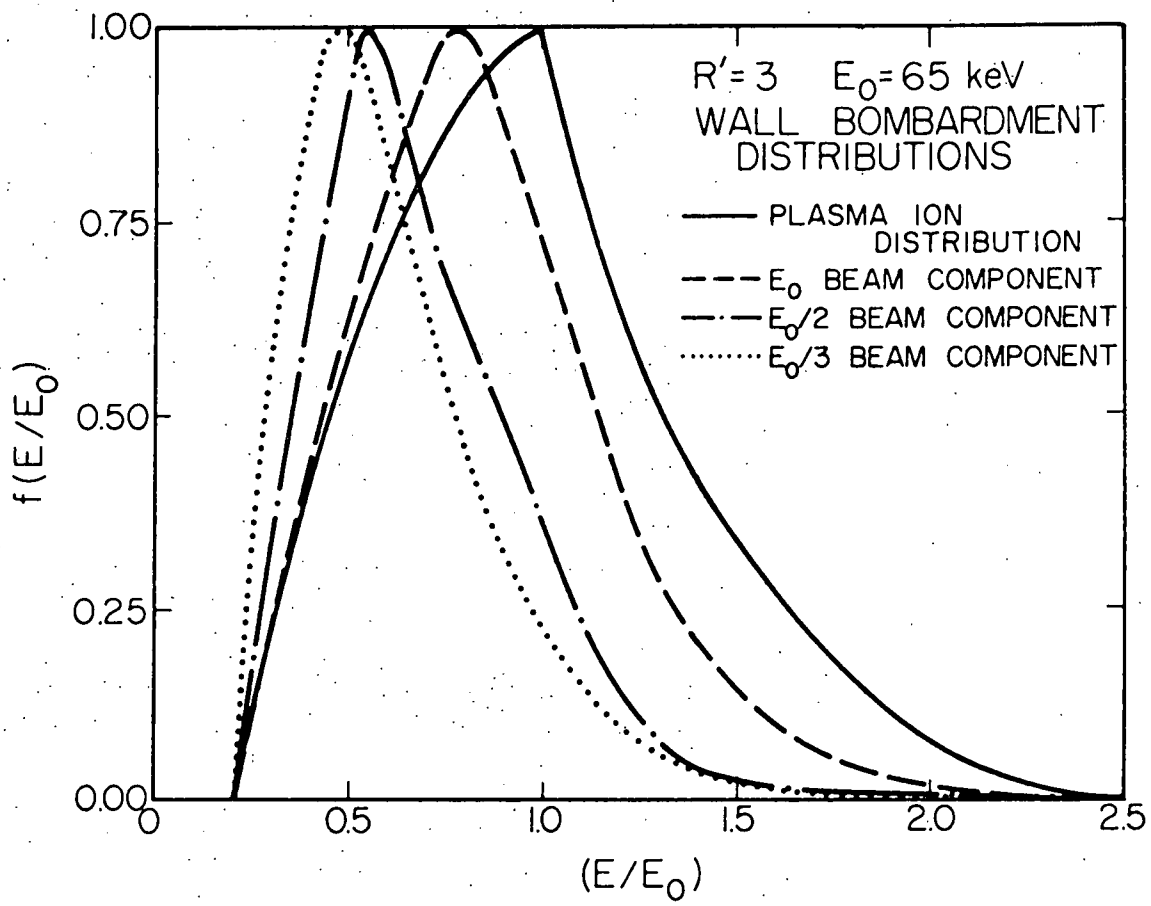

Figure 28. Normalized energy distributions for the charge-transfer-produced neutral particles escaping to bombard a FERF first wall for the NUBIN3 benchmark calculation in spherical geometry.

spherical benchmark case of Table II. The results indicate a fairly good correlation between the energy of the beam component and the peak of the neutral-particle distribution associated with it. The high-energy tail of the ion energy distribution is essentially uninvolved in the charge-transfer process because of the drop in the charge-transfer cross section for large relative collision velocities.

2. Cylindrical Geometry.

If the axial plasma density profile of a mirror-confined plasma is taken to be constant, the system may be treated as though it were an infinite cylinder of plasma. This provides a useful test case for the MC method. For such a system two series of calculations were made for a FERF-like system in general similar to that of Table II. In the first series the plasma density was taken to be spatially uniform (χ=0) and the injection angle θ_i was set equal to $\pi/2$ radians to represent injection perpendicular to the magnetic axis. In the second series the plasma was given a cubic radial density profile (χ=1, j=3) and the injection angle was set to 0.98 radians as for the FERF reference case considered in the following section. The central plasma density was varied for both series of runs. Results for the neutral-beam terminal fractions are reported in Table IV and where possible compared to direct numerical attenuation calculations or to the analogous analytical spherical system results, although no precise agreement in the latter comparison was sought or anticipated. For CASE 1, the MC penetration fraction (f_p) results are in good agreement with the expected results as obtained from transmission calculations using Eqn. (2). Surprisingly good, although fortuitous, agreement is also noted for the analogous

TABLE IV

MIRROR-FERF CYLINDRICAL BENCHMARK CALCULATIONS[a]

CASE 1. (χ = 0.0, $\theta_i = \pi/2$)

n_{io}(ions/cm^3)	f_p	γ_o	f_w	P_w[b]	f_t	P_t[b]
10^{13}	0.810		0.081	(0.94)	0.109	(0.98)
	0.808[c]	0.213	0.082[d]		0.110[d]	
$5(10)^{13}$	0.341		0.210	(0.78)	0.449	(0.79)
	0.344[c]	1.067	0.215[d]		0.441[d]	
			~0.20[e]		~0.46[e]	
10^{14}	0.117		0.197	(0.80)	0.686	(0.78)
	0.119[c]	2.129	0.196[d]		0.685	
			~0.19[e]		~0.69[e]	

CASE 2. (χ = 1.0, j = 3, θ_i = 0.98)

10^{13}	0.829	0.068	(0.96)	0.104	(0.98)
$5(10)^{13}$	0.388	0.194	(0.78)	0.418	(0.79)
10^{14}	0.151	0.206	(0.79)	0.643	(0.77)
$5(10)^{14}$	~0.0	0.099	(0.96)	0.901	(0.84)

---

[a] Parameters largely consistent with Table II.

[b] Confidence probability for error $|\varepsilon| < 0.002$, $N = 10^5$ test particles.

[c] Eqn. 2 transmission calculation using estimated rate coefficients.

[d] Eqns. (6-7) ∞-generation results for spherical target.

[e] Ref. 22 1-generation results for spherical target.

spherical f_w and f_t results. Here, since the neutral particle mean-free paths are of the order of the target size, the shape of the target is unimportant. For the f_w and f_t results, the corresponding convergence confidence values of P are also given. The trapping and wall bombardment terminal fractions by charge-transfer generation number are summarized in Table V. As expected, the influence of later generations increases as the density of the target increases, thus increasing the number of mean-free paths available for a fixed radius. As for Table III, f_w for the 0^{th}-generation corresponds to f_p.

B. Reference Case Studies.

1. Overview.

The Mirror Fusion Test Facility (MFTF)[3] and the Fusion Engineering Research Facility (FERF)[6] are well-suited for MC neutral-beam simulation using the NUBIN code. The proposed design points for both devices incorporate characteristic energies (50-100 keV) and target plasma radii (20-70 cm) that the analytic models discussed in Chapter I suggest will make the influence of charge-transfer-produced neutrals important. The specific features of the design points of the two machines relevant to this study are summarized in Table VI. For present purposes a deuterium beam is taken to be injected into a deuterium plasma. The equivalent D-T system, for which energy-multiplication Q-values will be calculated, would involve simultaneous injection of tritium at equal speed. Since the collision cross sections of interest depend only on the collision speed and not on isotopic identity, this bookkeeping simplification is justified. The results of the FERF calculations will be presented in greater detail in this chapter and will serve as the basis for the discussion of engineering implications in the next chapter.

TABLE V

TERMINAL PARTICLE FRACTIONS BY GENERATION (CYLINDER)

CASE 2. (χ = 1.0, j = 3, θ_i = 0.98)*

n_{io}(ions/cm^3)	10^{13}		$5(10)^{13}$		10^{14}		$5(10)^{14}$	
GENERATION #	f_t	f_w	f_t	f_w	f_t	f_w	f_t	f_w
0	0.100	0.829	0.358	0.388	0.496	0.151	0.585	~0.0
1	0.003	0.065	0.050	0.159	0.110	0.146	0.188	0.064
2	~0.0	0.003	0.008	0.030	0.028	0.045	0.075	0.023
3	~0.0	~0.0	0.001	0.005	0.007	0.012	0.031	0.009
4			~0.0	0.001	0.002	0.003	0.013	0.003
5			~0.0	~0.0	~0.0	0.001	0.005	0.001
6					~0.0	~0.0	0.002	0.001
7							0.001	~0.0
8							~0.0	~0.0
9								
10								

*See Table IV.

TABLE VI

REFERENCE MIRROR DEVICE PARAMETERS*

Parameter	MFTF	FERF
Plasma length, L(m)	3.4	4.2
Plasma radius, R_p(m)	0.6	0.25
Magnetic field, B_o(T)	2.0	3.75
Mirror ratio, R_{vac}	2.0	2.0
Effective mirror ratio, R'	2.83	3.38
Plasma energy, $\tilde{E}_p$ (keV)	50	70
Injection energy, E_o (keV)	75	65
Central density, n_o (ions/m^3)	$1(10)^{20}$	$3(10)^{20}$
Plasma beta, β	0.5	0.65
Electron energy, $\tilde{E}_e$ (keV)	5	7
Injection "point source," $P_o(x_o,y_o,z_o)$	(-300.0, -300.0, 0.0)	(-0.45, 0.0, -0.30)
Injection orientation, $\vec{I}(\theta,\phi)$(radians)	(1.57, 0.785)	(0.98, 0.0)
Beam half-width, α (radians)	0.115	0.218

*These parameters may not reflect recent LLL updates.

2. MFTF Results.

The Mirror Fusion Test Facility (MFTF) was originally envisioned[3] as an extrapolation of standard mirror-machine technology to a larger target plasma and higher neutral-beam energy and current. A preliminary set of MFTF parameters was made available by LLL[116] and served as the basis for the MC simulation results reported in this section. At the time of this writing, however, the goals and therefore the design of the MFTF are being redirected toward possible tandem-mirror operation when the machine eventually becomes operational. Therefore, since the actual MFTF device may bear little resemblance to the conceptual design of Reference 3, the MC simulation results will not be analyzed for their impact on engineering design as will be done for the FERF results in the next section and chapter.

Using the MFTF reference design parameters of Table VI, MC simulation runs using $2(10)^5$ test particles were made for the three major beam energy components. Results of this study are summarized in Table VII. The positive ion beam current fractions f_I used to weight the aggregate results were obtained from LLL.[23,116] The global terminal particle fractions are relatively insensitive to beam component energy in this case. Approximately 14% of the injected neutral atoms are ionized by collisions with plasma electrons and approximately 53% by collisions with plasma ions. As injection energy E_I decreases from 75 to 35 keV the penetrating fraction f_p decreases as the plasma's optical thickness increases with increasing $\langle\sigma v\rangle/v$. This is offset by the increased production and escape of neutrals in the backward (beam) direction to give an increasing value of f_w as E_I decreases. The

TABLE VII

MFTF GLOBAL RESULTS

	Primary	Secondary	Tertiary	Aggregate
	E_o	$E_o/2$	$E_o/3$	$\langle E_I \rangle$
E_I (keV)	75	37.5	25	55.4
f_I [Ref. 23]	0.506	0.231	0.236	0.973
Terminal Particle Fractions:				
f_{ei}	0.135	0.154	0.156	0.144
f_{ii}	0.508	0.555	0.534	0.526
$f_t = f_{ei} + f_{ii}$	0.643	0.709	0.690	0.670
f_p	0.228	0.078	0.031	0.145
f_w	0.130	0.213	0.278	0.185
E at max $f_w(E)$(keV)	44	36	28	36-40
$\langle E \rangle$ of $f_w(E)$(keV)*	44	41	40	42
P_L/P' [Eqn. (62)]	0.30	0.31	0.48	0.35
J_I (atoms/sec)	$8.1(10)^{20}$			$8.1(10)^{20}$
$J_I(A)$	130			130
P_I(MW)	9.7			7.2
J_I'(atoms/sec)	$1.3(10)^{21}$			$1.2(10)^{21}$
$J_I'(A)$	200			193
P_I'(MW)	15.0			10.7

*Obtained by numerically averaging the Fig. 29 result.

formulae of Section A-1 of Chapter IV are used to calculate the neutral-beam injector current and power requirements for the monoenergetic E_o and aggregate cases. The imperfect beam trapping ($f_t < 1$) increases the actual injector parameters to the primed values.

The charge-transfer-produced neutral deuterium atoms bombarding the MFTF first wall are distributed in energy according to the distribution function indicated in Fig. 29, with which is compared the assumed plasma ion distribution function [Eqn. (18)]. These results are for the aggregate results of Table VII. The abscissa is here normalized to the characteristic plasma energy $\tilde{E}_p$ = 50 keV. The ordinate is normalized to 100 arbitrary units corresponding to the maximum value of the wall bombardment distribution as determined by the NUBIN simulation. The fluctuations near the peak of the wall-bombardment distribution function are a qualitative indication of the stochastic nature of the incompletely converged simulation results. The peak of this distribution is nominally 36-40 keV with an average energy of 42 keV. The high-energy tail of the plasma ion distribution contributes very little to the wall bombardment distribution for reasons suggested in Chapter II. The charge-transfer neutrals are thus preferentially drawn from the low-energy ion population.

The angular distribution of the aggregate MFTF neutral-atom first-wall bombardment is indicated in Fig. 30. The hypothetical first-wall detector surface at r_w = 200 cm is split longitudinally at ϕ = 0 radians so that the relative bombardment can be graphed as a function of polar (θ) and azimuthal (ϕ) angle. Figure 30 depicts this relative bombardment as a three-dimensional projection where the

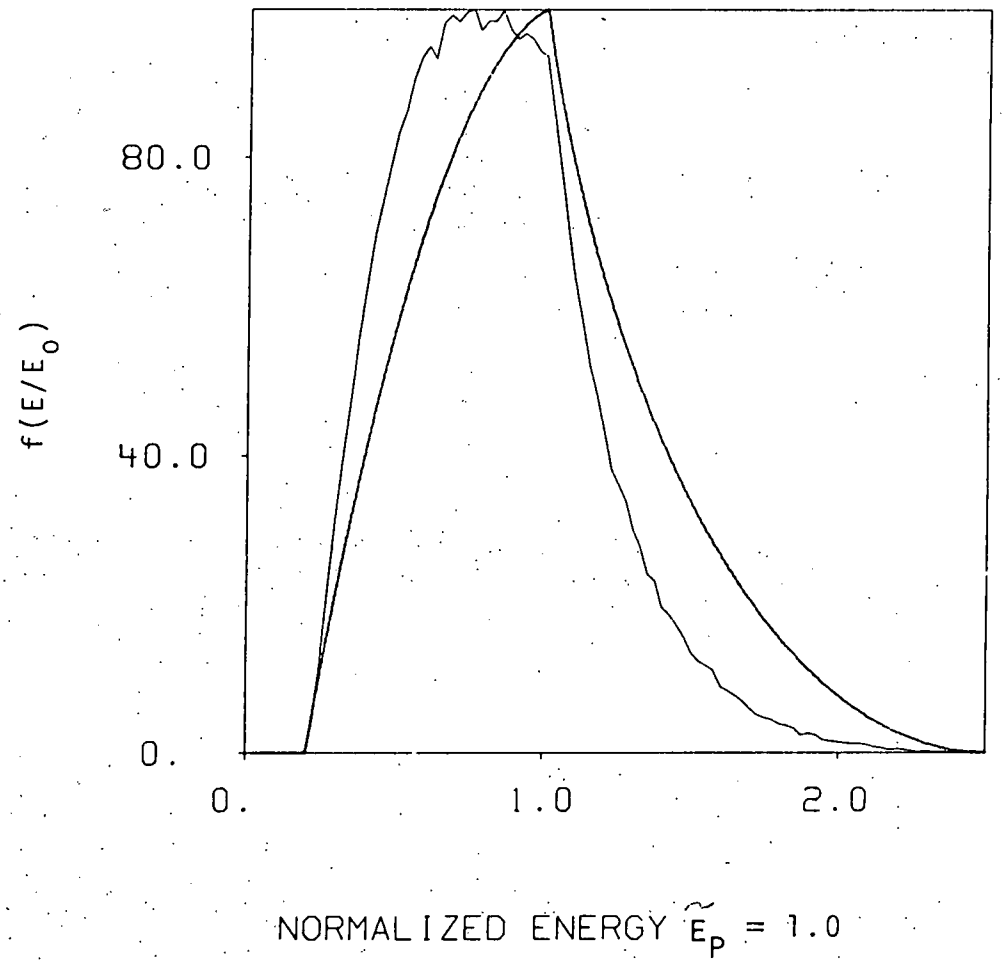

Figure 29. Normalized energy distribution for the charge-transfer-produced neutral particles escaping to bombard a MFTF first wall. $\tilde{E}_p = 1.0$ corresponds to the 50 keV peak energy of the plasma ion distribution also graphed for comparison. The average energy of the neutrals is $\langle E \rangle \sim 42$ keV.

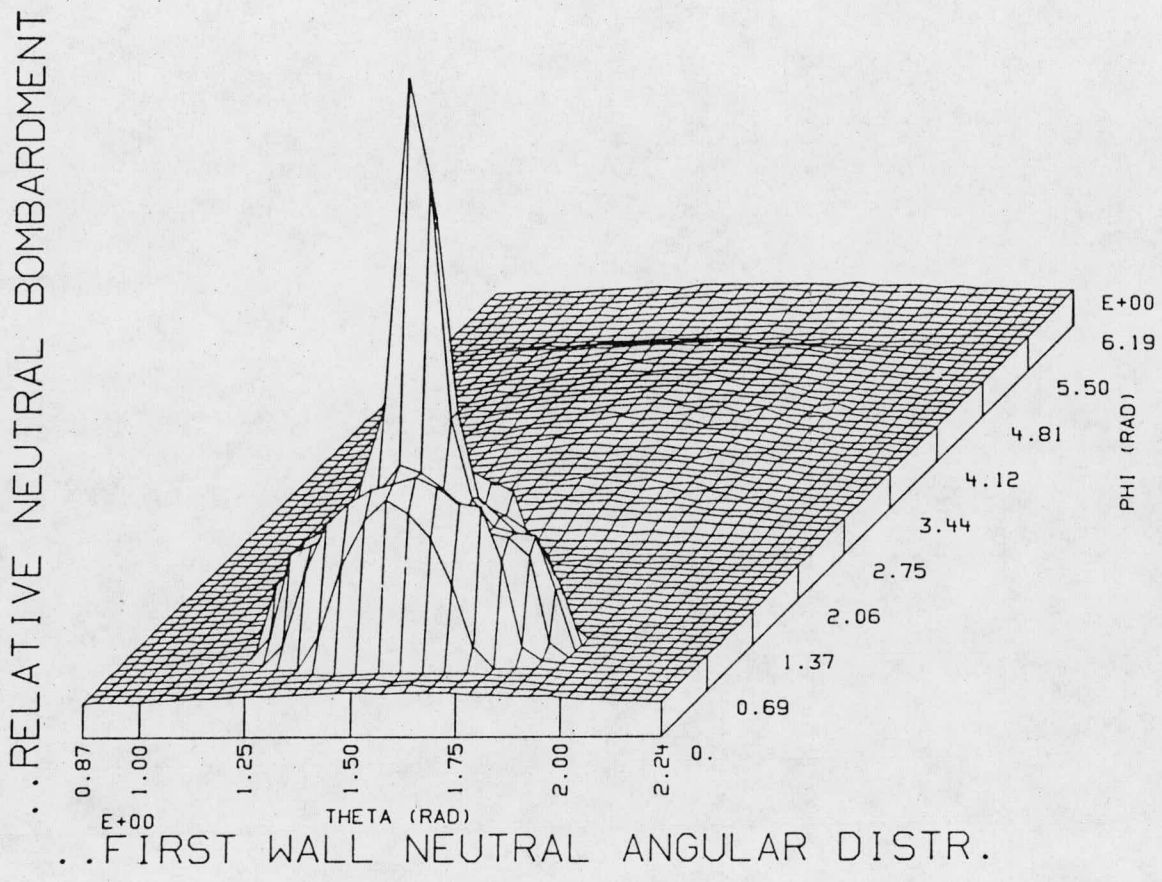

Figure 30. Angular distribution of the neutral-atom first-wall bombardment of the MFTF "first wall" at R_w = 200 cm. The peak at $\phi \sim \pi/4$ and $\theta \sim \pi/2$ represents penetrating neutrals and the lesser peak centered at $\phi \sim 5\pi/4$ and $\theta \sim \pi/2$ represents higher-generation neutrals produced in the backward (beam) direction.

height (in arbitrary units) of the surface is proportional to the magnitude of the local bombardment intensity. The surface is subdivided into a detector grid (here 32x64 resolution in θ and ϕ, respectively) in order to estimate the angular dependence. This discrete histogrammic approach and the statistical fluctuations associated with the small test particle weight value that survives to bombard the first wall result in the observed jaggedness of this surface plot. This is particularly true for the relatively small number ($N=2(10)^5$) of test particle histories run in this simulation. The peak at $\phi \sim \pi/4$ and $\theta \sim \pi/2$ represents penetrating neutrals impacting the first wall opposite the beam port while the lesser broad maximum at $\phi \sim 5\pi/4$ and $\theta \sim \pi/2$ represents the higher-generation neutrals produced in the backward (beam) direction. For higher plasma values of $\bar{n}D$, the relative dominance of these two peaks reverses. This is consistent with LLL estimates.[22]

Figure 31 depicts the same information as that of Fig. 30 on a contour map. The outermost contour bounds the region of first-wall bombardment. Successively nested contours mark regions of increasing bombardment intensity in units of the surface-averaged current or power deposition, 9.8 W/cm^2 for this MFTF aggregate simulation.

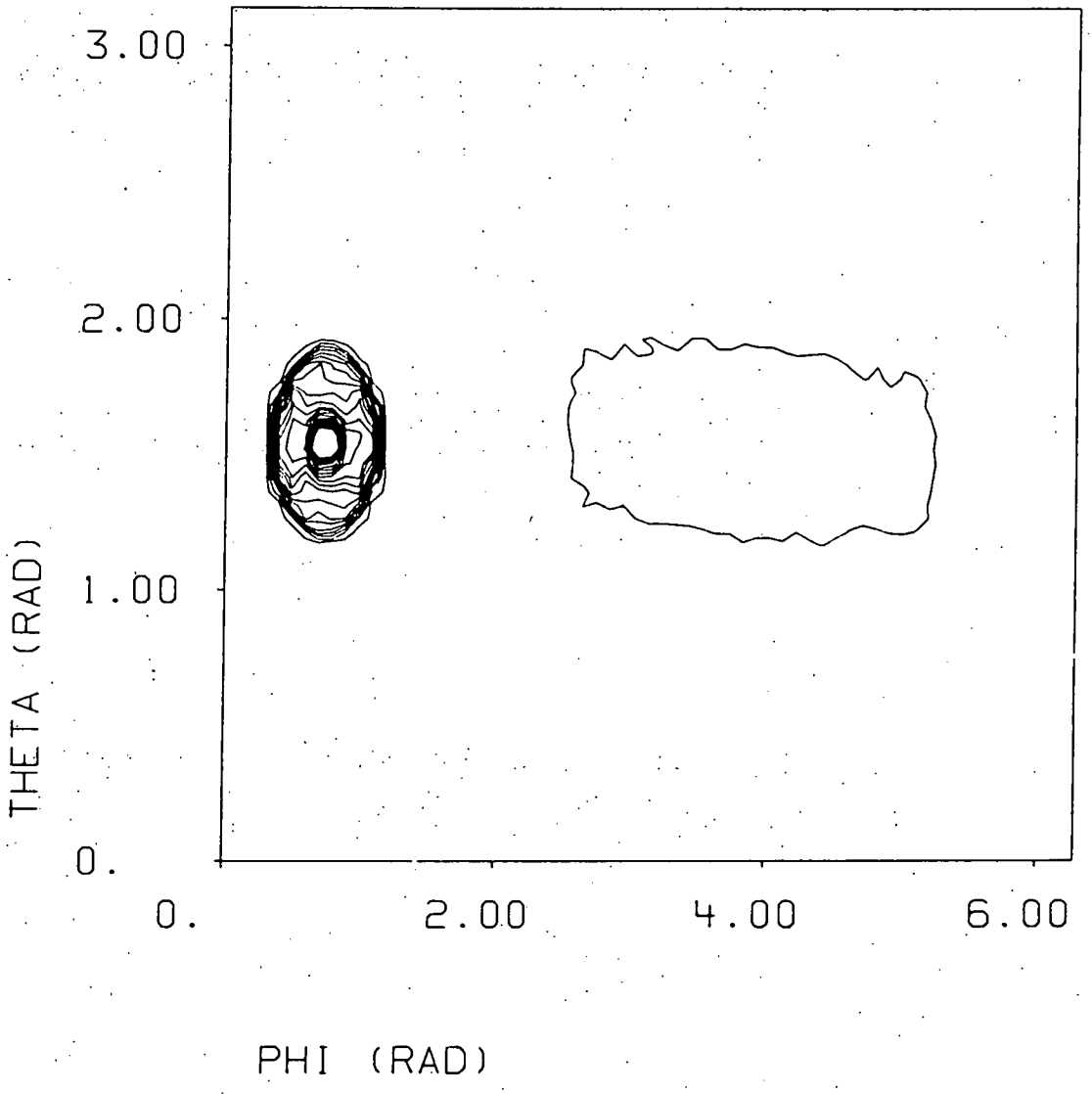

Figure 31. Angular distribution of the neutral-atom first-wall bombardment of the MFTF "first wall" at R_w = 200 cm. This contour plot illustrates the same information as Fig. 30.

3. FERF Results.

The overall design of the proposed Fusion Engineering Research Facility (FERF) is reported in detail in Ref. 6. A minor design iteration has subsequently been performed[117] but the fundamental plasma and injector parameters of interest to this study remain essentially unchanged. These parameters have been previously given in Table VI. The goals of the FERF experimental concept are to provide a reactor-grade plasma of small volume which maximizes the 14-MeV neutron flux for use in testing and evaluating anticipated reactor materials and components.[118] As noted in Chapter I, a mirror machine with a small plasma radius and a plasma energy ~ 50 keV will encounter significant beam losses due to charge-transfer collisions. Thus, this section will consider in detail the results of the MC simulation of neutral-beam injection for the FERF.

MC simulation runs eventually using $4.5(10)^5$ test particles were made for the three major FERF beam energy components. Results of this study are summarized in Table VIII. As for the MFTF, the positive ion beam current fractions used to weight the aggregate results were obtained from LLL.[23,116] The global results reported in Table VIII are qualitatively similar to the MFTF results of the previous section, as expected. Approximately 14-16% of the injected neutral atoms are ionized by electron collisions and approximately 60-70% by collisions with plasma ions to give an overall trapping efficiency of ~ 88% for the primary beam component and ~ 80% and ~ 73% for the $E_0/2$ and $E_0/3$ parasitic beam components, respectively. Again f_w increases as E_I decreases with the penetrating fraction f_p being small for all beam components.

TABLE VIII

FERF GLOBAL RESULTS

	Primary	Secondary	Tertiary	Aggregate
	E_o	$E_o/2$	$E_o/3$	$\langle E_I \rangle$
E_I(keV)	65	32.5	21.7	46.0
f_I [Ref. 23]	0.520	0.224	0.228	0.972
Terminal Particle Fractions:				
f_{ei}	0.157	0.150	0.139	0.151
f_{ii}	0.721	0.653	0.593	0.675
$f_t = f_{ei} + f_{ii}$	0.878	0.802	0.732	0.826
f_p	0.005	<0.001	<0.001	0.003
f_w	0.117	0.197	0.267	0.171
E at max $f_w(E)$(keV)	51	53	51	51
<E> of $f_w(E)$(keV)	58	57	57	57
P_L/P' [Eqn. (62)]	0.11	0.35	0.70	0.22
J_I (atoms/sec)	$1.1(10)^{21}$			$1.1(10)^{21}$
J_I (A)	180			180
P_I (MW)	11.8			8.3
J_I' (atoms/sec)	$1.3(10)^{21}$			$1.4(10)^{21}$
J_I' (A)	206			219
P_I' (MW)	13.4			10.1
Q	0.43			0.61
Q'	0.38			0.50

The charge-transfer-produced neutral deuterium atom bombardment of the first-wall surface is governed more by the background plasma ion distribution in both angle and energy than by the injection energy. The primary beam results suffice to illustrate the salient features. Figure 32 compares the energy distribution function of the escaping neutrals produced by the E_0 beam component with the assumed background plasma distribution function which peaks at $\tilde{E}_p$ = 70 keV. The ordinate is again normalized to 100 arbitrary units corresponding to the maximum value of the wall bombardment distribution as determined by the NUBIN simulation. This peak occurs at E ~ 52 keV irrespective of the beam component energy as indicated in Table VIII. As with the MFTF the charge-transfer neutrals are preferentially drawn from the low-energy ion population.

The angular distribution of the primary FERF neutral-atom first-wall bombardment is indicated in Figs. 33-34. The hypothetical first-wall detector surface at R_w = 80 cm is split longitudinally at ϕ = 0 radians. The height (in arbitrary units) of the three dimensional projection of Fig. 33 is proportional to the magnitude of the local bombardment intensity. Figure 34 depicts the same information as a contour map. The outermost contour bounds the region of first-wall bombardment to $0.7 < \theta < 2.5$ radians. Successively nested contours mark regions of increasing bombardment intensity in units of the surface-averaged current or power deposition 7.3 W/cm^2 up to a peak value of ~ 44 W/cm^2. In contrast to the MFTF results of the previous section, the dominant FERF peak at $\phi \sim \pi$ and $\theta \sim \pi/2$ represents the

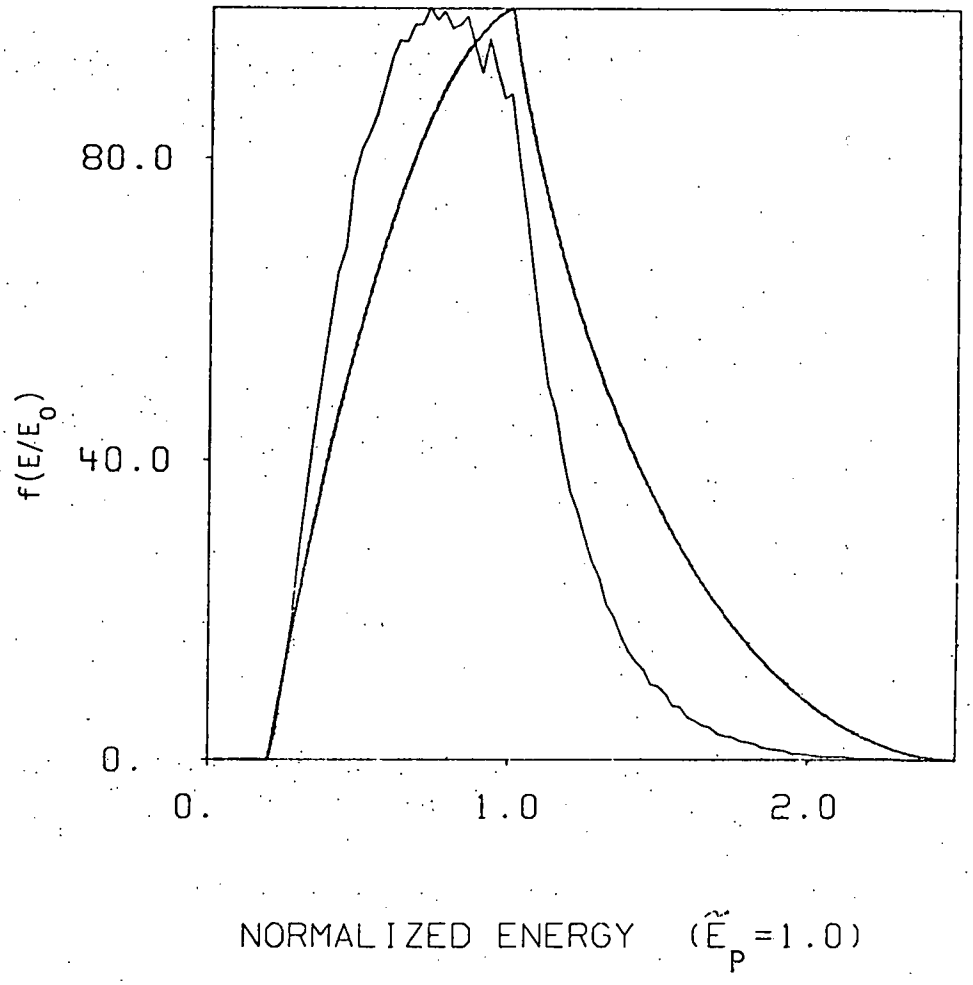

Figure 32. Normalized energy distribution for the charge-transfer-produced neutral particles associated with the primary FERF beam energy component at E_o = 65 keV. $\tilde{E}_p$ = 1.0 corresponds to the 70 keV peak energy of the plasma ion distribution also graphed for comparison. The average energy of the neutrals is 58 keV with the peak of the neutral distribution function occurring at 51 keV.

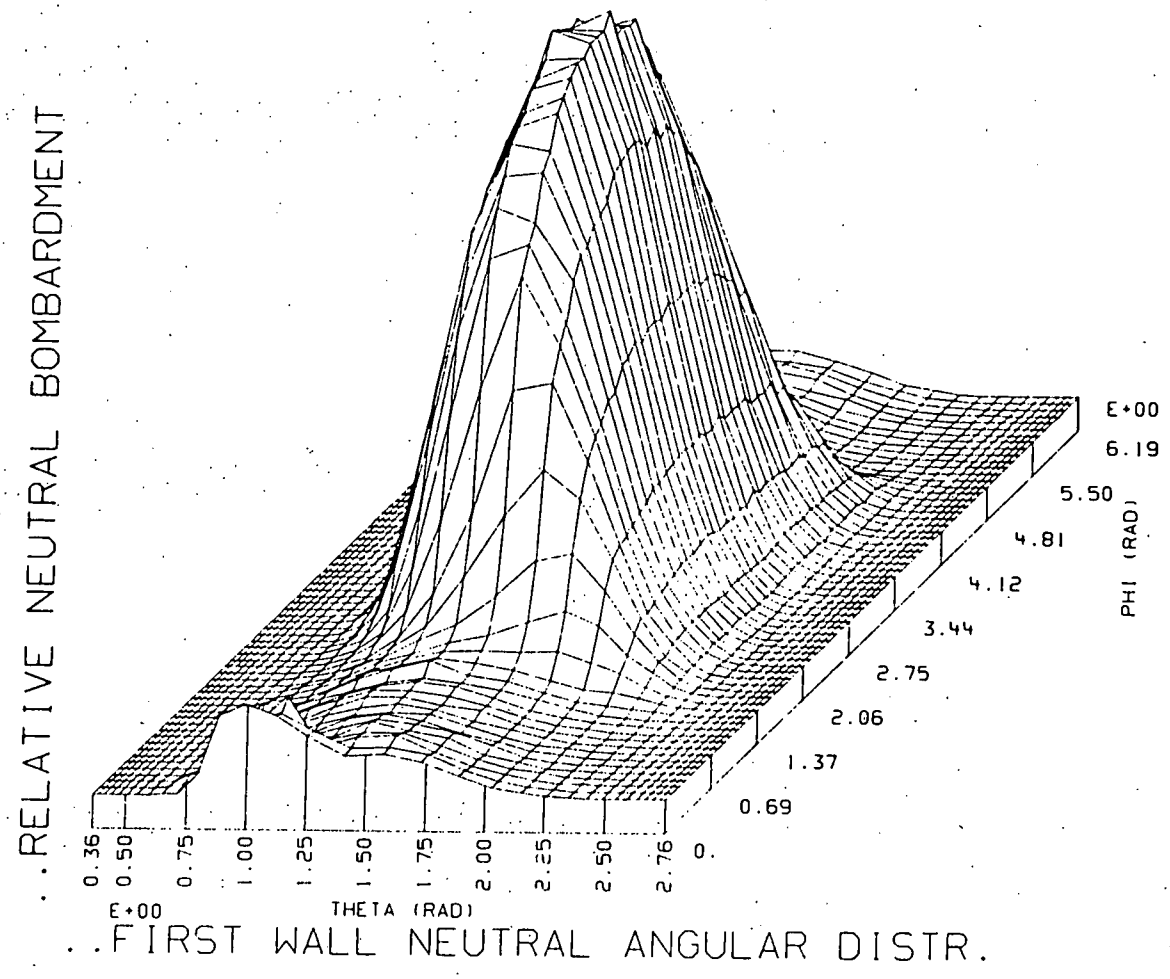

Figure 33. Angular distribution of the neutral-atom first-wall bombardment of the FERF "first-wall" at R_w = 80 cm associated with the primary beam energy component at E_o = 65 keV. The dominant peak at $\phi \sim \pi$ and $\theta \sim \pi/2$ represents the higher-generation neutrals produced in the backward (beam) direction while the lesser peak at $\phi \sim 0$ and $\theta \sim 1.3$ represents penetrating neutrals in contrast to the MFTF results of Figs. 30-31.

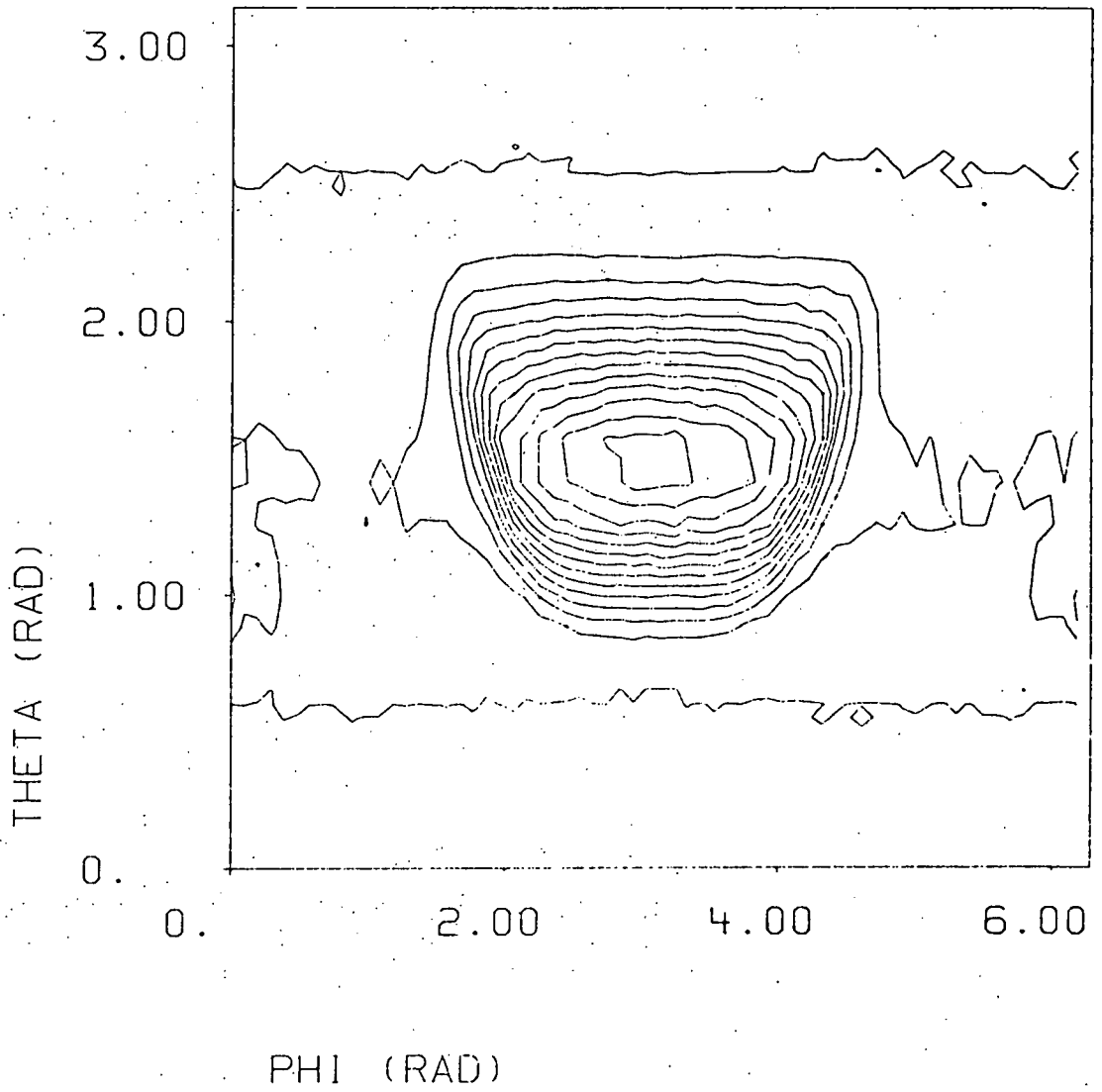

Figure 34. Angular distribution of the neutral-atom first-wall bombardment of the FERF "first wall" at R_W = 80 cm associated with the primary beam energy component at E_O = 65 keV. This contour plot illustrates the same information as Fig. 33.

higher-generation neutrals produced in the backward (beam) direction.

Before considering the FERF aggregate results an aside regarding the convergence of the MC simulation is in order. The global results of Table VIII for which the convergence parameter P_x (where x = ei, ii or w) of Chapter III-C was monitored are well-converged, even for the stringent tolerance of $\varepsilon = 0.001$. This is indicated by Table IX which displays the several global terminal particle fractions f_x and, where appropriate, the corresponding confidence factors P_x for successive interim stages in the MC simulation using $N = 4.5(10)^5$ test particles. The confidence factor parameter P_x is seen here to be a weak indicator of convergence insofar as the results at the early stages of the simulation are very close to the results for much larger values of N. But this is good if only the global results are of interest since the MC simulation may be run for a relatively small value of N for a tentative but useful result. Large values of N are, however, required to resolve the angular distribution of the first-wall bombardment, particularly if the detector grid (here 64x32) is finely meshed. Only with large N can a high-resolution, smooth contour plot like that of Fig. 32 be expected. Even for $N > 4(10)^5$ a certain amount of jagged behavior remains.

A weighted average of the three simulation runs for the respective FERF beam energy components produces the aggregate global results in the rightmost column of Table VIII. The aggregate wall-bombardment energy distribution function is depicted in Fig. 35 and is seen to be essentially identical to the primary beam results of Fig. 32. The peak of the neutral distribution occurs at E ~ 51 keV and <E> ~ 57 keV.

TABLE IX

FERF GLOBAL RESULTS CONVERGENCE FOR $\varepsilon = 0.001$

PRIMARY BEAM COMPONENT: $E_I = 65$ keV

N Test Particles	f_p	f_{ei}	P_{ei}	f_{ii}	P_{ii}	f_w	P_w
$2.50(10)^4$	.0050	.1575	.336	.7219	.276	.1217	.371
$5.00(10)^4$	.0050	.1573	.461	.7211	.382	.1227	.504
$1.00(10)^5$	.0051	.1573	.615	.7211	.519	.1225	.665
$2.00(10)^5$	.0052	.1573	.780	.7208	.681	.1229	.827
$3.00(10)^5$	.0052	.1573	.867	.7208	.778	.1230	.905
$4.00(10)^5$	.0052	.1573	.918	.7208	.841	.1229	.946
$4.50(10)^5$	.0053	.1572	.935	.7207	.865	.1230	.959

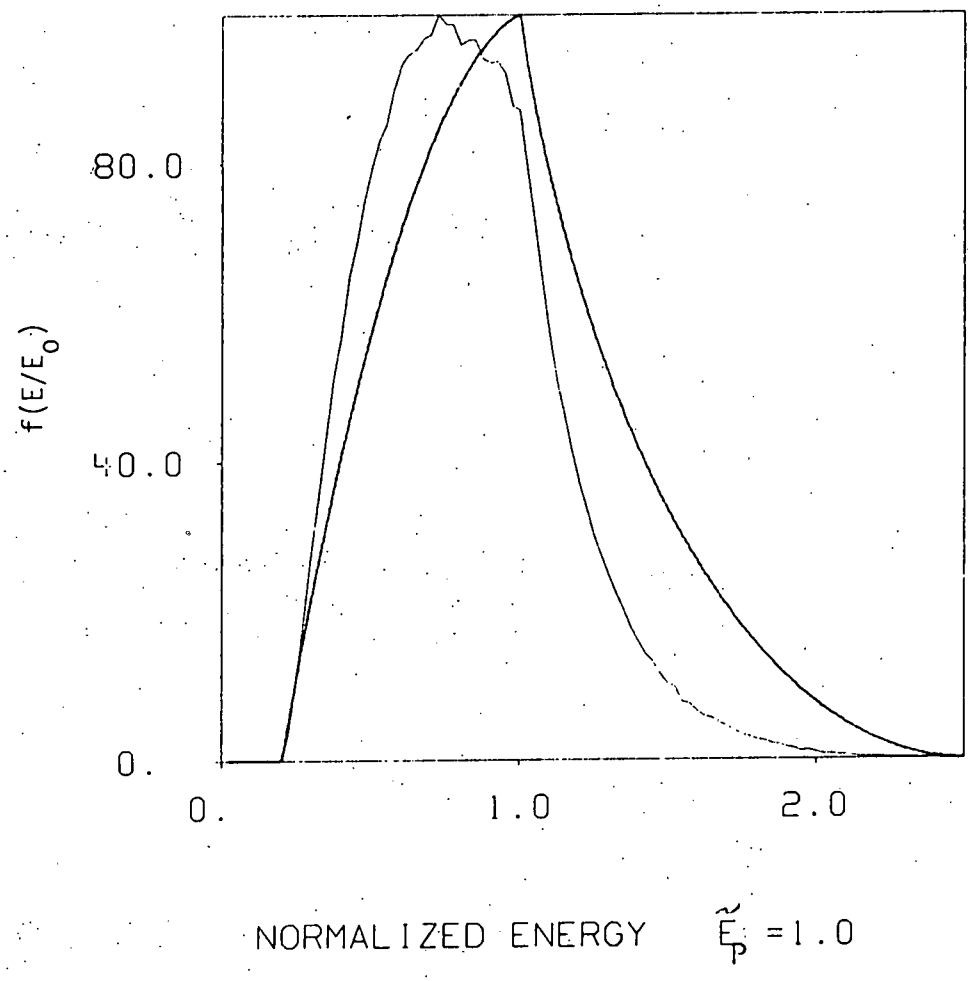

Figure 35. Normalized energy distribution for the charge-transfer-produced neutral particles escaping to bombard a FERF first wall. $E_p = 1.0$ corresponds to the 70 keV peak energy of the plasma ion distribution also graphed for comparison. The average energy of the neutrals is $\langle E \rangle \sim 58$ keV.

The angular distribution of the aggregate FERF neutral-atom first-wall bombardment is indicated in Figs. 36-37. The penetrating neutrals represent a very small effect now so that only the higher-generation peak at $\phi \sim \pi$ and $\theta \sim$ 1.4 is significant. As before, the first-wall bombardment is limited to $0.7 < \theta < 2.5$ radians. The surface-averaged power deposition is now 11 W/cm^2 and the peak value is 69 W/cm^2. The position of the maximum of the backward (beam) directed intensity is no longer precisely coincident with the beam port, as suggested by the spherical models.[22] Rather, the polarization of the neutrals by the anisotropic ion phase-space distribution shifts the maximum toward the first-wall midplane at $\theta \sim \pi/2$ and decouples it somewhat from the original injection orientation. The FERF injection system was designed,[6] however, to accommodate injection through up to four beam ports arranged azimuthally about the plasma. Renormalization and superposition of the results of Fig. 37 consistent with this configuration gives the effect seen in Fig. 38 as a function of θ and ϕ or the same result in Fig. 39 as a function of z and ϕ for R_w = 80 cm. There is now, as a result of superposition of the local bombardment of the four beams, a band of intensity around the plasma in which are seen four local maxima. The average power deposition is now ~ 18 W/cm^2 with peak values of ~ 115 W/cm^2 at R_w = 80 cm.

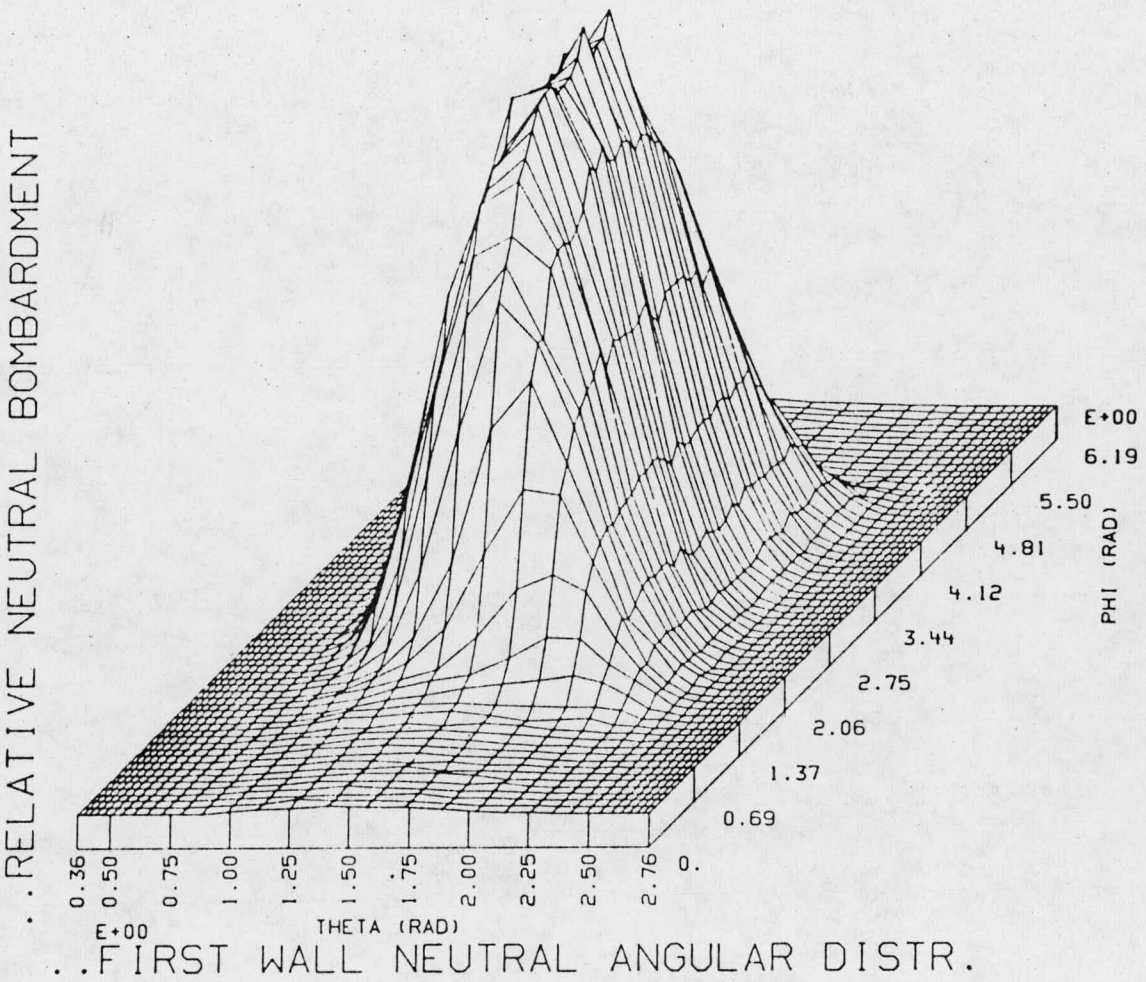

Figure 36. Angular distribution of the neutral-atom first-wall bombardment of the FERF "first wall" at R_W = 80 cm. The peak at $\phi \sim \pi$ and $\theta \sim 1.4$ represents higher-generation neutrals produced in the backward (beam) direction.

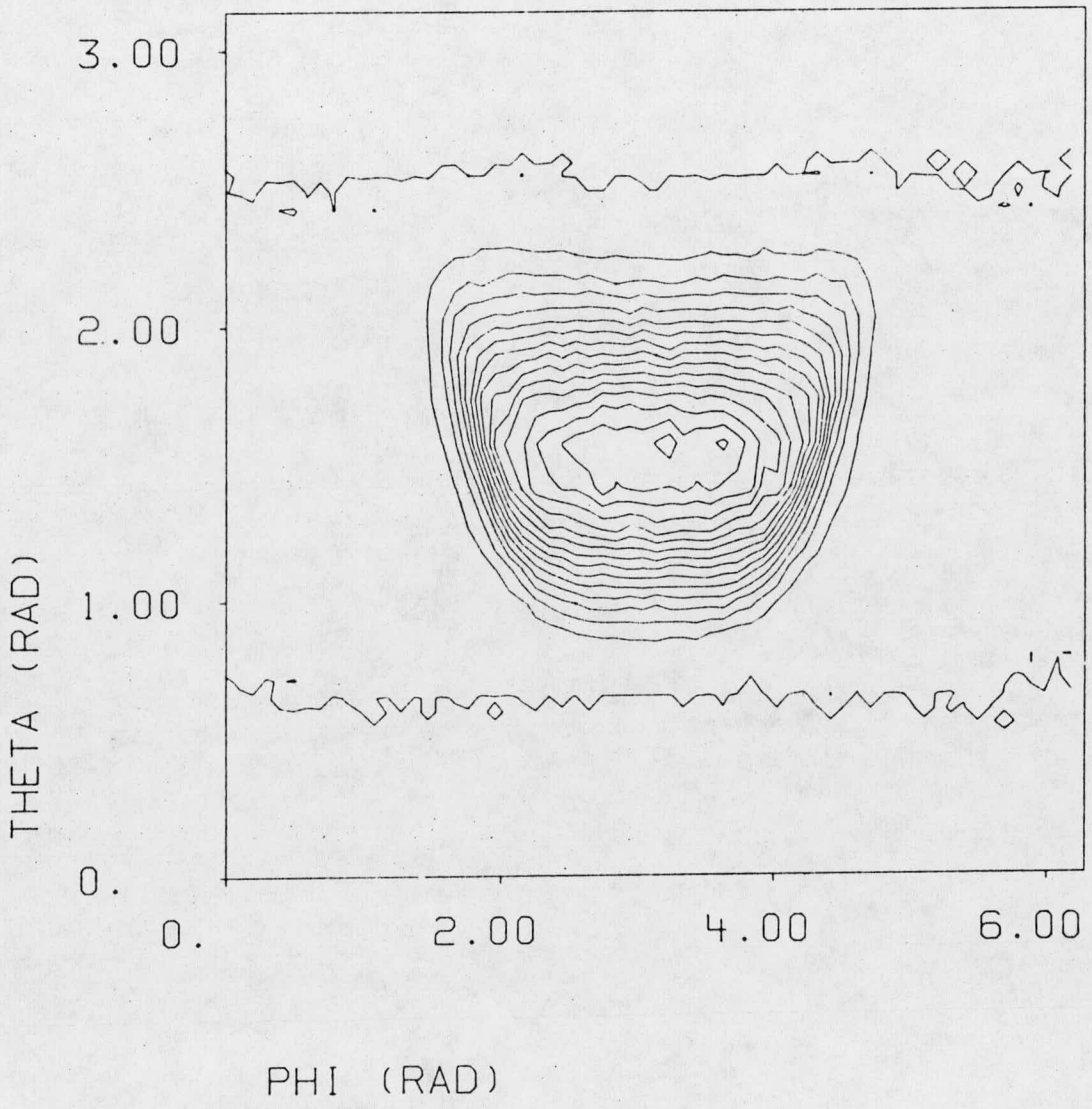

Figure 37. Angular distribution of the neutral-atom first-wall bombardment of the FERF "first wall" at R_W = 80 cm. This contour plot illustrates the same information as Fig. 36.

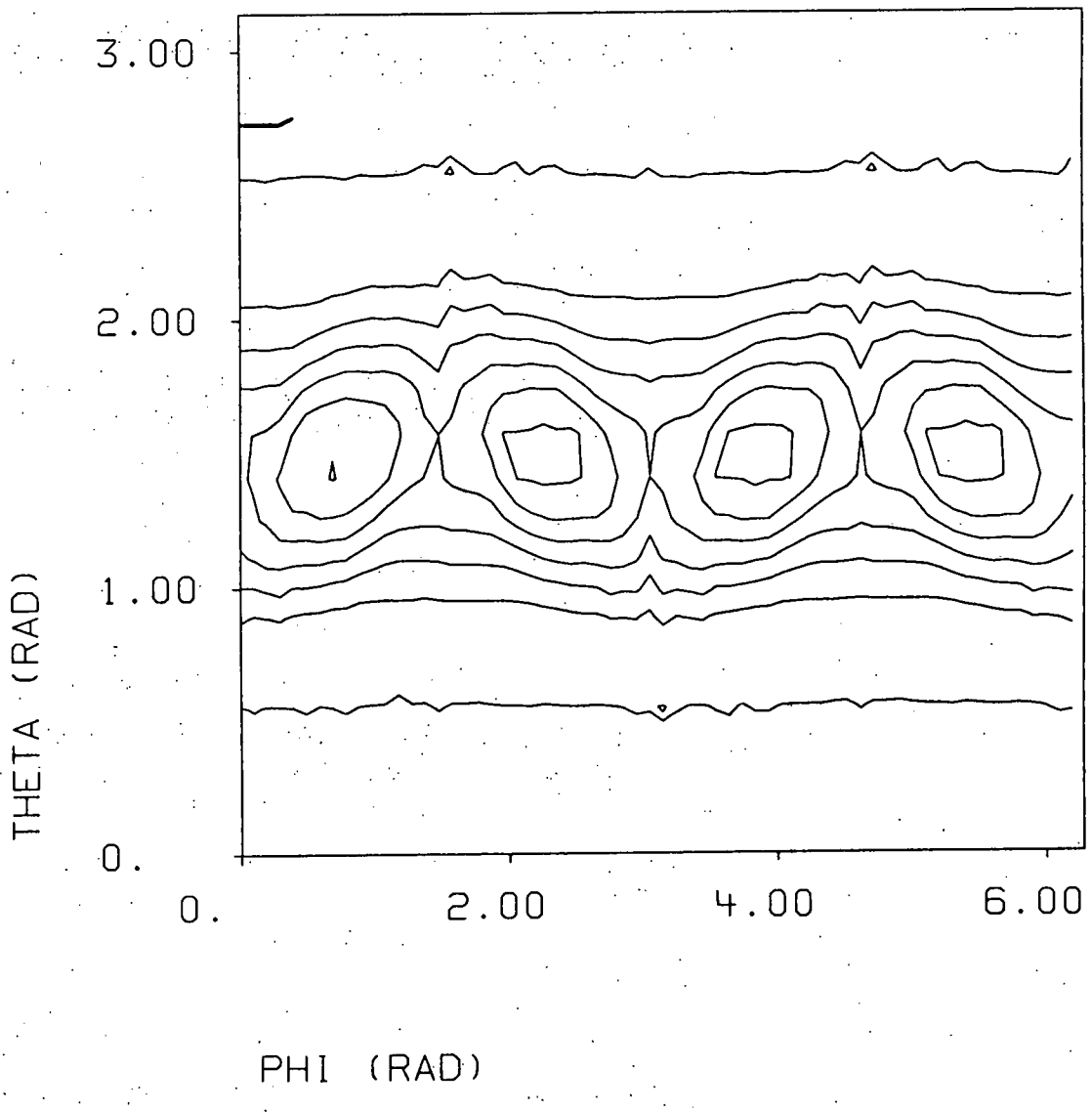

Figure 38. Angular distribution of the neutral-atom first-wall bombardment of the FERF "first wall" at R_W = 80 cm. The results of Fig. 37 have been renormalized to represent a four-beam injector configuration.

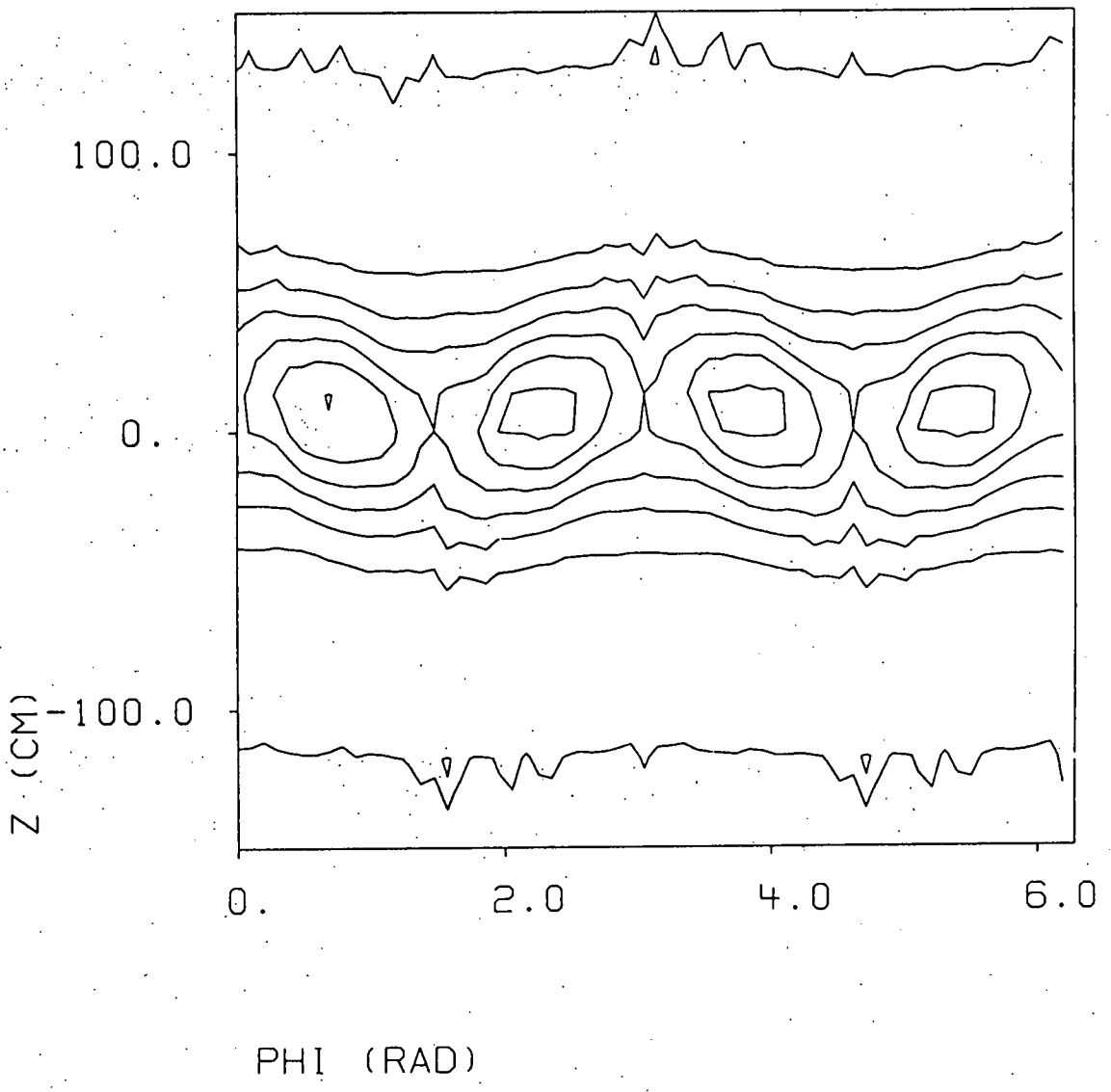

Figure 39. Angular distribution of the neutral-atom first-wall bombardment of the FERF "first wall" at R_w = 80 cm. The results of Fig. 37 have been renormalized to represent a four-beam injector configuration. Note the change from θ - ϕ to z - ϕ coordinates.

VI. FIRST-WALL ENGINEERING IMPLICATIONS

A. Surface Heat Flux.

The MC simulation results of the previous chapter indicate a non-uniform surface heat flux averaging ~ 18 W/cm^2 (peak value ~ 115 W/cm^2) at the hypothetical FERF first-wall radius (R_w = 80 cm). For a real first wall with radius closer to the midplane plasma radius (R_p = 25 cm), the local heat flux may be expected to increase approximately as R_w^{-1}. The discussion of the engineering design of the FERF first wall contained in Ref. 6 can now be reexamined in light of these results in order to assess their impact on materials choice, heat removal requirements and, in the next section, sputtering erosion and lifetime.

Using thermal stress and heat-removal rate constraints, the maximum allowable surface heat flux for the FERF has been estimated[6, 119] for various candidate materials. Following Fig. J-12 of Ref. 6, Table X summarizes these estimates. The upper (short time) limit applies to transient start-up or accident conditions in which the target plasma might be lost and the neutral beam would illuminate the first wall on the far side (in the notation of previous chapters, f_p = 1). The lower (standard operation in steady state) limit, taken to be approximately one-half of the upper limit, provides the limit of interest to this study insofar as it applies to the steady-state results of Chapter V.

The neutral-atom bombardment is the dominant contribution to the first-wall surface heating. Since the energetic neutral particles penetrate only 1-10 μm into the surface, the approximation of surface heating is made. By contrast the ~ 200 W/cm^2 of incident 14-MeV neutrons in the FERF will deposit their energy on a volumetric basis in the

TABLE X

FIRST-WALL HEAT FLUX LIMITS (W/cm^2)*

Candidate Material	Steady-State Limit**	Short-time Limit
Pure T	300	600
SAP-895 (120°C limit)	1000	~2000
Al-6061 (120°C limit)	1000	~2000
FS-85	1000	~2000
Nb-1Zr (400°C limit)	1000	~2000
Mo-0.5 T	2400	4900
Ta-10W (1000°C limit)	3200	6400

*Following Fig. J-12 of Ref. 6.

**Assuming water coolant with $\Delta p/p = 0.5$ and thermal stresses at one-third of the allowable yield stress.

structures behind the first wall or in materials test assemblies. If the separation of the first wall from the plasma is greater than the gyro-orbit of charged particles, as is the case for the FERF, charged particles will contribute very little to the surface heating. Radiation, both bremsstrahlung and synchrotron, contributes less than 2 W/cm^2 on average to the FERF first wall.

The anticipated FERF first-wall surface heating from charge-transfer-produced neutral atom bombardment at R_w = 30 cm is summarized in Table XI. LLL estimates[6,22,120] have been renormalized to reflect the 4-beam injector configuration considered in this study. The total injector current requirements are based on the respective estimates of the classical plasma loss rate. Under these circumstances the peak energy deposition rate is well below the materials limits of Table X. The potential for anomalous plasma loss rates has lead to the incorporation of FERF injector design capabilities of up to a factor of three greater than the classical injection requirement assumed in Table XI. In that event the design margin for energy deposition in the absence of a target plasma is eliminated for all candidate materials other than Mo and Ta. It may be noted that the global LLL estimates for the particle and energy deposition with plasma for the primary neutral-beam component are in good agreement with the MC simulation results. Thus, no recommendations for FERF design changes are made here.

B. Physical Sputtering.

The MC simulation results of Chapter V provide neutral particle fluxes and energy spectra which can be incorporated into models of

TABLE XI

FERF Neutral-Particle First Wall Heating[1]

	LLL Estimate[2] E_o = 65 keV	This Study[3] E_o	This Study[3] <E>
With no plasma			
Illuminated area (cm^2)	8100	8100	8100
Injector power (MW)	2.7	3.4	2.5
Amps to the wall (A)	36	45	45
Power to the wall (MW)	2.7	3.4	2.5
Energy deposition (W/cm^2)	330	420	309
With plasma			
Amps to the wall (A)	23	25	37
Power to the wall (MW)	1.7	1.5	2.2
Energy deposition			
Average (W/cm^2)	< 53	30	40
Peak (W/cm^2)	<198	180	264

[1]Four-injector configuration (cf. Fig. 38) and classical injection requirement

[2]References 6, 22, 120

[3]From Table VIII

the physical sputtering of atoms from surfaces to give estimates of the FERF first-wall lifetime.[121-126] The subsequent effect, the reflux of impurity atoms into the plasma will not be treated here. The discussion here is limited to niobium which was found in the preceeding section to be a generally acceptable first-wall material from a thermal stress and heat transfer viewpoint. Near-normal incidence of the bombarding particles, which minimizes the sputtering yield, is assumed. Only for those few neutrals impinging $>\pi/4$ radians off normal is this a poor approximation.

The treatment of sputtering incorporated into SUBROUTINES SPUTS and SPUTRA of the NUBIN code is consistent with that used for the design of the UWMAK-I tokamak reactor[126] and the Reference Theta-Pinch Reactor[127-129] as well as work done independent of particular fusion reactor designs.[130-132] Physical sputtering is defined for present purposes as the ejection from the first-wall surface of metallic atoms which have been displaced from their lattice positions by momentum transfers as a result of collisions with incident high-speed neutral atoms. The microscopic cross section σ_d for displacing of heavy ions by light incident atoms has three forms depending upon the incident energy. For $E < E_A$ (=4.1 keV for D→Nb)[126], E_A is given by

$$E_A = 2E_R Z_1 Z_2 (Z_1^{2/3} + Z_2^{2/3})^{1/2} \left(\frac{M_1 + M_2}{M_2}\right) \qquad (75)$$

where E_R = 13.6 eV and Z_i and M_i are the atomic number and atomic weight of the projectile (1) and target (2) atoms, respectively. The collisions are represented by the hard-sphere collision cross section

$$\sigma_d = \pi \left[Z_1 Z_2 e^2 \left(\frac{M_1 + M_2}{M_2}\right) E \right]^2 \left[1 - \frac{E_d}{E_{max}}\right] \qquad (76)$$

where E_d (= 16.2 keV for Nb) is the lattice displacement energy and E_{max} is the maximum possible energy transfer to the primary knock-on atom (PKA) given by

$$E_{max} = \frac{4M_1M_2E}{(M_1 + M_2)^2} \quad . \tag{77}$$

The FERF plasma considered in this study does not produce neutral particles with energies less than E_A. Hence, this low-energy regime is only of passing interest.

For incident projectile energies satisfying $E_A < E < E_B$ (= 14.0 keV for D→Nb)[126] given by

$$E_B = 4\, E_R^2\, Z_1 Z_2 (Z_1^{2/3} + Z_2^{2/3})^{1/2}\ \frac{M_1}{M_2\, E_d} \tag{78}$$

the displacement cross section becomes that of a weakly screened Coulomb collision

$$\sigma_d = \pi \frac{a_o^2}{(Z_1^{2/3} + Z_2^{2/3})^{1/2}} \tag{79}$$

where $a_o = 5.292(10)^{-9}$ cm is the Bohr radius.

Above E_B, where most of the neutral atoms of the FERF case are produced (cf. Figs. 32, 35), the displacement cross section is represented by the Rutherford scattering cross section

$$\sigma_d = \frac{4\pi a_o^2\, M_1\, Z_1^2 Z_2^2 E_R^2}{M_2 E_d E} \left(1 - \frac{E_d}{E_{max}}\right) \quad . \tag{80}$$

The number of first-wall atoms sputtered per incident neutral particle with energy E is the sputtering ratio S(E) given by [126]

$$S(E) = \frac{(\sigma_d\, \bar{E}\, n^{2/3})}{4E_d} \left[1 + \frac{\log(\bar{E}/E_s)}{\log 2}\right]^{1/2} \tag{81}$$

where $n(= 5.56(10)^{22}$ cm^{-3} for Nb) is the atomic density of the target, E_s is the sublimation energy (= 7.25 keV for Nb)[121] and $\bar{E}$ is the average PKA energy taken to be

$$\bar{E} = E_d \log (E_{max}/E_d) \quad . \tag{82}$$

The curve of S(E) obtained in this fashion peaks at approximately 0.20 atoms/atom for E ~ 15 keV and thus overestimates the available experimental results.[121,130] To better match the experimental results the curve of S(E) is displaced downward by a factor of three giving the peak value of S(E) ~ 0.007 at E ~ 15 keV.

The energy spectrum of incident neutral atoms is used to compute an average value <S> of the sputtering yield according to

$$\langle S \rangle = \frac{\int_0^\infty S(E)\, f_w(E)\, dE}{\int_0^\infty f_w(E)\, dE} \tag{83}$$

where S(E) is calculated from Eqn. (81), incorporating the normalization to experiment, and $f_w(E)$ is obtained from the NUBIN code (cf. Figs. 32, 35). This average sputtering rate can be used to determine the erosion rate R of the first wall material using

$$R = \langle S \rangle \frac{\Phi\, M}{N_A\, \rho} \tag{84}$$

where Φ is the incident particle flux density, M(= 92.91 g/mole for Nb) is the atomic weight of the wall material, ρ(= 8.57 g/cm^3 for Nb) is mass density of the material and $N_A = 6.025(10)^{23}$ atoms/mole is Avagadro's number. Thus for niobium $R = 5.7(10)^{-15}$ $\langle S \rangle \Phi$ mm/year. The sputtering results for the FERF case are summarized in Table XII. It may be noted that S(<E>) provides a good approximation of the spectrum-

TABLE XII

FERF First-Wall Sputtering Erosion Results
for the Primary Beam Component and Aggregate Cases

	E_o = 65 keV	<E>
<E> of f_w (keV)	58	57
S(<E>)(atoms/atom)	$2.6(10)^{-3}$	$2.6(10)^{-3}$
<S>	$2.7(10)^{-3}$	$2.8(10)^{-3}$
Avg. Φ (atoms/cm^{2}s)	$3.2(10)^{15}$	$4.4(10)^{15}$
Peak Φ (atoms/cm^{2}s)	$1.9(10)^{16}$	$2.8(10)^{16}$
Avg. R (mm/year)	$4.9(10)^{-2}$	$7.0(10)^{-2}$
Peak R (mm/year)	$2.9(10)^{-1}$	$4.5(10)^{-1}$

averaged value <S> obtained from Eqn. (83). This agreement in the particular case of the FERF results from the concentration of neutrals near the peak of the S(E) curve such that S(E) is nearly constant. The nominal FERF first wall thickness is δ = 0.5 mm, which suggest a lifetime limit due to sputtering along of less than one year for areas of peak neutral particle bombardment. While this might be tolerable in a near term test facility where one might expect to sacrifice components in the interest of gaining information on materials behavior, it would be unacceptable in a commercial fusion reactor. Also, as in the previous section, if non-classical losses require higher neutral-beam injection currents, the erosion rates of Table XII will have to be scaled upward accordingly and the lifetime estimate will be correspondingly reduced.

VII. CONCLUSIONS AND RECOMMENDATIONS FOR FURTHER STUDY

Monte Carlo simulation techniques have been developed which permit the modeling of neutral-beam trapping in realistic mirror-machine plasma configurations and in addition provide information on neutral-particle first-wall surface heating and sputtering erosion of interest to engineering-design studies. Application of these techniques to idealized benchmark calculations and to the MFTF and FERF systems confirms the qualitative conclusions of previously developed simple models insofar as the global beam trapping efficiency results are concerned only in a broad sense. The restrictions inherent in the simpler models tend to dictate their results. Only by generally relaxing those restrictions, as is allowed by the MC method, can the conflicting influences of these restrictions be sorted out. Beyond this, however, new aspects of the model; including the effect of higher-generation neutral particles, anisotropic distributions in three-dimensional target-plasmas, self-consistent interaction cross sections, and the resolution of neutral-particle energy spectra; provide information and insight not previously available. For the first time the anisotropic phase space distribution function of the mirror-confined plasma ions has been used to calculate self-consistent charge transfer and ionization rate coefficients. For the first time the tracking of charge-transfer-produced through more than one generation has been accomplished. For the first time the radial and axial plasma density profiles of Yin-Yang mirror systems have been used in beam trapping calculations. For the first time the availability of the angular and energy distributions of the neutral particle bombardment of the first wall has enabled the calculation of

nonuniform surface heating and sputtering erosion rates under the condition of the superposition of multiple beam sources. The angular distribution of the charge-transfer-produced neutral particles has been shown to be determined more by the anisotropic plasma ion distribution than by the original injection orientation. The computational framework developed for this study can accommodate the incorporation of more realistic physics as it becomes available from either theoretical work or experimental observation of mirror devices.

As is often the case, a research effort such as this identifies new opportunities for study and leaves some "loose-ends" in the effort to focus on key questions. The following recommendations for future study are therefore made in order to advance this work.

- In steady state, there will be a balance of neutral particles at the mirror machine first wall between those energetic neutrals coming from the plasma and those reflecting from the first-wall surface or those cold neutrals dislodged by neutral-particle impact. A self-consistent study could follow these reflux neutrals back into the plasma where they will undergo charge transfer interactions and increase the effective energy loss rate per original beam particle.
- The energy distributions assumed for the target plasma are calculated by separate Fokker-Planck calculations. The Monte Carlo computations of this study provide a source term which may differ from that originally assumed for the Fokker-Planck calculations. Some technique for iterative

adjustment or renormalization should be developed to make these two aspects of the total model more self-consistent.

- The NUBIN code in its present form is rather ill-adapted for parametric studies. Some further code optimization to speed it up (or simply an implementation on a faster computer) and incorporation of algorithms to perform sensitivity analyses of the results would be useful.
- The code could be applied to other systems heated by neutral beams; for example the end-cells of the Tandem Mirror Experiment (TMX), the Field-Reversed Mirror (FRM), or Tokamak Fusion Test Reactor (TFTR). In the latter case a substitution of a toroidal geometry option would have to be provided.
- The code in its present form is limited to steady-state calculations. A technique to model the start-up phase of a mirror device, perhaps using a sequence of quasi-steady interim stages might prove useful.
- The code results should be compared with charge-transfer-analyzer diagnostic measurements of the neutral-particle energy spectrum where possible.

Application of the code in its present form to the reference case studies of the MFTF and the FERF has not uncovered any fatal design flaws. The uncertain extrapolation of currently understood mirror-plasma particle confinement physics has lead to the incorporation of liberal engineering design margins sufficient to handle the peak heat

loads predicted by this study if confinement is nearly classical. The identification made possible by this study of the areas of the first wall surface at which the peak heating rate may be expected will allow more careful refinement and optimization of the preliminary designs of these systems.

REFERENCES

1. R. F. Post, "LLL Magnetic Fusion Research: The First 25 Years," Energy and Technology Review (UCRL-52000-78-5), 1-13, (May 1978).

2. R. F. Post, "Recent Mirror Machine Results and Their Implications for Mirror Systems," UCRL-77221, (15 August 1975).

3. F. H. Coensgen, ed., "MX Major Project Proposal," Lawrence Livermore Laboratory Report LLL-Prop-142, (1976).

4. R. W. Moir, et al., "Preliminary Design Study of the Tandem Mirror Reactor (TMR)," UCRL-52302, (15 July 1977).

5. R. S. Devoto, G. A. Carlson, and J. D. Hanson, "Engineering Parameters of a Field-Reversed Mirror Reactor Cell," UCID-17737, (1977).

6. T. H. Batzer, et al., "Conceptual Design of a Mirror Reactor for a Fusion Engineering Research Facility (FERF), UCRL-51617, (28 August 1974).

7. F. H. Coensgen, "Mirror Machine Program in the USA," UCRL-79870, (2 September 1977).

8. N. Metropolis and S. Ulam, "The Monte Carlo Method," Journal of the American Statistical Association, 44, 247, 335-341, (September 1949).

9. J. M. Hammersley and D. C. Handscomb, Monte Carlo Methods, (Methuen & Co. Ltd., London), (1964).

10. R. W. Moir and C. E. Taylor, "Magnets for Open-Ended Fusion Reactors," Proc. Sym. Tech. of Controlled Thermonuclear Fusion Experiments and the Engineering Aspects of Fusion Reactors, Austin, TX, CONF-721111, 853-883, (1974), also UCRL-74326, (15 November 1973).

11. D. R. Sweetman, "Ignition Condition in Tokamak Experiments and Role of Neutral Injection Heating," Nuclear Fusion, 13, 157-165, (1973).

12. J. E. Sharer, R. W. Conn, and D. T. Blackfield, "Study of Radio-frequency and Neutral Beam Heating of Large Tokamaks," UWFDM-148, (December 1975).

13. H. S. Staten, ed., "Proceedings of the Plasma Heating Requirements Workshop," CONF-771241, (1977).

14. A. H. Futch, Jr., et al., "Plasma Production by Neutral-Atom Injection: Equations and Numerical Solutions," The Physics of Fluids, 5, 10, 1277-1287, (October 1962).

15. A. Simon, "Alternative Neutral Burnout Equation," The Physics of Fluids, 2, 336-337, (1959).

16. R. J. Colchin, "Target Plasma Trapping," Nuclear Fusion, 11, 329-337, (1971).

17. A. C. Riviere, "Penetration of Fast Hydrogen Atoms into a Fusion Reactor Plasma," Nuclear Fusion, 11, 363-369, (1971).

18. J. Hovingh and R. W. Moir, "Efficiency of Injection of Neutral Beams into Thermonuclear Reactors," Nuclear Fusion, 14, 629-637, (1974), also UCRL-51419, (17 July 1973).

19. J. Hovingh, "The Effect of Component Performance Perturbations on Neutral Beam Injection System Performance in Thermonuclear Reactors," UCID-16360, (3 October 1973).

20. R. L. Miller, "Neutral-Beam Injection: Preliminary Analysis of Charge-Exchange Losses," University of Illinois Report PFP-TM-08, (25 February 1974).

21. R. L. Miller and G. H. Miley, "Charge-Exchange Losses During Neutral-Beam Injection," First IEEE International Conference on Plasma Science, Knoxville, TN, 74CH0922-5-NPS, 39-40, (May 1974).

22. G. A. Carlson and G. W. Hamilton, "Wall Bombardment Due to the Charge Exchange of Injected Neutrals with a Fusion Plasma," First Topical Meeting on the Technology of Controlled Nuclear Fusion, San Diego, CA, CONF-740402-P1, 401-416 (16-18 April 1974), also Appendix C of Ref. 6 and UCRL-75306, (April 1974).

23. D. J. Bender and G. A. Carlson, "Fusion Plasma Losses Due to the Charge Exchange of Injected Neutrals," UCRL-76438, (1 April 1975).

24. T. B. Kaiser, "Monte Carlo Neutral Transport Code," Magnetic Fusion Energy Quarterly Report — October through December 1977, UCRL-50551-77-4, 45-47 (28 February 1978).

25. T. B. Kaiser, "Neutral Particle Transport in Mirror Machines: Monte Carlo Simulation," Proc. of the Annual Controlled Fusion Theory Conference, Gatlinburg, TN, B6, (April 1978).

26. M. H. Hughes and D. E. Post, "Monte Carlo Algorithm for Calculating Neutral Gas Transport in Plasmas," PPPL-1335, (March 1977).

27. J. David Jackson and Harry Schiff, "Electron Capture by Protons Passing through Hydrogen," Physical Review, 89, 2, 359-365, (15 January 1953).

28. Edgar Everhart, Gerald Stone, and R. J. Carbone, "Classical Calculation of Differential Cross Section for Scattering from a Coulomb Potential with Exponential Screening," Physical Review, 99, 4, 1287-1290, (15 August 1955).

29. P. M. Stier and C. F. Barnett, "Charge Exchange Cross Sections of Hydrogen Ions in Gases," Physical Review, 103, 4, 896-907, (15 August 1956).

30. Michâl Gryzinski, "Stopping Power of a Medium for Heavy, Charged Particles," Physical Review, 107, 6, 1471-1475, (15 September 1957).

31. C. F. Barnett and H. K. Reynolds, "Charge Exchange Cross Sections of Hydrogen Particles in Gases at High Energies," Physical Review, 109, 2, 355-359, (15 January 1958).

32. Samuel K. Allison, "Experimental Results on Charge-Changing Collisions of Hydrogen and Helium Atoms and Ions at Kinetic Energies above 0.2 keV," Reviews of Modern Physics, 30, 4, 1137-1168, (October 1958).

33. Wade L. Fite, R. Theodore Brackmann, and William R. Snow, "Charge Exchange in Proton-Hydrogen-Atom Collisions," Physical Review, 112, 4, 1161-1169, (15 November 1958).

34. Michâl Gryzinski, "Classical Theory of Electronic and Ionic Inelastic Collisions," Physical Review, 115, 2, 374-383, (15 July 1959).

35. R. Curran and T. M. Donahue, "Electron Capture and Loss by Hydrogen Atoms in Molecular Hydrogen," Physical Review, 118, 5, 1233-2136, (1 June 1960).

36. Wade L. Fite, R. F. Stebbings, David G. Hummer, and R. T. Brackmann, "Ionization and Charge Transfer in Proton-Hydrogen Atom Collisions," Physical Review, 119, 2, 663-668, (15 July 1960).

37. W. L. Fite, A. C. H. Smith, and R. F. Stebbings, "Charge Transfer in Collisions Involving Symmetric and Asymmetric Resonance," Proceedings of the Royal Society, A268, 527-536, (1962).

38. S. K. Allison, J. Cuevas, and M. Garcia Munoz, "Particle Atomic Stopping Power of Gaseous Hydrogen for Hydrogen Beams. I," Physical Review, 127, 3, 792-798, (1 August 1962).

39. M. N. Huberman, "Partial Ionic Stopping Power and the Energy Expended in Electron Capture and Loss Collisions of Protons in Hydrogen Gas, II," Physical Review, 127, 3, 799-804, (1 August 1962).

40. G. W. McClure, "Charge Exchange and Dissociation of H^+, H_2^+, and H_3^+ Ions Incident on H_2 Gas," Physical Review, 130, 5, 1852-1859, (1 June 1963).

41. H. B. Gilbody and J. V. Ireland, "Ionization of Atomic Hydrogen by Protons in the Energy Range 60 to 400 keV," Proceedings of the Royal Society, A277, 137-141, (1963).

42. Benjamin Roth, "Theory of Electron Capture in H^+-H Collisions," Physical Review, 133, 5A, A1257-A1262, (2 March 1964).

43. Robert C. Stabler, "Classical Impulse Approximation for Inelastic Electron-Atom Collisions," Physical Review, 133, 5A, A1268-A1273, (2 March 1964).

44. G. W. McClure, "Ionization and Dissociation of Fast H_2 Molecules Incident on H_2 Gas," Physical Review, 134, 5A, A1226-A1234, (1 June 1964).

45. J. Cuevas, M. Garcia-Munoz, P. Torres, and S. K. Allison, "Partial Atomic and Ionic Stopping Powers of Gaseous Hydrogen for Helium and Hydrogen Beams," Physical Review, 135, 2A, A335-A345, (20 July 1964).

46. R. A. Langley, D. W. Martin, D. S. Harmer, J. W. Hopper, and E. W. McDaniel, "Cross Sections for Ion and Electron Production in Gases by Fast Helium Ions (0.133-1.0 MeV). I. Experimental," Physical Review, 136, 2A, A379-A385, (19 October 1964).

47. D. W. Martin, R. A. Langley, D. S. Harmer, J. W. Hooper, and E. W. McDaniel, "Cross Sections for Ion and Electron Production by Fast Helium Ions (0.133-1.0 MeV). II. Comparison with Theory," Physical Review, 136, 2A, A385-A392, (19 October 1964).

48. M. R. C. McDowell, ed., Atomic Collision Processes, (North-Holland Publishing Company, Amsterdam), (1964).

49. O. Hollricher, "Umladung und Ionisation beim Durchgang von leichten und schweren Wasserstoffionen durch leichten und schweren Wasserstoff," Zeitschrift fur Physik, 187, 41-51, (1965).

50. Michál Gryzinski, "Two-Particle Collisions. I. General Relations for Collisions in the Laboratory System," Physical Review, 138, 2A, A305-A321, (19 April 1965).

51. Michál Gryzinski, "Classical Theory of Atomic Collisions. I. Theory of Inelastic Collisions," Physical Review, 138, 2A, A336-A358, (19 April 1965).

52. H. B. Gilbody and G. Ryding, "An Experimental Study of Charge Transfer in Proton-Atomic Hydrogen Collisions at Impact Energies above 40 keV," Proceedings of the Royal Society, A291, 438-443, (1966).

53. L. J. Kieffer and G. H. Dunn, "Electron Impact Ionization Cross-Section Data for Atoms, Atomic Ions and Diatomic Molecules. I. Experimental Data," Reviews of Modern Physics, 38, 1-35, (January 1966).

54. A. B. Wittkower, G. Ryding, and H. B. Gilbody, "An Experimental Study of Charge Transfer in Proton-Atomic Hydrogen Collisions Using a Furnace Target Method," Proceedings of the Physics Society, 89, 541-546, (1966).

55. E. Gerjuoy, "Cross Section for Energy Transfer between Two Moving Particles," Physical Review, 148, 1, 54-59, (5 August 1966).

56. Wolfgang Lotz, "Electron-Impact Ionization Cross-Sections and Ionization Rate Coefficients for Atoms and Ions," Astrophysical Journal Supplement Series, 14, 207-238, (May 1967).

57. J. D. Garcia and E. Gerjuoy, "Charge Transfer in the Classical Binary-Encounter Approximation," Physical Review Letters, 18, 22, 944-946, (29 May 1967).

58. L. Vriens, "Binary-Encounter Proton-Atom Collision Theory," Proceedings of the Physics Society, 90, 935-944, (1967).

59. A. B. Wittkower, G. Levy, and H. B. Gilbody, "An Experimental Study of Electron Loss During the Passage of Fast Hydrogen Atoms through Atomic Hydrogen," Proceedings of the Physics Society, 91, 306-309, (1967).

60. V. A. Belyaev, B. G. Brezhnev, and E. M. Erastov, "Resonance Charge Exchange of Protons and Deuterons at Low Energies," Soviet Physics JETP, 25, 5, 777-782, (November 1967).

61. J. D. Garcia, E. Gerjuoy, and Jean E. Welker, "Classical Approximation for Ionization by Proton Impact," Physical Review, 165, 1, 66-71, (5 January 1968).

62. J. D. Garcia, E. Gerjuoy, and Jean E. Welker, "Classical Calculations of Charge-Transfer Cross Sections," Physical Review, 165, 1, 72-80, (5 January 1968).

63. G. W. McClure, "Ionization and Electron Transfer in Collisions of Two H Atoms: 1.25-117 keV," Physical Review, 166, 1, 22-29, (5 February 1968).

64. E. R. Salvatelli, G. Lantschner, and W. Meckbach, "Search for a Possible Isotope Effect in Charge-Changing Collisions Involving Hydrogen and Deuterium," Journal of Physics b (Atomic and Molecular Physics), Series 2, 2, 772-776, (1969).

65. Robert A. Mapleton, Theory of Charge Exchange, (Wiley-Interscience, New York), (1972).

66. H. Tarawa and A. Russek, "Charge Changing Processes in Hydrogen Beams," Reviews of Modern Physics, 45, 2, 178-229, (April 1973).

67. W. Hess, "Echange de Charge avec Exitation de l'Atome d'Hydrogene par Impact des Ions H^+, H_2^+ sur des Gaz Neutres," EUR-CEA-FC-701, (June 1973).

68. R. C. Dehmel, H. K. Chau, and H. H. Fleischmann, "Experimental Stripping Cross Sections for Atoms and Ions in Gases, 1950-1970," Atomic Data, 5, 231-289, (1973).

69. H. H. Fleischmann, C. F. Barnett, and J. A. Ray, "Small-Angle Scattering in Stripping Collisions of Hydrogen Atoms Having Energies of 1-10 keV in Various Gases," ORNL-4954, (April 1974).

70. C. F. Barnett, et al., "Atomic Data for Controlled Fusion Research," ORNL-5206/5207, (February 1977).

71. J. T. Woo, "Neutral-Injection-Induced Transport in Mirror-Confined Plasmas," Nuclear Fusion, 17, 1373-1376, (1977).

72. R. L. Miller and G. H. Miley, "Ionization and Charge Exchange Rate Coefficients for CTR Calculations," University of Illinois Report COO-2218-26, (29 January 1975).

73. F. Evans, "Energy Deposition of a Fast Deuteron in a Hot Deuterium Plasma," The Physics of Fluids, 16, 1011-1020, (July 1973).

74. J. D. Jackson, Classical Electrodynamics, (John Wiley and Sons, Inc., New York), 451-456, (1963).

75. J. P. Holdren, "Analytical Approximation to Collisional Distributions in Mirror Plasmas," Nuclear Fusion, 12, 267-269, (1972).

76. J. G. Cordey, "Absorption of Plasma Waves in Collisional Mirror Plasmas," The Physics of Fluids, 14, 1407-1410, (July 1971).

77. L. G. Kuo-Petravic, M. Petravic, and C. J. H. Watson, "Alpha Particle Heating and the Energy Balance in a Mirror Reactor," B.N.E.S. Nuclear Fusion Reactor Conference, Culham Laboratory, Paper 2,4, 144-172, (September 1969).

78. D. J. Rose and M. Clark, Jr., Plasmas and Controlled Fusion, (the MIT Press, Cambridge, MA), (1961).

79. D. J. Bender and G. A. Carlson, personal communication, LLL, (1975).

80. R. S. Devoto and J. D. Hanson, "SIGV-A Code to Evaluate Plasma Reaction Rates to a Specified Accuracy," UCRL-52559, (22 September 1978).

81. J. H. Halton, "A Retrospective and Prospective Survey of the Monte Carlo Method," SIAM Review, 12, 1-63, (January 1970).

82. N. Metropolis and S. Ulam, "The Monte Carlo Method," Journal of the American Statistical Association, 44, 335-341, (September 1949).

83. A. S. Householder, ed., Monte Carlo Method, National Bureau of Standards Applied Mathematics Series, 12, (11 June 1951).

84. D. J. Hughes, J. E. Sanders, and J. Horowitz, Physics and Mathematics, Progress in Nuclear Energy, Series 1, Volume 2, (Pergamon Press, New York), (1958).

85. E. D. Cashwell and C. J. Everett, A Practical Manual on the Monte Carlo Method for Random Walk Problems, (Pergamon Press, New York), (1959), also LA-2120, (1957).

86. Yu. A. Schreider, The Monte Carlo Method, (Pergamon Press, New York), (1966).

87. M. H. Kalos, F. R. Nakache, and J. Celnick, "Monte Carlo Methods in Reactor Computations," in Computing Methods in Reactor Physics, (Gordon and Breach Science Publishers, New York), (1968).

88. J. Spanier and E. M. Gelbard, Monte Carlo Principles and Neutron Transport Problems, (Addison-Wesley Publishing Company, Reading, MA), (1969).

89. E. Greenspan, "The Calculation of the Transport of Neutral Atoms in Highly Ionized Plasmas Using Neutron Transport Methods," Nuclear Fusion, 14, 771-778 (1974), also MATT-1001, (September 1973).

90. J. H. Marable and E. M. Oblow, "The Application of Neutron Transport Codes to the Transport of Neutral Atoms in Plasmas," Nuclear Science and Engineering, 61, 90-97, (1976), also ORNL/TM-5164, (February 1976).

91. W. Pfeiffer, "Calculation of Neutral Transport in a Plasma Using a Neutron Transport Method," GA-A13995, (October 1976).

92. Z. El Derini and E. M. Gelbard, "Neutral Transport Code in Plasma," ANL/FPP/TM-75, (15 February 1977).

93. K. H. Burell, "NEUCG: A Transport Code for Hydrogen Atoms in Cylindrical Hydrogenic Plasmas," Journal of Computational Physics, 27, 88-102, (1978), also GA-A14113, (October 1976).

94. J. G. Gilligan, et al., "Multigroup Calculations of Low-Energy Neutral Transport in Tokamak Plasmas," Nuclear Fusion, 18, 63-85, (1978).

95. R. L. Miller and G. H. Miley, "Monte Carlo Simulation of Neutral-Beam Injection into Fusion Reactors," Second IEEE International Conference on Plasma Science, Ann Arbor, MI, 75CH0987-8-NPS, 103, (May 1975).

96. R. L. Miller, "Monte Carlo Simulation of Neutral-Beam Injection into Fusion Reactors," University of Illinois Report COO-2218-38, (15 September 1975).

97. R. L. Miller and G. H. Miley, "Charge-Exchange First Wall Loading in Beam-Driven Mirror Devices," Sixth Symposium on Engineering Problems of Fusion Research, San Diego, CA, (November 1975), 75CH1097-5-NPS, 994-1000, (1976).

98. R. L. Miller and G. H. Miley, "Monte Carlo Studies of Mirror Fusion Reactor Neutral Beam Injection," Second ANS Topical Meeting on the Technology of Controlled Nuclear Fusion, Richland, WA, CONF-760935-P2, 515-527 (September 1975).

99. S. Inoue, et al., "Monte Carlo Analysis of the Neutral Particle Transport in Torus Plasma," JAERI-M-6777, (November 1976).

100. B. Jensen, Random Number Generators, (Victor Pettersons Bokindustri Aktiebolag, Stockholm), (1966).

101. R. R. Coveyou and R. D. MacPherson, "Fourier Analysis of Uniform Random Number Generators," Journal of the Association for Computing Machinery, 14, 100-119 (January 1967).

102. A. van Gelder, "Some New Results in Pseudo-Random Number Generation," Journal of the Association for Computing Machinery, 14, 785-792, (October 1967).

103. G. Marsaglia, "Random Numbers Fall Mainly in the Planes," Proceedings of the National Academy of Sciences, 61, 25-28, (1968).

104. C. S. Smith, "Multiplicative Pseudo-Random Number Generators with Prime Modulus, "Journal of the Association for Computing Machinery, 18, 586-593, (October 1971).

105. C. J. Everett, "Number Theory of the Congruential Random Number Generators," LA-6667-MS, (January 1977).

106. L. L. Carter, E. D. Cashwell, and W. M. Taylor, "Monte Carlo Sampling with Continuously Varying Cross Sections Along Flight Paths," Nuclear Science and Engineering, 48, 403-411, (1972).

107. H. Kahn, "Use of Different Monte Carlo Sampling Techniques," in Symposium on Monte Carlo Methods, (J. Wiley & Sons, New York), (1954).

108. H. Kahn and A. W. Marshall, "Methods of Reducing Sample Size in Monte Carlo Computations," Journal of the American Operations Research Society, 1, 262-283, (November 1953).

109. J. M. Hammersley and K. W. Morton, "A New Monte Carlo Technique: Antithetic Variates," Proceedings of the Cambridge Philosophical Society, 52, 449-475, (1956).

110. J. M. Hammersley and J. G. Mauldon, "General Principles of Antithetic Variates," Proceedings of the Cambridge Philosophical Society, 52, 476-481, (1956).

111. S. Ulam, "On the Monte Carlo Method," Proceedings of the Second Symposium on Large-Scale Digital Calculating Machinery, 207-212, (1951).

112. M. Abramowitz and I. A. Stegun, Handbook of Mathematical Functions, National Bureau of Standards Applied Mathematics Series: 55, (1964).

113. D. J. Bender, personal communication, LLL, (1975).

114. D. J. Bender and G. A. Carlson, "System Model for Analysis of the Mirror Fusion--Fission Reactor," UCRL-52293, (12 October 1977).

115. L. S. Hall, "Magnetostatic Equilibria of Finite-Pressure Minimum-B Plasma Configurations," The Physics of Fluids, 15, 882-890 (1972).

116. D. J. Bender and G. A. Carlson, personal communications, LLL, (1975-6).

117. R. S. Devoto, "Update of Plasma Parameters for a Mirror FERF," UCRL-52203, (6 January 1977).

118. G. H. Miley, "Potential Mirror Concepts for Radiation Testing of Fusion Reactor Materials," Nuclear Instruments and Methods, 145, 169-177 (1977).

119. M. A. Hoffman and R. W. Werner, "Heat Flux Limitations on First-Wall Shields for Early Fusion Machines, Proceedings of the First Topical Meeting on the Technology of Controlled Nuclear Fusion, CONF-740402-P1, 619-633, (16-18 April 1974), also UCRL-75622, (April 1974).

120. R. W. Moir, "Surface Bombardment Rates for Mirror Fusion Reactor Designs," UCRL-77799, (3 February 1976).

121. R. Behrisch, "First-Wall Erosion in Fusion Reactors," Nuclear Fusion, 12, 695-713, (1972).

122. H. Vernickel, "Wall Erosion in a Fusion Reactor Due to Sputtering," Nuclear Fusion, 12, 386, (1972).

123. N. Laegreid and S. D. Dahlgren, "Controlled Thermonuclear Reactor First Wall Sputtering and Wall Life Estimates," Journal of Applied Physics, 44, 2093-2096, (May 1973).

124. H. K. Perkins, "Ion and Fast Neutral Bombardment of Surfaces in Controlled Fusion Devices," MATT-1005, (October 1973).

125. I. O. Bohachevsky and J. F. Hafer, "Sputtering Erosion of Fusion Reactor Cavity Walls," LA-6633-MS, (December 1976).

126. B. Badger, et al., "UWMAK-I: A Wisconsin Toroidal Fusion Reactor Design," UWFDM-68, (1973).

127. R. A. Krakowski, et al., "An Engineering Design Study of a Reference Theta-Pinch Reactor (RTPR)," LA-5336 and ANL-8019, (1974).

128. R. A. Krakowski, R. L. Miller and R. L. Hagenson, "Operating Point Considerations for the Reference Theta-Pinch Reactor (RTPR)," Proceedings of the Second Topical Meeting on the Technology of Controlled Nuclear Fusion, CONF-760935-P1, 359-370, (21-23 September 1976).

129. G. E. Gryczkowski, "Neutral-Gas-Blanket Theory as Applied to the Reference Theta-Pinch Reactor," Ph.D. Thesis, University of Michigan, (1978).

130. A. J. Summers, N. J. Freeman, and N. R. Daly, "Sputtering of Niobium by Niobium, Hydrogen, Deuterium and Helium Ions in the 10-80-keV Energy Range," Journal of Applied Physics, 42, 4774-4778, (November 1971).

131. D. T. Goldman and A. Simon, "Theory of Sputtering by High-Speed Ions," Physical Review, 111, 383-386, (15 July 1958).

132. W. Brandt and R. Laubert, "Unified Sputtering Theory," Nuclear Instruments and Methods, 47, 201-209, (1967).

APPENDIX: COMPUTER CODE USER'S GUIDE

A. Running NUBIN without changes.

The MCSAVG and NUBIN computer code package developed for this study is written in the FORTRAN language and currently implemented on the Control Data Corporation (CDC) 7600 computer of the Magnetic Fusion Energy Computer Center (MFECC) of the U. S. Department of Energy, Office of Fusion Energy. This Guide will assume a certain level of familiarity with the utility routines of that system, online documentation of which is available through the routine DOCUMENT.

The files of the code package are available through FILEM using the command:

FILEM .READ 504 .NUBIN <*list*> / *t v*

where <*list*> is a string of file names chosen from Table A1, t is the user-allocated time limit and v is the priority value.

Consider first the execution of the already compiled version of NUBIN for the FERF (i.e., MFF). With MFF and the data file FA5 (or FB5 or FC5) available, the execution line is

MFF / *t v*

with t = 10 being sufficient for 10^4 test particles. Upon normal completion, the file FA6 contains the output summary with files FA1, FA2, FA7, FA8, FA9, FA10 containing additional tables of graphed values. In particular FA10 is used to reinitialize MFF in order to continue a previous run (see use of IUI and JCYCLE in Table A4). Plot output is contained in the file DXPLOTSMFF which can be processed by the utility routines NETPLOT and TEKPLOT for paper, film or CRT terminal output. Tables A2 and A3 list sample data files FA5 and MA5 for the

FERF and MFTF primary beam cases, respectively. Changes to these files can be made using the TRIX AC editor. Table A4 discusses the variables required in these input files. To run cases for values of $\tilde{E}_p$ = EAVGPL much different ($\pm$10 keV) from the FERF value of 70 keV or the MFTF value of 50 keV requires a recompilation of MCS with a new version of BLKMFF or BLKMMX containing new <σv> tables as described in Sect. B below.

The MCSAVG and NUBIN codes use certain library routines of the TV80LIB, ORDERLIB, STACKLIB and IMSL system libraries; access to which is obtained through AVGLOD and MCSLOD when the codes are complied and loaded. This aspect is transparent to the user at this level.

B. Making changes in NUBIN.

New interaction <σv> tables are generated by running the MCSAVG code. A sample input file AVG5 is listed in Table A5 with explanation in Table A6. With the files AVGLOD, MCSAVG, RMLIBB and AVG5 available, the command for compilation and execution of MCSAVG is

CHATR (AVGLOD%) MCSAVG MAV$ LAV *box* L L / 20 *v*.

Upon normal completion the file AVG6 contains an output summary and DXPLOTMAVG contains plots of <σv> vs. E_I for various values of θ_I. Using the TRIX AC editor, appropriate lines of AVG8 must be substituted into BLKM_ _ to effect the required <σv> interface to the NUBIN code. The suffix _ _ indicates FF or MX for the FERF or MFTF, respectively.

The new version of BLKM_ _ is compiled with the command

CHATR (AVGLOD%) BLK_ _ C BL$ LDAT *box* L L / 1 *v*.

With the file MCSLOD available, the relocatable binary file BL is then used to create a new version of MCS using the command

CHATR (MCSLOD%) MCS M_ _ BCS$ L_ _$ *box* L L / 5 *v*

which results in an executable file M_ _ for which the discussion in Sect. A applies. AVGLOD% and MCSLOD% make the appropriate system library routines available.

TABLE A1

MCSAVG/NUBIN Code Package Files

File Name	Application[1]	Type[2]	Remarks
AVGLOD	M	C	
MCSAVG	M	F	MCSAVG source
AVG5	M	D	MCSAVG data
RMLIBB	M,N	B	Contains SUBROUTINE RMAXIS
BLKFF	N	F	FERF <σv> data (70 keV)
BL	N	B	Binary of BLKFF
BLKMX	N	F	MFTF <σv> data (50 keV)
MCSLOD	N	C	
MCS	N	F	NUBIN source
RMPL3DB	N	B	Contains SUBROUTINE PLOT3D
MFF	N	B	Binary of MCS (FERF)
MMX	N	B	Binary of MCS (MFTF)
FA5	N	D	FERF data (E_0)
FB5	N	D	FERF data ($E_0/2$)
FC5	N	D	FERF data ($E_0/3$)
FD5	N	D	FERF data (<E>)
MA5	N	D	MFTF data (E_0)
MB5	N	D	MFTF data ($E_0/2$)
MC5	N	D	MFTF data ($E_0/3$)
MD5	N	D	MFTF data (<E>)
MCSFD	N	F	FD10 from FA10, FB10, and FC10

[1] M denotes the MCSAVG code and N denotes the NUBIN code

[2] B = relocatable binary, C = command file, D = data file, F = FORTRAN source file

TABLE A2

FERF Sample Input Data File FA5 for NUBIN Code

```
        10          10          10
     0.000       0.000       0.000
    25.000      80.000     210.000     210.000
   -40.000       0.300       3.000
  0.3000000E+15
     0.999       3.000
70000.000   7000.000
  0.0000000E+00    0.0000000E+00
22200.000       0.650
     2.000
     0.575       0.292       0.218
   -45.000       0.000     -30.000
  0.9827937E+00    0.0000000E+00
     0.218       0.200           2
65000.000
           1           1
           6
           3
  0.9900000E-15
           2       25000
           5           2
          10
     4.000
     4.100
     4.200
     4.300
     4.400
     4.500
     5.000
     8.000
    10.000
 1010.000
     0.001
     0.005
  0.8000000E+00    0.8000000E+00    0.4000000E+00    0.1800000E+18         9
           1           1          10           0
45.         135.
           7654321             1
```

TABLE A3

MFTF Sample Input File MA5 for NUBIN Code

```
        10          10          10
     0.000       0.000       0.000
    60.000     200.000     170.000     170.000
   -60.000       0.680      10.000
  0.9500000E+14
     0.999       2.100
 50000.000    5000.000
  0.0000000E+00     0.0000000E+00
 20000.000       0.500
     2.000
     0.606       0.296       0.222
  -300.000    -300.000       0.000
  0.1570000E+01     0.7850000E+00
     0.115       0.100           2
 75000.000
           1           1
           6
           3
  0.5000000E-16
           2       25000
           5           2
          10
     4.000
     4.100
     4.200
     4.300
     4.400
     4.500
     5.000
     8.000
    10.000
  1010.000
     0.001
     0.005
  0.8000000E+00     0.8000000E+00     0.5000000E+00     0.1800000E+18         9
           1           1          10           0
 45.         135.
    23456787654321              1
```

TABLE A4

Explanation of NUBIN Code Input File

Line Number	Format	Variable Name(s)	Meaning	Remarks
1	3I10	IUI	Data input file specification	To begin a run set IUI = 5. To continue a prior run, set IUI equal to the IUO1 of the prior run in order to properly initialize the counters. Also update JCYCLE below.
		IUO1	Date output file specification	This index identifies the output file into which much of the data is dumped and updated after each simulation cycle. Do not use 1,2,4,8,9.
		IUO2	Data output file specification	Under certain error conditions, the latest data will be dumped into this file.
2	3F10.3	XHP YKP ZLP	Cartesian coordinates of the plasma midpoint. (units: cm)	Require: XHP, YKP, ZLP = 0.0

Line Number	Format	Variable Name(s)	Meaning	Remarks
3	4F10.3	RPL1	Plasma mid-plane radius	RWL1 > RPL1
		RWL1	"First wall" radius. Plasma half-length.	Distance between midplane and mirror point.
		PLNG		
		WLNG	Half-length of "first wall".	
4	3F10.3	AAA	These parameters determine the plasma geometry following the Bender model. (units: cm)	
		PHIM		PHIM < 00 for cylindrical option
		HTFAN	(units: radians) (units: cm)	
5	E16.7	XNPLCR	Central plasma density (units: ions/cm^3)	
6	2F10.3	XXI	Radial density profile parameters	$\frac{n(r)}{n_o} = [1 - X\ (\frac{r}{R})^j]$
		XXJ		X = XXI
				j = XXJ
				$0.0 \leq X \leq 0.999$

Line Number	Format	Variable Name(s)	Meaning	Remarks
7	2F10.3	EAVGPL EAVGEL	Characteristic plasma ion and electron energies (units: eV)	EAVGPL should correspond to the value used by MCSAVG to calculate the <σv> tables in BLK _ _.
8	2E16.7	THEB PHIB	Polar orientations of the magnetic axis $\overline{B}(\theta,\phi)$ (units: radians)	Require: THEB = PHIB = 0.0
9	2F10.3	BFIELD BETA	Central vacuum magnetic field strength and β (units: Gauss)	
10	F10.3	RVACC	Vacuum mirror atio	
11	3F10.3	G0 G1 G2	Plasma volume integration factors, consistent with Table 3 of Moir & Taylor, "Magnets for Open-Ended Fusion Reactors," with G0 = C°, etc.	Must be consistent with the mirror ratio.

Line Number	Format	Variable Name(s)	Meaning	Remarks
12	3F10.3	XHB YKB ZLB	Cartesian coordinates of the neutral beam point source (units: cm)	This point must lie outside the plasma.
13	2E16.7	THEI PHII	Polar orientations of the injection orientation $\overline{I}(\theta,\phi)$ (units: radians)	One should verify that the beam intersects the plasma.
14	2F10.3,	ALPHA BETAB IOPTBM	Angular half-width of the conical beam = α. Angle at which the beam intensity falls by 1/e if IOPTBM = 3 is specified = β_B.	IOPTBM = 1 for pencil beam, $\alpha = 0$ IOPTBM = 2 for uniform beam, $\alpha > 0$ IOPTBM = 3 for Gaussian beam, $0 < \beta_B < \alpha$
15	F10.3	EINJCT	Neutral beam injection energy (units: eV)	
16	2I10	NINJ NPLA	Number of injection species and number of plasma ion species	Require: NINJ = 1 NPLA = 1 If a multispecies version is ever developed, this will have some significance.

Line Number	Format	Variable Name(s)	Meaning	Remarks
16.1	I10	ISPECI(1)	Identification index for injection species	5 indicates H^1 6 indicates H^2 7 indicates H^3
.	.	.		
.	.	.		
.	.	.		
16.NINJ		ISPECI(NINJ)		Must have proper <σv>'s.
16.NINJ+1	I10	ISPECP(1)	Identification index for plasma ion species.	2 indicates H^{1+} 3 indicates H^{2+} 4 indicates H^{3+}
.		.		
.		.		
.		.		
16.NINJ + NPLA		ISPECP(NPLA)		Must have proper <σv>'s.
17	E16.7	SGMAVK	Fusion reactivity <σv> (units: cm^3/sec)	Must be consistent with EAVGPL.
18	2I10	NCYCLE NPARTC	Number of cycles in this run. Number of test particles/cycle.	Recommend: NCYCLE = 10 NPARTC = 10^4
19	2I10	MMMM IOPTGR	First wall surface grid resolution parameter. Grid type switch IOPTGR = 1 for spherical surface IOPTGR = 2 for cylindrical surface	1 < MMMM < 6 Recommend: MMMM = 5 (gives 64x128 grid)

Line Number	Format	Variable Name(s)	Meaning	Remarks
20	I10	NREGN	Number of coaxial plasma subregions. The thickness of these subregion should exceed a Larmor radius.	1 < NREGN < 20
20.1 . . . 20.NREGN	F10.3	CFACTR(1) . . . CFACTR(NREGN)	Monte Carlo sampling parameters	These should be inversely proportional to the plasma density profile on the range 4. < C_{FACTOR} < 1010 for best results.
21	F10.3	ERRTOL	Tolerance for simulation convergence	Recommend: 0.01 > ERRTOL > 0.001
22	F10.3	CRUSWT	"Russian Roulette" weight cutoff value	Recommend: 0.05 > CRUSWT > 0.005
23	4E16.7, I8	REJCF1 REJCF2 REJCF3 SPDCF2 ICOUNT	Various Monte Carlo simulation parameters	Recommend: Leave these as indicated in Tables A2-A3.

Line Number	Format	Variable Name(s)	Meaning	Remarks
24	4I10	IHISTO IPLOTO IPUNCH IWALLO	Histogram output switch. Plot output switch. Another output data set. Individual terminal output for each test particle.	Yes / No 1 / 0 1 / 0 7 / 0 8 / 0 for small runs, Require: IHISTO = 0 IPLOTO = 0 for large runs, Recommend: IWALLO = 0
25	2F10.3	VIEW1 VIEW2	Plot output viewing orientations. PLOT3D (units: degrees)	Recommend: VIEW1 = 45.0 VIEW2 = 135.0
26	I10	JCYCLE	Index of first cycle in this run	IF JCYCLE > 1, then IUI ≠ 5.
27	I12	JINITO	Initiator for the pseuds-random number generator, LRNFL	Should be odd.

TABLE A5

Sample Input File AVG5 for MCSAVG Code

```
     3.000          0          0          1          3
         6          3
 0.392699  0.000000          5
70000.000  7000.000
        48   0.2500000E+08
070070070070
```

TABLE A6

Explanation of MCSAVG Code Input File AVG5

Line Number	Format	Variable Name(s)	Meaning	Remarks
1	F10.3, 4I10	RMREFF	Effective mirror ratio	Should equal either 3.0 or 10.0 Is arbitrary if IMAXWL=ISOTRO=1
		IMAXWL	Energy distribution switch	=1 for Maxwellian =0 for Mirror-confined Electrons are assumed to be Maxwellian
		ISOTRO	Angular distribution switch	=1 for isotropic =0 for mirror normal mode Electrons are assumed to be isotropic
		INDSGM	Lower limit of interaction loop	DO 90 INDSGM=INDSGM,MINDSGM
		MNDSGM	Upper limit of interaction loop	1: charge exchange, cx 2: ion ionization, ii 3: Rutherford scattering RS 4: Electron ionication, ei
2	2I10	NMI	Test particle index	1: e^- 5: H^o 2: H^+ 6: D^o 3: D^+ 7: T^o 4: T^+ 8: He^{++} (do not use)
			Field particle index	

Line Number	Format	Variable Name(s)	Meaning	Remarks
3	F10.6,I10	ANGINC	Angular increment of test particle injection angle	(units: radians)
		PHII	Azimuthal injection angle	Recommend: 0.0
		NANG	Number of test particle angle increments	Maximum: 5 (unless dimension statements altered) $0 \leq NANG*ANGINC \leq \pi/2$
4	2F10.3	EAVGPL	Plasma ion characteristics energy	(units : eV)
		EAVGEL	Plasma election characteristic energy	(units : eV)
5	I10,E16.7	NPTS	Number of test particle speed increments	Maximum : 48 (unless dimension statements altered)
		SPDINC	Test particle speed increment	(units : cm/s)
6	4A3	ITITL(INDSGM), INDSGM=1,4	Array name information	Used by MCSAVG only to identify $\langle\sigma v\rangle$ tables, e.g. 020 indicates EAVGPL=20 keV

The author is available at the following address and telephone number to provide additional information and answer questions regarding the MCSAVG/NUBIN code package:

Ronald L. Miller
MS-641
Los Alamos Scientific Laboratory
P. O. Box 1663
Los Alamos, NM 87544 USA

(505) 667-4950 Commercial Telephone

843-4950 FTS

A FORTRAN listing of the MCSAVG and NUBIN codes is available under a separate report number from the

Fusion Studies Laboratory
Nuclear Engineering Program
University of Illinois
Urbana, IL 61801 USA

VITA

Ronald Lee Miller was [redacted]

He was raised in East Moline, Illinois and attended elementary and secondary schools there. In September, 1967 he entered the University of Illinois at Urbana-Champaign. He graduated in June, 1971 with the B.S. degree in Physics. Entering the Nuclear Engineering Program of the University of Illinois at Urbana-Champaign in February, 1972; he served as a teaching assistant and research assistant in the Fusion Studies Laboratory. In the latter capacity, he published several reports and articles relating to plasma engineering questions. He received the M.S. degree in Nuclear Engineering in February, 1973. He was employed by the Engineering Division of the Argonne National Laboratory during the summer of 1974, and served as a consultant to the Lawrence Livermore Laboratory in December, 1975. He is currently a member of the staff of the Controlled Thermonuclear Research Division of the Los Alamos Scientific Laboratory of the University of California. He is a member of Sigma Xi.